MASTER THESIS

OSCILLATORY FLOW IN JET PUMPS: SETUP DESIGN AND EXPERIMENTS

Mahening Citra Vidya

FACULTY OF ENGINEERING TECHNOLOGY
LABORATORY OF THERMAL ENGINEERING

EXAMINATION COMMITTEE

Prof.dr.ir. T.H. van der Meer (chairman)
Ir. J.P. Oosterhuis (internal member)
Dipl. Ing. S. Bühler (internal member)
prof.dr.ir. A. Hirschberg (external member)

UNIVERSITY OF TWENTE.

MASTER THESIS

OSCILLATORY FLOW IN JET PUMPS: SETUP DESIGN AND EXPERIMENTS

AUTHOR

Mahening Citra Vidya

EXAMINATION COMMITTEE

Prof. dr. ir. T.H. van der Meer	(*chairman*)
Ir. J.P. Oosterhuis	(*internal member*)
Dipl. Ing. S. Bühler	(*internal member*)
Prof. dr. ir. A. Hirschberg	(*external member*)

UNIVERSITY OF TWENTE

Faculty of Engineering Technology

Department of Mechanical Engineering

Drienerlolaan 5

7522 NB Enschede

Enschede

August 20, 2014

SUMMARY

Thermoacoustic devices have been developed over the past decades for various applications, such as power generation, cryogenic cooling, refrigeration and air conditioning. Despite the advantages of the thermoacoustic devices, there are still some challenges left that need to be solved, such as an acoustic streaming namely Gedeon streaming. To suppress the Gedeon streaming, a nonuniform cross-sectional device known as a jet pump is studied.

To study the effect of a jet pump, a thermoacoustic experimental setup is used. This setup has been used previously for experiments with a standing wave. In order to perform experiments with a traveling wave, a modification of the previous setup is required. Hence, a traveling wave termination using a quarter-wavelength resonator was designed and tested. Results show that the termination works best at 113 Hz with absorption coefficient of 99.9%.

The previous experimental setup and the modified setup are used to test four jet pump samples. The jet pump samples have been designed with various geometries to investigate the applicability of both Backhaus-Swift quasi-steady model and the steady flow minor loss coefficient in case of an oscillatory flow. The effect of the wave phasing and the geometrical parameters, such as taper angle and number of holes, in relation to pressure drop and acoustic power dissipation are investigated. It was found that different behavior occurs for high taper angle jet pumps (15° and 18°), therefore the quasi-steady model of Backhaus-Swift does not hold. The higher taper angle also leads to lower pressure drop and higher energy dissipation. Thus, the steady flow minor loss coefficient also cannot be applied in the case of oscillatory flow.

To get a better understanding on the behavior of the oscillatory flow, a flow visualization experiment is conducted. A new test section for flow visualization, which uses a smoke wire method, has been developed. Using this method, the gas oscillation as well as three flow patterns can be observed. The first flow pattern that was observed is a mean flow that occurs at the outer boundary of the jet pump hole, in which the smoke is sucked into the jet pump. The second flow pattern is an outburst flow which is visible only at low velocity amplitude. The last flow pattern is a vortex ring that propagates away from the jet pump opening.

It can be concluded that the smoke wire method can be applied to visualize the flow pattern of a jet pump in an oscillatory flow, which represents its condition in a thermoacoustic device. The observed flow patterns can be a reference for future research using other jet pump samples.

PREFACE

Firstly, I would like to express my gratitude to my daily supervisor, Joris Oosterhuis, to whom I am so much indebted. This thesis would not be possible without his guidance. His positive support, discussion and corrections are greatly appreciated. I would like to thank Theo van der Meer, who allowed me to work on this project and always encouraged me to discuss during our weekly meeting. His guidance since the first time I arrived in this university until my graduation day will not be forgotten. I am also grateful to Simon Bühler, for carefully reading the thesis draft and providing important comments as well as discussions.

This thesis consists of design process and experimental work in the Thermal Engineering Laboratory. During these nine months, I gain a lot of knowledge and insight in the field of thermoacoustic. The design process required me to learn Matlab and deal with the scripts, which provide me with valuable skill. I also have more experience in working with the experimental setup, for which I am very grateful for the opportunity. Generous support from the Indonesian Ministry of Education Scholarship that made me possible to reach this opportunity is gratefully acknowledged.

The experimental works would not be possible to perform without the help of Henk-Jan Moed and Robert, who assisted me with the experimental setup, constructed the flow visualization test section and helped me during my time in the laboratory. Special thanks to my partners in the lab, Frederieke and Koen, who helped me to obtain the experimental data. Furthermore, I would like to thank the guys in N248: Rob, Sjoerd, Niek and Gerrald, who were there during the whole thesis period and of course, thank you for teaching me klaverjas and for giving me a very good time in our room. I also thank Riza who supplied me with enormous amount of food, my colleagues in Thermal Engineering, my housemates and all Indonesian people in Enschede.

Finally, I acknowledge my thanks to my parents and my wonderful brother for their endless love and support.

Mahening Citra Vidya

Enschede, August 2014

CONTENTS

LIST OF FIGURES

LIST OF TABLES

NOMENCLATURE

NOMENCLATURE		
	$\dot{M}_2$	Time-averaged streaming mass flux
	$\widetilde{U_1}$	First-order complex volumetric velocity
	$U_{2,0}$	Second-order time-independent volumetric velocity
	ρ	Density
	ρ_1	Density at $T_1 = 0\ K$
	$\dot{Q}_{leak}$	Heat loss due to streaming
	T	Temperature
	Δp	Time-averaged pressure drop
	p	Pressure
	K	Minor loss coefficient
	u	Axial velocity
	v	Radial velocity
	A	Cross sectional area
	A_{in}	Cross sectional area before the expansion
	A_{out}	Cross sectional area after the expansion
	R	Radius
	$2R_{s,min}$	Diameter of jet pump waist
	U_1	Volume flow rate
	R_0	Gas constant
	ϕ	Dissipation function, representing heat transfer due to internal friction
	s	Shear wave number
	ρ_0	Density of air at standard condition
	ω	Angular frequency
	μ	Dynamic viscosity
	k_r	The reduced frequency
	c_0	Speed of sound at standard condition
	σ	The square root of the Prandtl number
	C_p	Specific heat capacity at constant pressure
	λ	Thermal conductivity Wavelength

γ	Ratio of the specific heats
C_v	Specific heat capacity at constant volume
f	Frequency
t	Time
x	x-coordinates
r	Radial coordinates
i	Imaginary unit
ξ	Axial dimensionless coordinate
η	Radial dimensionless coordinate
Γ	Propagation constant
n	Polytrophic coefficient Number of frame taken (flow visualization)
J	Bessel function
$\hat{p}$	Complex pressure amplitudes
G	Parameter which depends on the cross-sectional shape of the resonator
L	Length
V	Volume
Q	Mass flow
n_V	Polytrophic coefficient for a volume
m_V	Time-dependent mass for a volume
R	Reflection coefficient
α	Absorption coefficient Taper angle
d	End correction
N	Number of samples recorded for pressure measurement
$\emptyset$	Phase difference between two pressure sensor
θ	Phase difference between pressure and velocity
$\dot{E}$	Acoustic power dissipation
δ_v	Viscous penetration depth
K_E	Summation of minor loss coefficient for forward flow and backward flow
fps	Frame per second
x_v	Distance covered by the propagating vortex
u_v	Vortex propagation speed

INDICES	C	Cold
	H	Hot
	ml	Minor loss
	m	Mean
	exp	Expansion
	$cont$	Contraction
	s	Narrow-end
	b	Wide-end
	in	Flow in-to the narrow-end
	out	Flow out-of the narrow-end
	$curv$	curvature
	jp	Jet pump
	max	Maximum
	min	Minimum
	A	Backward propagating wave
	B	Forward propagating wave
	g	Geometrical
	e	Effective
	tot	Total
	avg	Average
	c	Vena contracta

ABBREVIATION	TAP	Thermo Acoustic Power
	PMMA	Polymethylmethacrylate

CHAPTER 1
INTRODUCTION

1.1. Background

Thermoacoustics is a phenomenon associated with thermodynamics and acoustics. Thermoacoustic devices have been developed over the past decades for various applications, such as power generation, thermoacoustic cryogenic cooling, refrigeration and air conditioning. In this section, some examples of thermoacoustic devices that have been used for commercial advantages will be explained.

Thermoacoustics use acoustic wave motion instead of a piston to perform a thermodynamic cycle. Due to the absence of moving mechanical parts in the thermoacoustic device, the manufacturing of the components does not need to have a high tolerance or specific machining requirement. The absence of moving mechanical parts also eliminates mechanical friction and wear, thus increasing the operational life and minimizing the maintenance and material cost. These advantages make thermoacoustics devices interesting for application [1,2,3].

One of the advantages of thermoacoustics is its ability to use a low grade heat source to produce acoustic work. The Dutch pilot project of Thermo Acoustic Power (TAP) is built in the north of the Netherlands and has been successfully generating electricity for industrial scale from the waste heat of a flue gas. This project concludes that the power level of the TAP should be scaled up to at least 50-100 kW electricity output power to become economic viable [4]. The pilot project has made clear that the conversion from waste heat into acoustic power is efficient and scalable. Another example of power generation is the down-well power generation of the natural gas industry [1]. By adding a side branch to the natural gas pipe and adjusting its length to the gas flow speed, it is possible to match the frequency of natural gas inside the pipe with the side branch pipe, hence creating a standing wave sound field in the side branch pipe. Thus, a temperature oscillation will result and electricity for sensor application can be provided.

Another application of thermoacoustics is the cooling effect which can be used for food refrigeration, air conditioning, or cryocooling. A thermoacoustic refrigeration system has been developed in Los Alamos National Laboratory, where the system can liquefy natural gases, hence the term thermoacoustic cryocooling. A group of researchers from the Pennsylvania State University also developed several projects based on thermoacoustic refrigeration, such as cooling device for electronics (SETAC project, [1]), spacecraft application (STAR project, [1]), and thermoacoustic a chiller (TRITON project, [1,5]).

Even though thermoacoustic devices are profitable, there are still some challenges that need to be solved before it can be used competitively on a large scale [1]. In order to produce work on a large scale, a compact thermoacoustic device with high pressure amplitude is needed. Some phenomena that happen in oscillatory flow at high pressure amplitude may degrade the thermoacoustic device performance. Complicated flow patterns such as vortex shedding, turbulence, shock waves and streaming are some examples of this phenomena [1,3]. Two types of acoustic streaming can degrade the efficiency of a thermoacoustic device, namely Gedeon streaming and Rayleigh streaming [2]. To suppress the Gedeon streaming, a nonuniform cross-

sectional device which is known as a jet pump is studied. Various jet pump samples are tested in the experimental setup for this thesis.

The experimental setup used to perform experiments in the scope of this thesis was originally established at the Technical University of Eindhoven. This setup is now being used at the University of Twente. The experimental setup consists of three main parts: the loudspeaker, the main tube and the cone which connects the loudspeaker and the main tube.

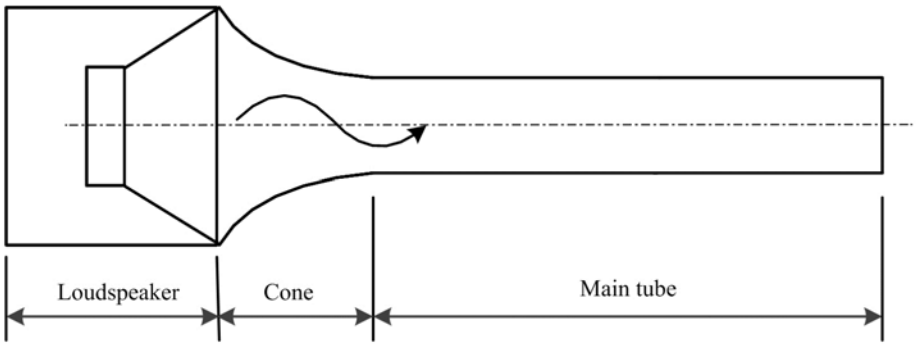

Figure 1.1 The standing wave experimental setup

This setup has been used previously for experiments with a standing wave inside the main tube. In order to perform experiments with a traveling wave, a modification of this thermoacoustic setup is needed. By adding an acoustic resonator at the end of the main tube, the sound wave can be absorbed, hence creating a forward traveling wave inside the main tube.

The focus of this thesis is mainly on the jet pump experiments using both a standing wave and a traveling wave in the setup. Chapter 2 explains the current setup and the modification that has been made. A detailed explanation about the design and testing of the traveling wave termination is covered in this chapter. Another test section has been made for flow visualization using a smoke wire. This test section is also explained in Chapter 2. Chapter 3 presents the jet pump samples and the results of the experiment. Finally, Chapter 4 delivers conclusion and suggestions for future work.

1.2. Jet pump principle

The Gedeon streaming is a mean mass flux that occurs in a looped thermoacoustic engine. This mass flux reduces the thermal efficiency of the engine because it enhanced unwanted convective heat transfer [6]. One way to keep the thermal efficiency as high as possible is by using a jet pump to balance the streaming mass flux. The utilization of a jet pump to suppress the Gedeon streaming mass flux was investigated by Backhaus and Swift [2]. Figure 1.2 shows their apparatus which consists of a looped tube, a resonator and a variable acoustic load. There they showed the utilization of a jet pump in the looped section right before the main cold heat exchanger.

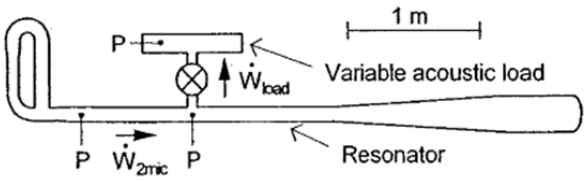

(a) The setup used by Backhaus and Swift for their experiment to study the streaming effects.

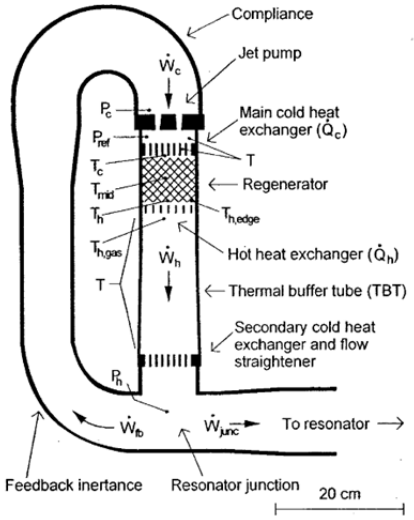

(b) Scale drawing of the looped section.

Figure 1.2 Schematic drawing of a travelling-wave based thermoacoustic engine [2].

From their experiment, it was concluded that Gedeon streaming is a major problem to overcome [2]. A mass flux can exist in the looped section as a result of the pressure difference caused by the regenerator. This mass flux leads to heat losses in the system and therefore it should be eliminated. The mass flux flows in a clockwise direction in the picture and its time-averaged formulation is expressed as:

$$\dot{M}_2 = \frac{\boldsymbol{Re}[\rho_1 \widetilde{U_1}]}{2} + \rho_m U_{2,0} \tag{1.1}$$

where ρ_1 is the density at $T_1 = 0\ K$, $\widetilde{U_1}$ is the first-order complex volumetric velocity, ρ_m is the mean density of ρ_1 and ρ_c, and $U_{2,0}$ is the second-order time-independent volumetric velocity.

The first term in the right hand side of the equation is always nonzero because it is proportional to the engine output power [6]. Thus, a mass flux will flow from the hot heat exchanger to the secondary cold heat exchanger. This mass flux carries away a heat loss of $\dot{Q}_{leak} = \dot{M}_2 C_p (T_H - T_C)$, thus lowering the engine efficiency. Since this mass flux is unwanted in the system, one way to suppress this streaming mass flux is by reducing the value of $\rho_1 \widetilde{U_1}$. However, as this value is proportional to the output power of the engine, reducing $\rho_1 \widetilde{U_1}$ would lead to a reduced engine performance. In order to have the same engine performance with no streaming, another solution is by imposing the second term in the right hand side such that it cancels the first term. Thus, a volumetric velocity of $U_{2,0}$ should flow to balance the streaming mass flux and this can be achieved using a jet pump.

A jet pump is an asymmetric constrictions in a tube formed from two transitions in cross section connected by a conical taper [7]. This transition in cross section could lead to a pressure drop due to minor losses. Minor losses are associated to pressure drop that takes place in junction, bends, valves, or when a flow passes through a sharp edge. In the case of a jet pump, due to the abrupt change of the cross-sectional area in the openings, a minor loss exist which results in a pressure difference across the jet pump.

Consider a jet pump with a geometry shown in Figure 1.3. For a jet pump in an oscillatory flow, a quasi-steady approach by Iguchi [8] can be used to calculate the analytical pressure drop.

This quasi-steady approach is based on the idea that for large amplitudes, the flow has no memory of its past [7]. Therefore, the case of an oscillatory flow can be described using the steady flow approach of a flow going to the right hand side of the jet pump and a flow going to the left hand side of the jet pump in Figure 1.3.

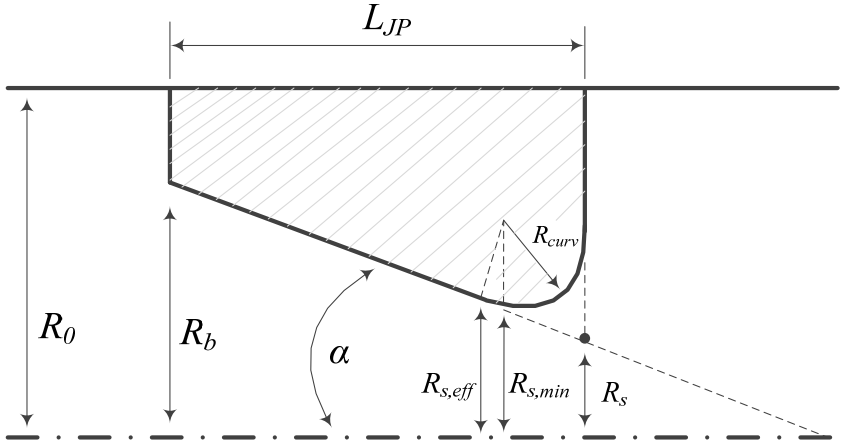

Figure 1.3 Jet pump geometry.

For the case where the flow goes to the right hand side of Figure 1.3, the steady flow formulation for pressure drop across the jet pump can be expressed by:

$$\begin{aligned}\Delta p_{ml} &= \frac{1}{2}\rho K_{exp,s} u_1^2 + \frac{1}{2}\rho K_{cont,b} u_2^2 \\ &= \frac{1}{2}\rho u_1^2 \left(K_{exp,s} + K_{cont,b} \left(\frac{A_{s,min}}{A_b} \right)^2 \right) \\ &= \frac{1}{2}\rho u_1^2 (K_{out})\end{aligned} \tag{1.2}$$

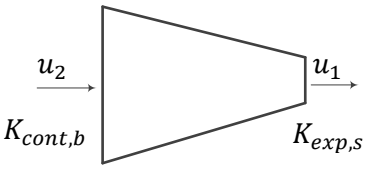

While for the case of the backward flow (to the left hand side of Figure 1.3), the steady flow formulation is:

$$\begin{aligned}\Delta p_{ml} &= \frac{1}{2}\rho K_{cont,s} u_1^2 + \frac{1}{2}\rho K_{exp,b} u_2^2 \\ &= \frac{1}{2}\rho u_1^2 \left(K_{cont,s} + K_{exp,b} \left(\frac{A_{s,min}}{A_b} \right)^2 \right) \\ &= \frac{1}{2}\rho u_1^2 (K_{in})\end{aligned} \tag{1.3}$$

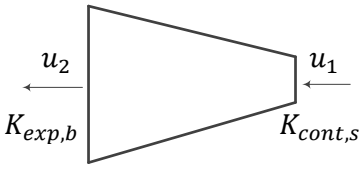

The minor loss coefficient of expansion and contraction K_{exp} and K_{cont} are determined based on the case of steady flow. For the expansion coefficient, the Borda-Carnot formula can be used [7]:

$$K_{exp} = \left(1 - \frac{A_{in}}{A_{out}} \right)^2 \tag{1.4}$$

where A_{in} and A_{out} are the cross-sectional area before and after the expansion, respectively. Thus, in the case of the jet pump in oscillatory flow, the minor loss coefficient from expansion can be written as:

$$K_{exp,s} = \left(1 - \frac{A_{s,min}}{A_0}\right)^2$$
$$K_{exp,b} = \left(1 - \frac{A_b}{A_0}\right)^2 \tag{1.5}$$

The minor loss coefficient for contraction at the jet pump waist is taken to be 0.04 based on the ratio of the radius of curvature R_{curv} and the diameter at the jet pump waist ($2R_{s,min}$) [2]. At the widest cross-section of the jet pump, the minor loss coefficient for contraction was taken to be 0.5 due to the sharp edge of the opening [2]. These values were chosen based on the first jet pump sample design provided by van Dixhoorn [9]. For the purpose of investigating different jet pump geometries, other jet pump samples have been designed based on this sample. The detailed explanation of the jet pump samples is covered in Chapter 3.

For large amplitude oscillatory flow, the pressure drop can be calculated by adding the pressure drop for both steady forward and backward flow:

$$\begin{aligned}\Delta p_{JP} &= \frac{1}{2}\rho K_{out} {u_{JP,max}}^2 - \frac{1}{2}\rho K_{in} {u_{JP,max}}^2 \\ &= \frac{1}{2}\rho {u_{JP,max}}^2 (K_{out} - K_{in})\end{aligned} \tag{1.6}$$

The maximum velocity in the jet pump $u_{JP,max}$ is defined as a volume flow rate $|U_1|_{JP}$ divided by the smallest cross-sectional area $A_{s,min}$. Thus, Equation (1.6) can also be written as:

$$\Delta p_{JP} = \frac{\rho_m {|U_1|_{JP}}^2}{8 {A_{s,min}}^2}\left[\left(K_{exp,s} - K_{cont,s}\right) + \left(\frac{A_{s,min}}{A_b}\right)^2 \left(K_{cont,b} - K_{exp,b}\right)\right] \tag{1.7}$$

This expression can be used to determine the theoretical pressure drop across a jet pump in an oscillatory flow.

These minor loss coefficients drive a second order mean velocity to flow to the right hand side of Figure 1.3 [6]. In order to control the mean velocity flow that suppresses the Gedeon streaming, the minor loss coefficient of a jet pump in oscillatory flow needs to be studied. Three assumptions are used to determine the minor loss coefficient for oscillatory flow. The assumptions are explained as follows:

1. The Iguchi hypothesis assumes that the value of the minor loss coefficient for an oscillatory flow is the same as in steady flow [8]. This implies that the total minor loss coefficient for a jet pump in oscillatory flow is the summation of the minor loss coefficient for the forward flow and backward flow.

2. The minor loss coefficient for expansion of the steady flow can be calculated using the Borda-Carnot formula (Equation (1.5)) and depends only on the cross-sectional area, while the minor loss coefficient for contraction can be obtained as a constant. These values have been tabulated for the steady flow case [2,16,23,31].

3. The relation between pressure drop and velocity amplitude in the jet pump is quadratic, while the power dissipation has a cubic relation. These are based on a quasi-steady model that has been developed by Backhaus and Swift [2] and are used to determine the minor loss coefficient for oscillatory flow. This model will be explained later in Chapter 3.2.

To investigate the applicability of these assumptions, four jet pump samples were made with varied geometries. Several parameters are changed, such as the taper angle and the number of the jet pump holes while keeping the cross-sectional area constant. Pressure and power measurements are conducted for all samples and the effect of different jet pump geometries to the pressure drop will be investigated. A flow visualization experiment was conducted to obtain the flow patterns generated by a jet pump in oscillatory flow. The information on the flow patterns can give a better understanding to interpret the results of pressure and power measurement. This subject will be explained in details in Chapter 3.

1.3. Research goals

To have a better understanding of the jet pump effects, a series of experiments have been performed. These experiments are important in order to verify a numerical simulation results and to give insight for the more complex jet pump geometries which cannot be simulated or require a long duration for the simulation to complete. To summarize, the research goals of this master assignment are:

1. Modifying the standing wave experimental setup into a traveling wave setup.

2. Investigating the effects of different jet pump geometries on the time-averaged pressure drop and power dissipation.

3. Checking the applicability of the three assumptions for oscillatory flow.

4. Visualizing the flow patterns generated by a jet pump in an oscillatory flow.

1.4. Outline of the thesis

This thesis consists of four chapters. The first chapter gives an introduction about the thermoacoustic technology, jet pump principle and the research goals. Chapter 2 discusses about the current experimental setup, the design and realization of a traveling wave setup, and the flow visualization test section. Chapter 3 presents the experimental work and results. Finally, Chapter 4 delivers conclusions and suggestions for further work.

CHAPTER 2

SETUP DESIGN

The experimental setup used in this thesis was originally conceived at the Technical University of Eindhoven [3]. This setup consists of three main parts: the loudspeaker, the main tube and the cone that connects the loudspeaker and the main tube (see Figure 2.1). Due to the hard termination at the end of the main tube, a standing wave builds up in the setup. The standing wave field represents the real condition in a standing wave thermoacoustic device. To represent the condition in a traveling wave thermoacoustic device, a traveling wave should exist in the experimental setup. In order to conduct a traveling wave in the setup, a dedicated termination needs to be designed. For the design of a traveling wave termination, a model is developed. Section 2.2 summarizes the model, the design process and the traveling wave termination testing.

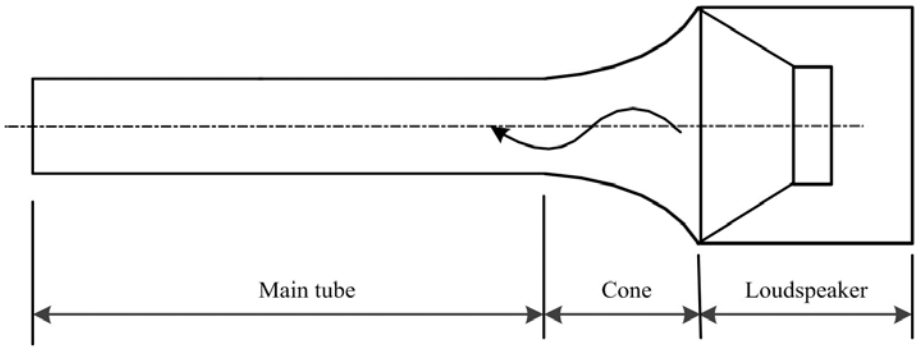

Figure 2.1 Standing wave experimental setup.

Another development of the current setup is the addition of a smoke wire for the flow visualization. Since the main tube consists of multiple aluminum sections that are interchangeable, a new test section can be placed in the middle of the. The test section for mounting the jet pump and for flow visualization was developed in the scope of this thesis. A detailed explanation on the test section is given in section 2.3.

2.1. Existing setup

The three main parts of the experimental setup have been made at the Technical University of Eindhoven, while the supporting frame of these parts is designed and manufactured at the University of Twente, as well as the data acquisition system. For more detailed description of the three main parts of the setup, readers are referred to Aben [3]. The data acquisition system and support design are provided in the thesis of van der Gun [10]. The termination of the main tube can be removed, thus experiments in closed setup and open setup are possible. Both cases represent a standing wave field inside the main tube. The difference lies

on the reflection coefficient: the closed setup has a reflection coefficient of 1 and for the open setup this value is -1 [24]. It implies that the reflected wave has the same phase as the incident wave for the case of closed setup and there is a 180° phase shift between the reflected and incident wave for the open setup.

A transparent tube is needed for the experiment with a jet pump. It has been realized by van Dixhoorn [9] using PMMA material. This PMMA tube acts as a mounting for the jet pump sample as well as the flow visualization test section. The jet pump location in the PMMA tube is indicated by x_{JP} in Figure 2.2. Two holes were made on the PMMA tube for placing the smoke wire and its location is indicated by x_{SW}. Four pressure sensors are used for the experiment and its locations are shown in Figure 2.2.

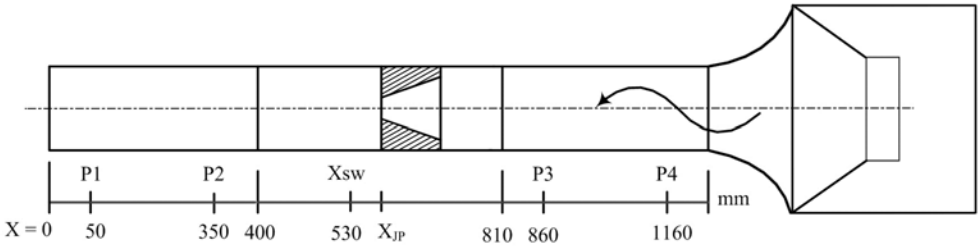

Figure 2.2 Standing wave experimental setup with mounted jet pump test section.

2.2. The traveling wave termination

The existing setup is now able to conduct a standing wave field that represents the condition of a standing wave thermoacoustic device. In order to represent the real condition in a traveling wave thermoacoustic device, a traveling wave should build up inside the setup. Therefore, the current setup needs to be modified.

One method to obtain a traveling wave inside the setup is to use a sound absorbing device. Two classes of sound absorbing structures can be distinguished in general: porous materials and resonance absorbers [11]. Some examples of porous materials are synthetic foams. While using a porous material is considered as a possibility, this will need a certain thickness to obtain total sound absorption. A rule of thumbs states that to totally absorb an acoustic wave, one needs a porous material with thickness more than a quarter of the corresponding wavelength [11]. For a frequency of 100 Hz, the length of porous material should exceed 80 cm which makes it difficult to apply to the experimental setup due to the limitation of the setup mounting rail. Any additional section longer than 80 cm can be attached to the current setup, however it takes bigger effort to construct an extension for the mounting rail. Moreover, the characteristic of the foam depends on the material and foam matrix, which makes it difficult to control the working frequency. Therefore, another way to create a traveling wave by using a resonator is studied. This resonator will be referred as the “traveling wave termination” from this point on.

2.2.1. Theory

The idea of adding a traveling wave termination at the end of the setup is to cancel all reflected wave inside the setup. Consider Figure 2.3 in which the traveling wave termination is attached to the end of the setup. When an incoming wave *f(x,t)* is generated from the

loudspeaker, it will be reflected at the end of the setup (wave $g_2(x,t)$). The incoming wave $f(x,t)$ will also be reflected by the end wall of the traveling wave termination (wave $g_1(x,t)$). Wave $g_2(x,t)$ should have equal amplitude but 180° phase difference to $g_1(x,t)$ so that all reflected wave cancels each other. Therefore, a traveling wave can be modeled in the setup.

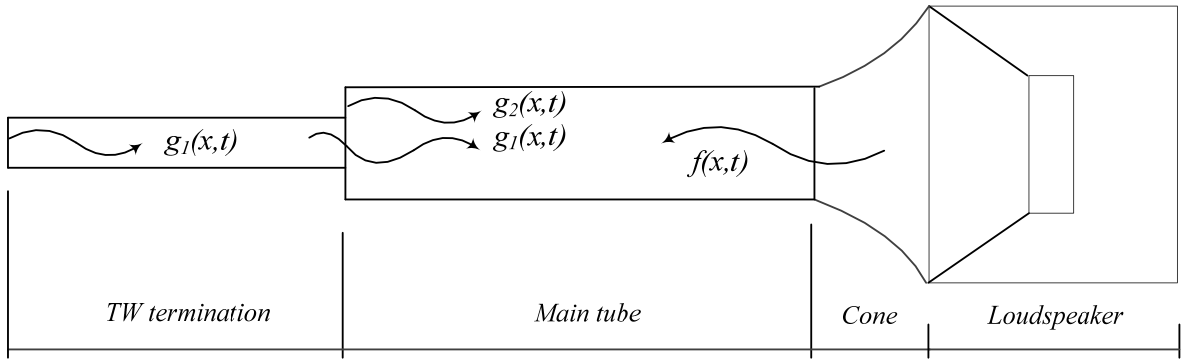

Figure 2.3 Schematic of the working principle of traveling wave termination.

To model the wave propagation inside the main tube and the traveling wave termination, a so-called Low Reduced Frequency Model is studied. The next section will discuss in detail the one-dimensional model that has been developed to design the traveling wave termination.

2.2.1.1. Wave propagation in a cylinder: the Low Reduced Frequency Model

In order to design a traveling wave termination, the wave propagation in a tube should be understood well. Various solutions have been proposed, such as the one by Tijdeman [12]. The Tijdeman's Low Reduced Frequency Model starts from the Navier-Stokes equation for a cylindrical coordinate system. The governing equations are given in the following.

The Navier-Stokes equation:

$$\rho\left[\frac{\partial u}{\partial t}+\ v\frac{\partial u}{\partial r}+\ \ u\frac{\partial u}{\partial x}\right]=\ -\frac{\partial p}{\partial x}+\mu\left\{\left[\frac{\partial^2 u}{\partial x^2}+\frac{\partial^2 u}{\partial r^2}+\frac{1}{r}\frac{\partial u}{\partial r}\right]\ +\frac{1}{3}\frac{\partial}{\partial x}\left[\frac{\partial u}{\partial x}+\frac{\partial v}{\partial r}+\frac{v}{r}\right]\right\} \tag{2.1}$$

$$\rho\left[\frac{\partial u}{\partial t}+\ v\frac{\partial u}{\partial r}+\ \ u\frac{\partial u}{\partial x}\right]=\ -\frac{\partial p}{\partial r}+\mu\left\{\left[\frac{\partial^2 v}{\partial r^2}+\frac{1}{r}\frac{\partial v}{\partial r}-\ \frac{v}{r^2}+\frac{\partial^2 v}{\partial x^2}\right]\ +\frac{1}{3}\frac{\partial}{\partial r}\left[\frac{\partial u}{\partial x}+\frac{\partial v}{\partial r}+\frac{v}{r}\right]\right\} \tag{2.2}$$

The equation of continuity:

$$\frac{\partial \rho}{\partial t}+\ u\frac{\partial \rho}{\partial x}+v\frac{\partial \rho}{\partial r}+\rho\left[\frac{\partial u}{\partial x}+\frac{\partial v}{\partial r}+\frac{v}{r}\right]=0 \tag{2.3}$$

The equation of state for an ideal gas:

$$p=\rho\ R_0 T \tag{2.4}$$

The energy equation:

$$\rho\, C_p \left[\frac{\partial T}{\partial t} + u\frac{\partial T}{\partial x} + v\frac{\partial T}{\partial r}\right] = \lambda\left[\frac{\partial^2 T}{\partial r^2} + \frac{1}{r}\frac{\partial T}{\partial r} + \frac{\partial^2 T}{\partial x^2}\right] + \frac{\partial \rho}{\partial t} + u\frac{\partial p}{\partial x} + v\frac{\partial p}{\partial r} + \mu\phi \tag{2.5a}$$

$$\phi = 2\left[\left(\frac{\partial u}{\partial x}\right)^2 + \left(\frac{\partial v}{\partial r}\right)^2 + \left(\frac{v}{r}\right)^2\right] + \left[\frac{\partial v}{\partial x} + \frac{\partial u}{\partial r}\right]^2 - \frac{2}{3}\left[\frac{\partial u}{\partial x} + \frac{\partial v}{\partial r} + \frac{v}{r}\right]^2 \tag{2.5b}$$

Some dimensionless parameters were introduced by Tijdeman to characterize the Low Reduced Frequency Model, namely the shear wave number, the reduced frequency, the square root of the Prandtl number, and the ratio of the specific heats.

$$s = R\sqrt{\frac{\rho_0 \omega}{\mu}}, \text{ the shear wave number} \tag{2.6}$$

$$k_r = R\frac{\omega}{c_0}, \text{ the reduced frequency} \tag{2.7}$$

$$\sigma = \sqrt{\frac{\mu C_p}{\lambda}}, \text{ the square root of the Prandtl number} \tag{2.8}$$

$$\gamma = \frac{C_p}{C_v}, \text{ the ratio of the specific heats} \tag{2.9}$$

These dimensionless parameters characterize the wave propagation in a tube. The shear wave number, for example, is a good indication to determine the most dominant effect of inertial or viscous forces [11]. In our case, the tube diameter is relatively large compared to the thickness of the viscous boundary layer and the term "wide" tube is introduced. For this case, the shear wave number is larger than one and the inertia effects are more dominant than the viscous effects. The reduced frequency represents the ratio of the characteristic length of the cross-section and the acoustic wavelength. The other two parameters σ and γ depends on the physical properties of the propagation medium. In this thesis, the propagation medium is always air and these values are considered to be constant.

The main assumptions used to simplify the equation are listed in the following:

a. The wavelength is very large compared to the diameter of the tube.

b. Homogenous medium, which means that the wave length and the tube radius must be large in comparison with the mean free path; for air of normal atmospheric temperature and pressure, this condition breaks down for $f > 10^8$ Hz and $R < 10^{-5}$ cm;

c. No steady flow;

d. Small amplitude, sinusoidal perturbation (no circulation and no turbulence);

e. Tube long enough, so that end effects are negligible.

The solution has to satisfy the following boundary conditions:

a. At the rigid tube wall, the axial and radial velocity must be zero. i.e:

$$\text{At } r = R,\ u = 0 \text{ and } v = 0$$

b. The radial velocity must be zero at the tube axis due to the axial symmetry of the problem, i.e:

$$\text{At } r = 0,\ v = 0$$

c. The heat conductivity of the tube wall is large in comparison with the heat conductivity of the fluid, i.e:

$$\text{At } r = R,\ T = 0 \text{ (isothermal walls).}$$

The boundary conditions in the axial direction are specified, e.g. imposing the pressure amplitude at one end where the loudspeaker is located and the pressure amplitude at the other end. To obtain the solution for this model, Equation (2.1) – (2.5) are simplified by substituting the relevant variables as shown in the following equations.

$$u = c_0\, u(x,r)e^{i\omega t} \tag{2.10}$$

$$v = c_0\, v(x,r)e^{i\omega t} \tag{2.11}$$

$$p = p_s\left[1 + p(x,r)e^{i\omega t}\right] = \frac{\rho_s c_0^2}{\gamma}\left[1 + p(x,r)e^{i\omega t}\right] \tag{2.12}$$

$$\rho = \rho_s\left[1 + \rho(x,r)e^{i\omega t}\right] \tag{2.13}$$

$$T = T_s\left[1 + T(x,r)e^{i\omega t}\right] \tag{2.14}$$

Dimensionless coordinates are used, namely $\xi = \omega x/c_0$ and $\eta = r/R$ (see Figure 2.4). When the internal tube radius is small compared to the wave length and the radial velocity component, *v* is small compared to the axial velocity, *u.* Then, $\omega x/R_0 \ll 1$ and $v/u \ll 1$, hence Equation 2.1 to 2.5 can be simplified.

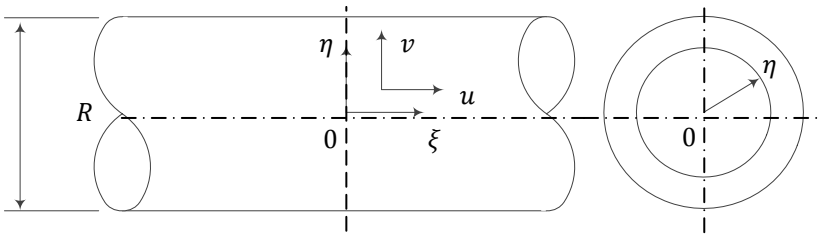

Figure 2.4 Dimensionless coordinates ξ and η.

The five equations are then linearized, where all the higher order terms are neglected due to the assumption of small perturbation. Thus, the solutions of the Low Reduced Frequency Model are mentioned in Equation (2.15) – (2.21).

$$p = A\, e^{\Gamma\xi} + B\, e^{-\Gamma\xi} \tag{2.15}$$

where A and B are the pressure amplitude of the backward and forward travelling wave respectively. The pressure amplitudes are obtained from the boundary conditions in the axial direction. The propagation constant Γ and polytrophic coefficient n are expressed in Equation (2.16) – (2.17).

$$\Gamma = \sqrt{\frac{J_0(i^{3/2}s)}{J_2(i^{3/2}s)}}\ \sqrt{\frac{\gamma}{n}} \tag{2.16}$$

$$n = \left[1 + \frac{\gamma - 1}{\gamma}\frac{J_2(i^{3/2}\sigma s)}{J_0(i^{3/2}\sigma s)}\right]^{-1} \tag{2.17}$$

$$u = \frac{i\Gamma}{\gamma}\left[1 - \frac{J_0(i^{3/2}\eta s)}{J_0(i^{3/2}s)}\right]\left[A\, e^{\Gamma\xi} - B\, e^{-\Gamma\xi}\right] \tag{2.18}$$

$$v = ik\left[\frac{1}{2}\eta\left\{1 + \frac{J_0(i^{3/2}s)}{J_2(i^{3/2}s)}\frac{\gamma}{n}\right\} + \frac{\gamma - 1}{i^{3/2}\sigma s}\frac{J_1(i^{3/2}\sigma\eta s)}{J_0(i^{3/2}\sigma s)} - \frac{\gamma}{i^{3/2}\eta s}\frac{J_1(i^{3/2}\eta s)}{J_2(i^{3/2}s)}\right]\left[A\, e^{\Gamma\xi} + B\, e^{-\Gamma\xi}\right] \tag{2.19}$$

$$\rho = \left[1 - \frac{\gamma - 1}{\gamma}\left\{1 - \frac{J_0(i^{3/2}\sigma\eta s)}{J_0(i^{3/2}\sigma s)}\right\}\right]\left[A\, e^{\Gamma\xi} + B\, e^{-\Gamma\xi}\right] \tag{2.20}$$

$$T = \frac{\gamma - 1}{\gamma}\left[1 - \frac{J_0(i^{3/2}\sigma\eta s)}{J_0(i^{3/2}\sigma s)}\right]\left[A\, e^{\Gamma\xi} + B\, e^{-\Gamma\xi}\right] \tag{2.21}$$

2.2.1.2. The one-dimensional model of a coupled tube

The goal of this thesis is to model the coupling of the main tube and the traveling wave termination, then to obtain the absorption coefficient as close as possible to one. To achieve this goal, a one-dimensional model of van der Eerden [11] is used. This model uses the Low Reduced Frequency Solution for velocity and pressure perturbation. The one-dimensional solution for velocity and pressure perturbation is then used to model two tubes in series. The model solves for the velocity, pressure perturbation and the reflection coefficient at both tubes, as well as the absorption coefficient.

The one-dimensional solution for velocity and pressure perturbation in a tube is mentioned in Equation (2.22) and (2.23).

$$p(x) = \hat{p}_A e^{\Gamma k x} + \hat{p}_B e^{-\Gamma k\, x} \tag{2.22}$$

$$u(x) = \frac{G}{\rho_0 c_0}\left(\hat{p}_A e^{\Gamma k x} - \hat{p}_B e^{-\Gamma k x}\right) \tag{2.23}$$

where $\hat{p}_A$ and $\hat{p}_B$ are the complex pressure amplitudes of the backward and forward propagating wave, respectively.

A parameter G which depends on the cross-sectional shape of the tube is introduced in Equation (2.24). The wave propagation constant Γ depends on the shear wave number. For a cylindrical tube, the wave propagation constant Γ and polytrophic coefficient n are formulated as in Equation (2.25) – (2.26).

$$G = -\frac{i}{\Gamma}\frac{\gamma}{n} \tag{2.24}$$

$$\Gamma = \sqrt{\frac{J_0(i^{3/2}s)}{J_2(i^{3/2}s)}\frac{\gamma}{n}} \tag{2.25}$$

$$n = \left(1 + \frac{\gamma - 1}{\gamma}\frac{J_2\left(i^{3/2}s\sigma\right)}{J_0(i^{3/2}s\sigma)}\right)^{-1} \tag{2.26}$$

Another approximation was derived by Kirchhoff for large values of shear wave number s ($s > 4$) [12]. Based on Equation (2.15)-(2.21), a first order approximation can be used for the calculation of a large tube. Both viscous and thermal effects are also considered through the shear wave number s and σ. Then, Γ and G can be written as:

$$\Gamma = i + \frac{i+1}{\sqrt{2}}\left(\frac{\gamma - 1 + \sigma}{s\sigma}\right) \tag{2.27}$$

$$G = -\frac{i}{\Gamma} \tag{2.28}$$

Since $s > 4$ occurs in this thesis, the Kirchhoff approximation was used for further calculations.

The one-dimensional solution for a single tube is then used to model two tubes connected in series. A transfer function is needed to couple the individual expression in order to model the boundary of the two connecting tubes. It is assumed that there is an imaginary volume in between them, where the mass in conserved. This imaginary volume is only used for a better understanding of the inflow and outflow of the two tubes.

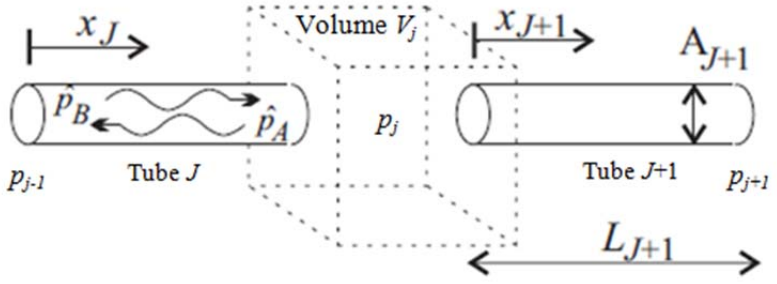

Figure 2.5 Two tubes connected with a volume in between [11].

Each tube has its own coordinate system, x_J and x_{J+1} with the index J refers to the number of the tube. The index j indicates three points in the coupled tubes: one at the inlet of the first tube, one at the junction of the two tubes where the imaginary volume exists, and one point at the end of the second tube. The length of the tube is indicated by L and its cross-sectional area is expressed as A.

The transfer function that couples the two tubes can be obtained by the mass balance in the volume V_J. The change of mass in V_J must be equal to the difference of mass entering V_J and mass leaving V_J. If the mass flow is indicated by Q, then the mass balance equation is:

$$\frac{dm_V}{dt} = \left(Q_J(x_J = L_J) - Q_{J+1}(x_{J+1} = 0)\right) e^{i\omega t} \tag{2.29}$$

The pressure perturbation in the volume is assumed to be constant. For small value of the pressure perturbation and the density perturbation, the polytrophic relation applies as follow:

$$\rho = \frac{p}{(c_0)^2}\frac{\gamma}{n_V} \tag{2.30}$$

where n_V is the polytrophic coefficient for a volume and is formulated similarly as in Equation (2.26).

Hence, the time-dependent mass m_V can be written as:

$$m_V = V_j\left(\rho_0 + \frac{p}{(c_0)^2}\frac{\gamma}{n_V}\right) e^{i\omega t} \tag{2.31}$$

The mass flow that enters V_J is expressed as a function of the density, the cross-section area of the tube J, and the velocity entering V_J. The same expression can be derived for the tube $J+1$. Equation (2.32) shows the mass flow that enters and leaves V_J, respectively.

$$Q_J(x_J = L_J) = A_J\rho_0 u(x_J = L_J) \text{ and } Q_{J+1}(x_{J+1} = 0) = A_{J+1}\rho_0 u(x_{J+1} = 0) \tag{2.32}$$

Other equation is needed to couple the mass balance with the pressure at both ends of the tube. The boundary conditions at both ends of the tube are applied and the complex amplitude of the reflected and incident wave can be determined. Using the formulation of Bergh and Tijdeman [13] results in the derived complex pressure amplitudes for tube J and $J+1$.

$$\hat{p}_{AJ} = \frac{p_j - p_{j-1}e^{(-\Gamma kL)_J}}{e^{\Gamma kL_J} - e^{-(\Gamma kL)_J}} \tag{2.33a}$$

$$\hat{p}_{BJ} = \frac{-p_j + p_{j-1}e^{(\Gamma kL)_J}}{e^{(\Gamma kL)_J} - e^{-(\Gamma kL)_J}} \tag{2.33b}$$

$$\hat{p}_{AJ+1} = \frac{p_{j+1} - p_j e^{(-\Gamma kL)_{J+1}}}{e^{(\Gamma kL)_{J+1}} - e^{-(\Gamma kL)_{J+1}}} \tag{2.34a}$$

$$\hat{p}_{BJ+1} = \frac{-p_{j+1} + p_j e^{(\Gamma kL)_{J+1}}}{e^{(\Gamma kL)_{J+1}} - e^{-(\Gamma kL)_{J+1}}} \tag{2.34b}$$

From Equation (2.29), (2.32), (2.33) and (2.34), it follows that the recursive formulation for the coupled tube is:

$$\frac{p_j}{p_{j-1}} = \left[\cosh(\Gamma kL)_J + \frac{\sinh(\Gamma kL)_J}{A_J G_J}\left(-\frac{ik\gamma}{n_V}V_j + \frac{A_{J+1}G_{J+1}}{\sinh(\Gamma kL)_{J+1}}\left\{\cosh(\Gamma kL)_{J+1} - \frac{p_{j+1}}{p_j}\right\}\right)\right]^{-1} \tag{2.35}$$

Next, using the chain rule, the transfer function for coupling the tubes can be written as:

$$\frac{p_{j+1}}{p_{j-1}} = \frac{p_{j+1}}{p_j}\frac{p_j}{p_{j-1}} \tag{2.36}$$

In a case when the two tubes are directly coupled in series, then $V_j = 0$. In our case, the transfer function formula for the main tube is exactly as equation (2.35) without the

$\left((-ik\gamma/n_V)\,V_j\right)$ term. The transfer function for the traveling wave termination follows from the equation for a tube ended with an acoustically hard wall, Equation (2.37).

$$\frac{p_j}{p_{j-1}} = \left[\cosh(\Gamma kL)_J\right]^{-1} \tag{2.37}$$

Equation (2.35) and (2.37) are rewritten for the main tube and the traveling wave termination in the following. The index 0, 1 and 2 refer to the inlet of the main tube, the junction, and the end wall of the termination.

$$\frac{p_1}{p_0} = \left[\cosh(\Gamma kL)_1 + \frac{\sinh(\Gamma kL)_1}{A_1 G_1}\left(\frac{A_2 G_2}{\sinh(\Gamma kL)_2}\left\{\cosh(\Gamma kL)_2 - \frac{p_2}{p_1}\right\}\right)\right]^{-1} \tag{2.38}$$

$$\frac{p_2}{p_1} = \frac{1}{\cosh(\Gamma kL)_2} \tag{2.39}$$

Using the transfer function in Equation (2.38) and (2.39), and the pressure at the inlet of the main tube, p_1 and p_2 can be calculated by the following equations.

$$p_1 = \frac{p_1}{p_0}\, p_0 \tag{2.40}$$

$$p_2 = \frac{p_2}{p_1}\, p_1 \tag{2.41}$$

Substituting p_1 and p_2 into Equation (2.22) results in two equations with two unknown variables, $\hat{p}_A$ and $\hat{p}_B$. Substituting $\hat{p}_A$ from one equation to the other results in $\hat{p}_B$, hence both variables can be calculated.

After obtaining the pressure amplitudes of the forward and backward traveling wave for both tubes, the reflection coefficient in both tubes can be obtained as well.

$$R(x) = \frac{\hat{p}_A e^{\Gamma kx}}{\hat{p}_B e^{-\Gamma k\, x}} \tag{2.42}$$

Then the absorption coefficient for each tube can be calculated with the following equation.

$$\alpha(x) = 1 - |R|^2 \tag{2.43}$$

To conduct a traveling wave inside the setup, it is desired to have an absorption coefficient of 100 %. By combining the cross-sectional area A (or radius R) and length L of the traveling wave termination, one can calculate the absorption coefficient for a specific frequency.

The theory derived in this section is applied to make a model of two connected tubes: the main tube and the traveling wave termination. For validation of the implementation, the model is run with the same parameters as mentioned by van der Eerden [11] first. The results are compared to the one obtained by van der Eerden and are discussed in Appendix A. Then, the model is used to design a traveling wave termination for 100 Hz.

2.2.2. Design of traveling wave termination

The model is then used to design a traveling wave termination for the current experimental setup. In this case, some parameters are defined based on the available dimension of the main tube. The working frequency is specified to be 100 Hz and the inner diameter of the main tube is 0.03 m.

The outcomes of the model implementation are the traveling wave termination length and diameter. The design process was done in accordance with the flowchart in Figure 2.6.

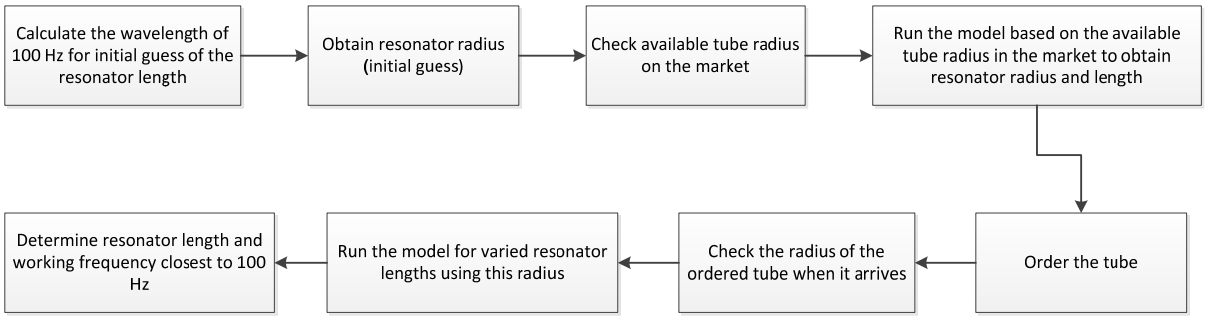

Figure 2.6 The traveling wave termination design process.

The design limitations are listed in Table 2.1.

Table 2.1 Design limitations.

Parameter	Limitation
Traveling wave termination length	0.8 m. The shorter will be favorable.
Working frequency	100 Hz, or as close as possible.
Absorption coefficient	≈ 1

The first step is determining the length of the traveling wave termination based on the wavelength of 100 Hz. Thus, the length of a quarter-wave is 0.85 m. Using this value, the model was run for different inner radii of the traveling wave termination, as depicted in Figure 2.7.

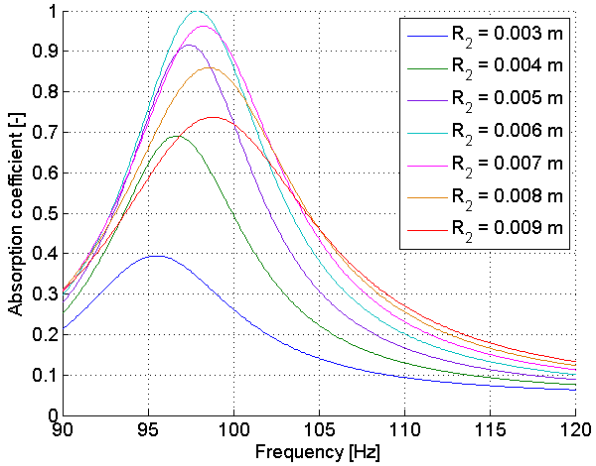

Figure 2.7 Result of frequency sweep for constant $L_{g,2} = 0.85\ m$ with applied end correction.

Table 2.2 List of working frequency and absorption coefficient for varied radii.

R_2 [m]	Working frequency [Hz]	α [%]
0.003	95.5	39.43
0.004	96.7	69.05
0.005	97.4	91.54
0.006	97.9	99.91
0.007	98.3	96.18
0.008	98.5	85.92
0.009	98.8	73.69

From Figure 2.7 and Table 2.2, it can be concluded that the radius of the traveling wave termination would be 0.006 m and the length is 0.85 m. The operating frequency is not precisely 100 Hz, however this value can be tuned later by varying the length because the length is the most important parameter to tune the resonator for a specific frequency [11]. In this case, the radius is the limiting parameter because it depends on the manufacturer, while the length can be adjusted easily by cutting. Thus, the selection of tube radius should be done first and then the length can be determined later when the tube arrives.

The selection of the tube material should be done by considering the length of the tube. Since the traveling wave termination is supported only at the two ends, the material should have a high Young's modulus and area moment of inertia to prevent them from bending. Aluminum was chosen because it meets the criteria [10] and it was available at the moment. The wall thickness is 2 mm and it is deemed sufficiently rigid.

The inner diameter of the ordered tube was measured using a three-point micrometer. The tube inner diameter is 11.97 mm. Thus, the model was recalculated using this diameter. The aim is to achieve the highest absorption coefficient for the shortest length possible and a working frequency as near as possible to 100 Hz. The model was run again for different lengths and the results are plotted in Figure 2.8. It was decided to choose a length of 0.737 m.

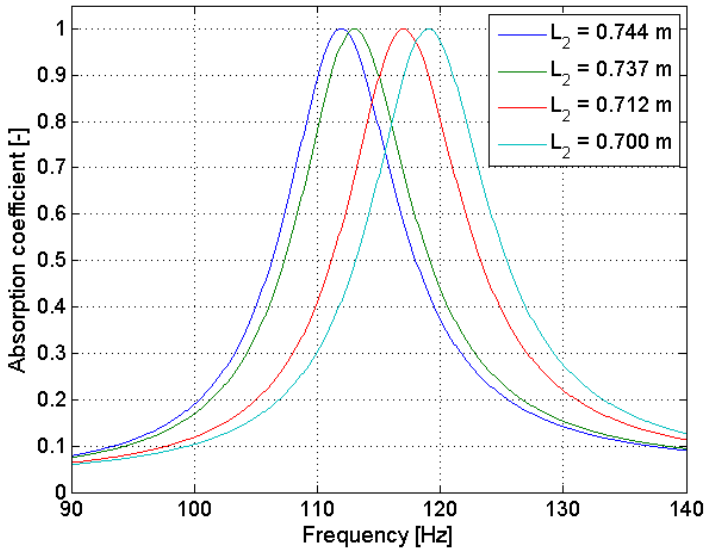

Figure 2.8 Result for constant $R_{i,2} = 0.005985\ m$.

Table 2.3 List of working frequency and absorption coefficient for varied tube length.

L_2 [m]	Working frequency [Hz]	α [%]
0 744	112	99.992
0.737	113	99.999
0.712	117	99.990
0.700	119	99.978

From Figure 2.8, it can be seen that different lengths of the tube does not significantly affect the absorption coefficient, e.g. increasing the length of 4 cm still leads to absorption coefficient very close to one. A sensitivity study about the effect of length and radius to the absorption coefficient and its working frequency is presented in Appendix A.

Finally, the final design of the traveling wave termination is listed in Table 2.4.

Table 2.4 Final design of the traveling wave termination.

Parameter	Value	Unit
Frequency	113	Hz
Inner radius	0.005985	m
Length	0.737	m
Reflection coefficient	0.003564	-
Absorption coefficient	99.999	%

To make sure that the traveling wave termination works perfectly, the model was run to obtain the pressure perturbation, phase and pressure amplitude at both tubes. Figure 2.9(a) and (b) give, respectively, the pressure perturbation and the phase information inside both tubes. For example, in the main tube, it can be seen from Figure 2.9(a) that the pressure perturbation is constant while the phase changes linearly (Figure 2.9(b)). The constant pressure perturbation and constant change of phase indicate the traveling wave in the main tube. While inside the traveling wave termination, it is shown that there is increasing pressure amplitude and an almost constant phase. The constant phase signifies that a standing wave is present inside the traveling wave termination.

Figure 2.9(c) gives more detail information to confirm that there is a forward traveling wave inside the main tube. There is an incident wave of 1 Pa while the reflected wave is close to zero. Moreover, Figure 2.9(d) also confirms that the forward and backward traveling wave behave similarly. The negative linear gradient shows that there is decay on pressure amplitude of the forward wave, followed by the same decay for the reflected wave.

The model confirms that a traveling wave exist in the experimental setup. The radius and the length of the resonator are obtained, hence the traveling wave termination can be manufactured.

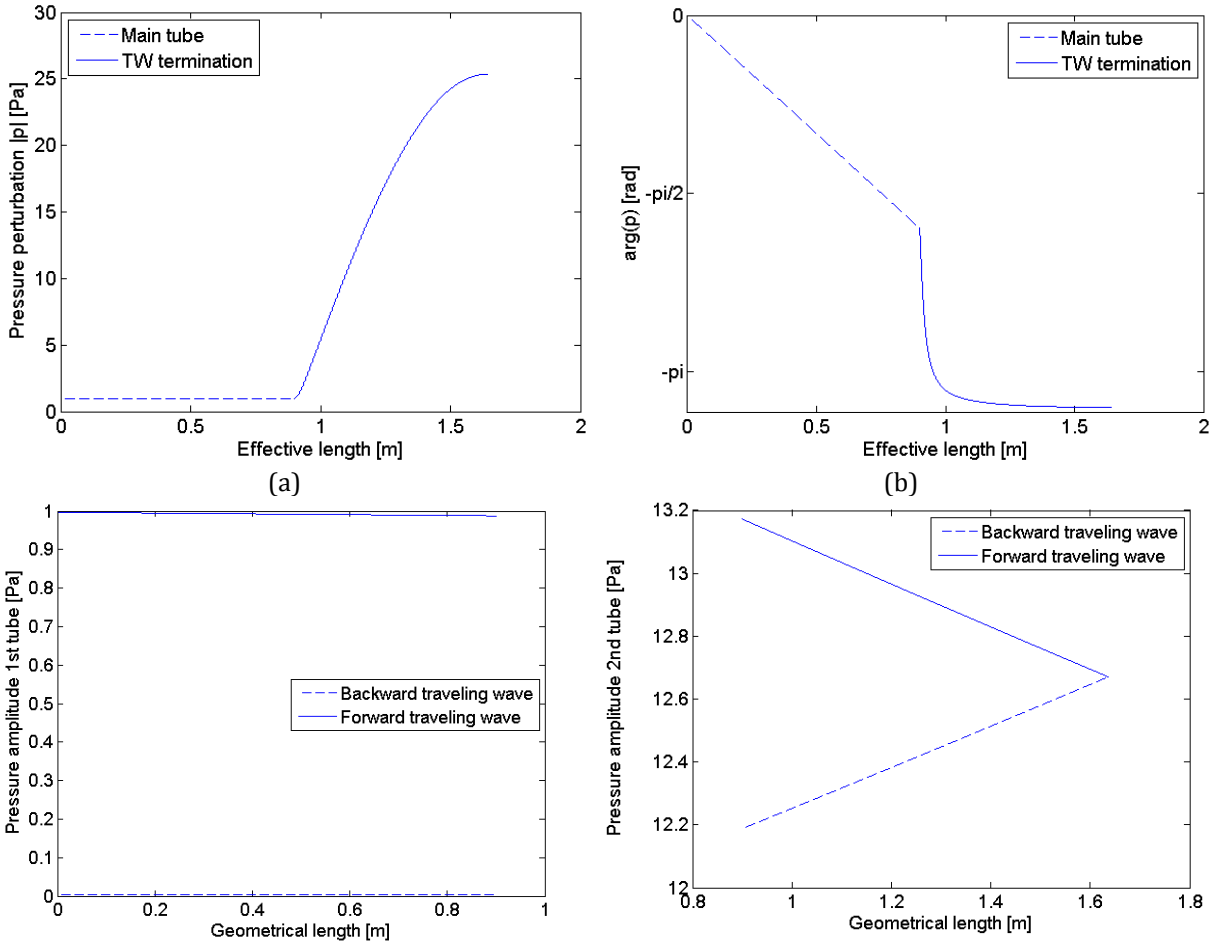

Figure 2.9 Results obtained at 113 Hz for the final design of the traveling wave termination: (a) Pressure perturbation, (b) phase, and pressure amplitude at (c) main tube and (d) traveling wave termination.

Aside from obtaining the final design of the traveling wave termination, the model was also run to know the temperature effect. The ambient temperature could change and result in different air properties. Thus, the working frequency may be changed as well as the absorption coefficient. To understand the temperature effect, the model was used to plot the R-f curve for different temperatures. Note that the previous results were performed at a temperature of 20°C.

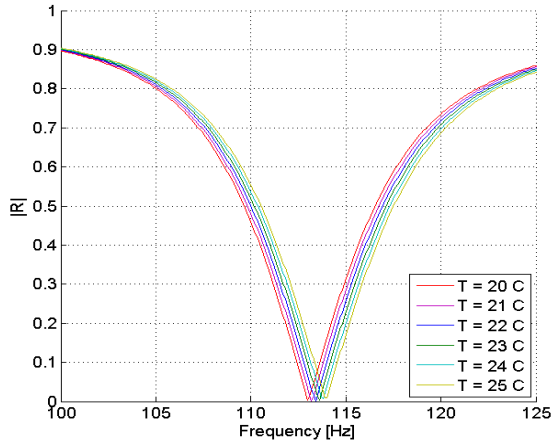

Figure 2.10 The temperature effects.

Table 2.5 List of working frequencies at specified temperature.

T (°C)	Minimum |R|	f (Hz)	α (%)
20	0.003564	113.0	99.9987
21	0.001054	113.2	99. 9999
22	0.001507	113 .4	99.9998
23	0.004095	113.6	99 9983
24	0.006724	113.8	99.9955
25	0.009389	114.0	99.9912

(Modeled for $R_2 = 0.005985\ m$ and $L_{g,2} = 0.737\ m$)

Figure 2.10 indicates that there is a shift in frequency corresponds to the minimum reflection coefficient for different temperature conditions. Increasing temperature of 5°C could result in a frequency shift of 1 Hz, while the absorption coefficient stays around 99.99%.

2.2.3. Manufacture and testing

Once the traveling wave termination was built, a series of experiments was conducted to test its performance. Three different set of experiments were done: (1) frequency sweep at pressure amplitude of 100 Pa and 600 Pa, (2) pressure amplitude sweep at 113 Hz, and (3) experiments using a jet pump sample. The frequency sweep was done to obtain the value of the reflection coefficient (and subsequently, absorption coefficient) as well as the working frequency where this value is minimum. Pressure amplitude of 100 Pa was chosen to match with other numerical research outside the scope this thesis, while 600 Pa was chosen to check the consistency of the result at 100 Pa. The second experiment was done by varying the pressure amplitude and keeping the frequency constant. The effect of pressure amplitude to the absorption coefficient is studied. The third experiment use a jet pump sample to make sure that the traveling wave termination can still conduct a traveling wave inside the setup. The addition of a jet pump could create more reflected wave and could result in a lower absorption coefficient.

The frequency sweep was done by keeping the pressure amplitude at sensor P2 (see Figure 2.11) constant. The sensor was chosen based on its location near the end of the setup, thus near a pressure antinode. Sensor P1 is favorable, however it is located nearer to the junction where the flow may be affected by the inlet effect at the entrance of the traveling wave termination. Therefore, pressure sensor 2 was chosen instead.

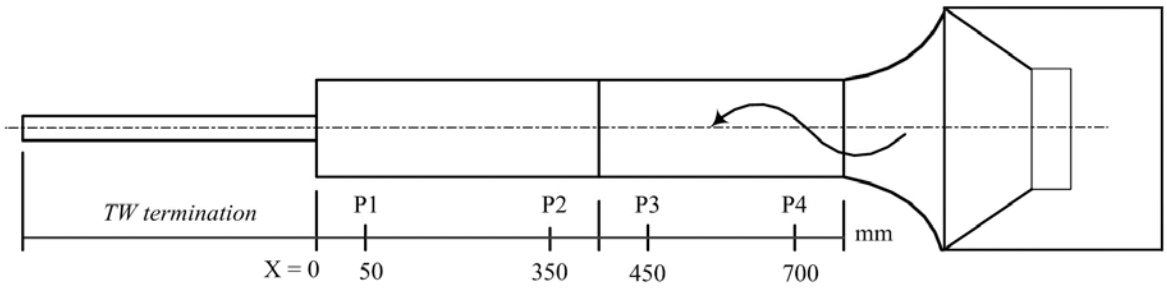

Figure 2.11 Pressure sensor locations in the traveling wave experimental setup.

In performing a frequency sweep, frequency resolution is one important parameter to be considered. In the data acquisition system, a Fourier Transform is used to transform signals between time domain and frequency domain. From the Fourier Transform, the phase and pressure amplitude can be obtained. The distance between adjacent frequency values in which the Fourier Transform is calculated is called the frequency resolution [26]. This parameter depends on the sampling frequency f and the number of samples N, as formulated in Equation (2.44).

$$df = \frac{f_s}{N} \tag{2.44}$$

The sample rate used for data acquisition was 20000 Hz with number of sample of 20000. Thus, the frequency resolution for the Fourier Transform is 1 Hz. This resolution is deemed sufficient for the frequency sweep since the frequency is changed for 1 Hz during the experiment.

The experimental data are recorded every second for two minutes before the frequency is changed. Therefore, for one frequency, there are approximately 120 data points obtained. The data points are selected based on the deviation of pressure amplitude between one data points to the next one. If the deviation is smaller than the tolerance value, the data point is selected and is grouped based on its frequency. The selected data points were averaged and plotted against the respective frequency. The standard deviation can be calculated and the error bar is defined as accumulation of the standard deviation from the measurement, the typical error for the pressure sensors, and calibration error. Figure 2.12 shows the result of data processing with the vertical error bar displayed for each data point.

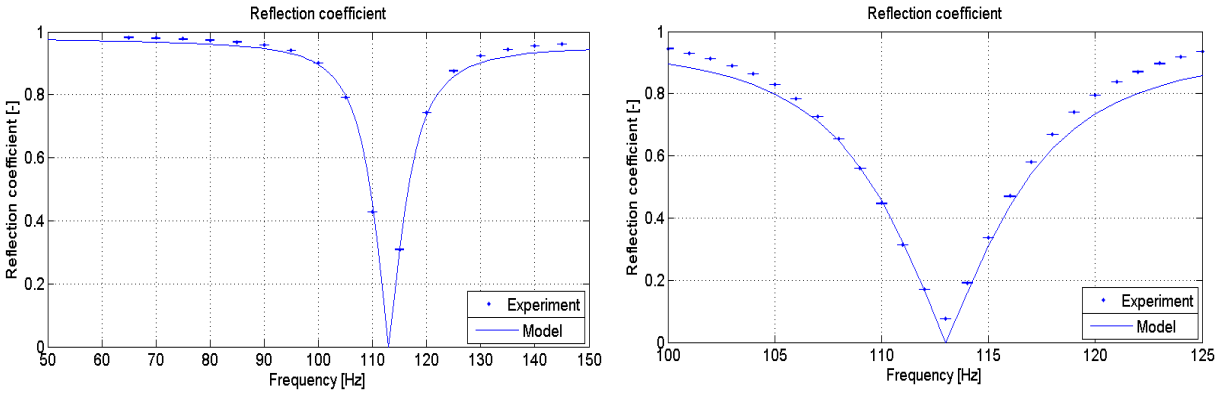

(a) Frequency sweep from 50 to 150 Hz with increment of 5 Hz.

(b) Frequency sweep from 100 to 125 Hz with increment of 1 Hz.

Figure 2.12 Result of frequency sweep at pressure amplitude of 100 Pa.

It is concluded that the reflection coefficient can be predicted by the model. The error bars that represent the standard deviation are small for each data point. There are some differences between the experimental result and the model; the most important is the value of the minimum reflection coefficient at 113 Hz. These differences could be caused by imperfection or nonlinear effects. The imperfection of the traveling wave termination refers to the inner diameter of the tube. To know the dimension of the inner diameter, the measurement was performed only at both ends of the tube. The ends of the tube may be affected by the cutting process, hence the diameter could change. Moreover, the inner diameter of the tube may not be constant over the length. Another possible reason for higher reflection is that the nonlinear effects take place.

Since the developed model is linear, it neglects higher order terms such as higher harmonics and these could lead to additional reflection. The higher harmonics phenomenon was observed by Gaitan and Atchley [27]. The generation of higher harmonics could cause nonlinear waveforms and its effects are highest near the resonance frequency [1]. Higher harmonics can also interact together to form shock waves. Their measurement indicates that 20% of the acoustic power is dissipated due to higher harmonics. Other nonlinear effect can exist in the form of flow disruptions. A turbulence flow can arise due to abrupt changes in the cross-section of the channel, which leads to flow separation and vortex shedding [1]. Thus, flow disruption may occur in the junction of the traveling wave termination where there is abrupt change in the cross-sectional area.

In conclusion, the reflection coefficient at 113 Hz is 0.04 which is 10 times higher than predicted by the model. However, this value is acceptable because it is small enough to lead to absorption coefficient of 99.999%.

To make sure that the minimum reflection occurs at 113 Hz, a second frequency sweep experiment was performer at higher pressure amplitude, 600 Pa. Figure 2.13 shows the experimental result at 600 Pa. The minimum reflection occurs at 113 Hz, however the value is three times higher compared to the one of 100 Pa. From this experiment, it was also known that the pressure amplitude does not give any effect on the frequency corresponds to the minimum reflection coefficient, but it affects the value of the minimum reflection coefficient.

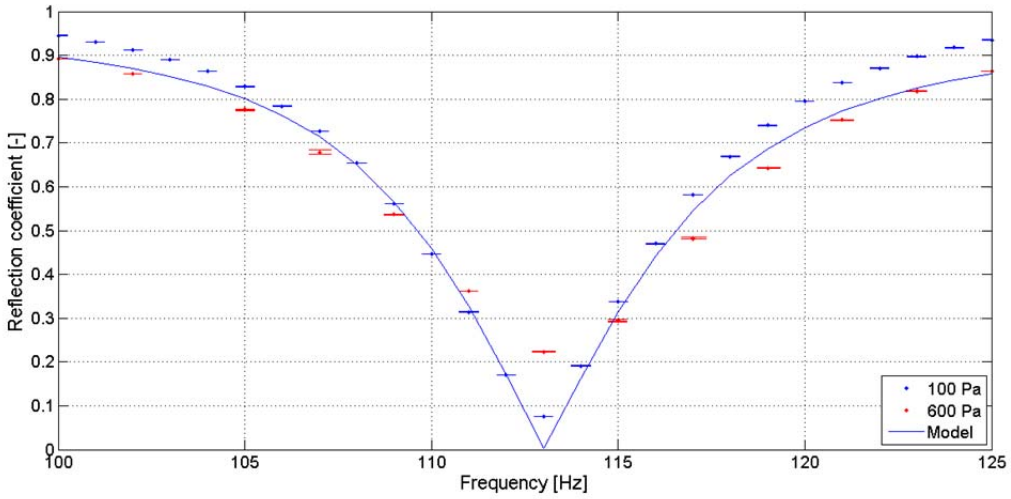

Figure 2.13 Result of frequency sweep at pressure amplitude of 600 Pa.

The higher value of the minimum reflection coefficient at higher pressure amplitude motivates the second experiment. In this experiment, the frequency was kept constant while the pressure amplitude was changed. Two experiments were conducted to see the repeatability and the results are depicted in Figure 2.14. The pressure amplitude sweep reveals that the reflection coefficient increases nonlinearly with increasing pressure amplitude. This behavior could be caused by nonlinear effects as explained before. The nonlinear effects occur at high amplitude so that the linear approximation cannot be used to represent the actual condition anymore [3]. This is confirmed by the fact that at higher pressure amplitude, the model increasingly diverges from the experimental results.

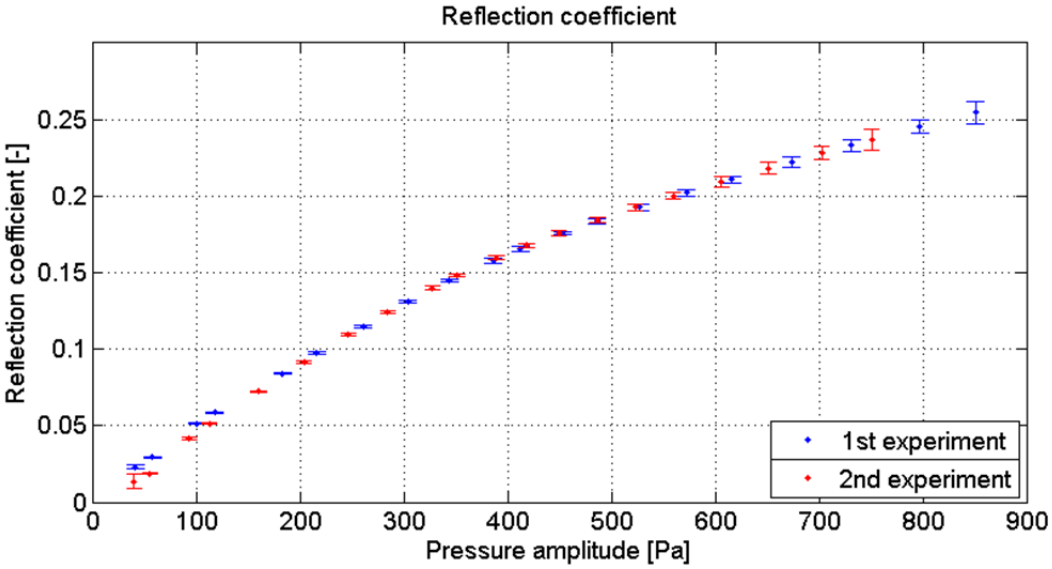

Figure 2.14 Result of pressure amplitude sweep at 113 Hz.

From this set of experiments, it can be concluded that higher pressure amplitudes lead to higher reflection coefficient. Hence one can determine the operational range of the experimental setup from Figure 2.14. While experiment in higher pressure amplitude would be favorable for further studies, it is also limited by the increasing reflection coefficient. To reduce the reflection coefficient at high pressure amplitude, experiment with foam attached to the junction of the traveling wave termination was performed. The utilization of foam does not succeed to reduce the reflection coefficient and readers a referred to Appendix A for the result of this experiment.

The third set of experiment uses a jet pump sample to investigate the effect of the jet pump to the performance of the traveling wave termination. The purpose of this experiment is to make sure that the traveling wave termination conducts a traveling wave inside the setup with a mounted jet pump. The addition of a jet pump can create more reflected wave and this causes more standing wave component in the setup. To investigate this, the wave phasing of the pressure amplitude at two sensor locations are studied.

The jet pump sample used for this experiment is a single hole 7° jet pump with orientation as depicted in Figure 2.15 (other jet pump samples are introduced in Chapter 3.1). The closed and traveling wave terminations were chosen to conduct a standing wave and traveling wave inside the setup. The interest of this experiment lies on the phase difference between two pressure sensors at the section after the jet pump (left hand side of Figure 2.15).

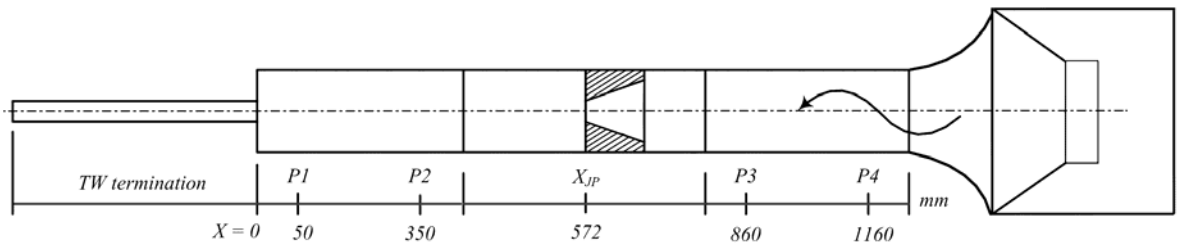

Figure 2.15 Jet pump and pressure sensor locations in the experimental setup.

A pressure amplitude sweep was performed at 113 Hz and the resulting phase difference between sensor P1 and P2 are shown in Figure 2.16.

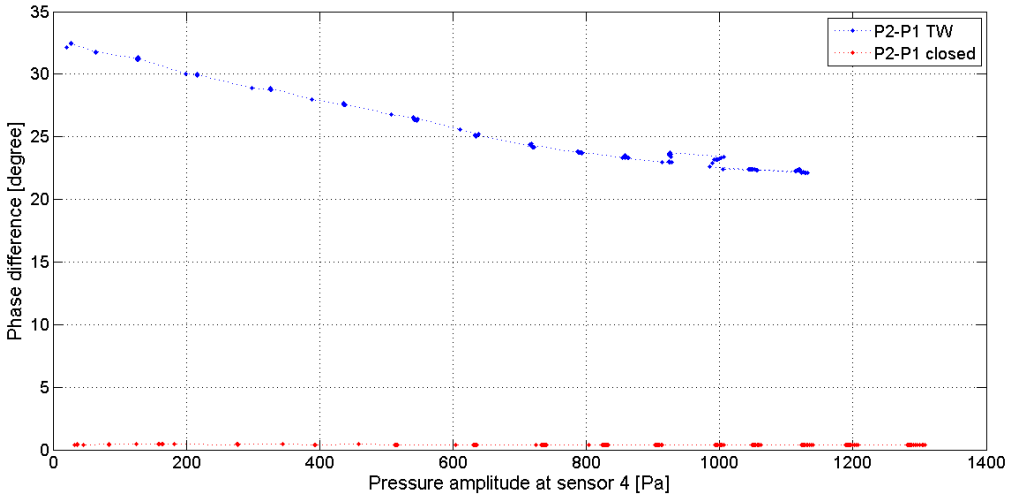

Figure 2.16 Phase difference between setup with closed and traveling wave termination.

The phase difference between two pressure sensors separated by 0.3 m for a frequency of 113 Hz is 35.6° for a pure traveling wave. The phase difference for a pure standing wave is zero. From the experimental results, the setup with closed termination results in a phase difference almost zero, thus a standing wave builds up in the setup. The setup with traveling wave termination gives phase difference higher than 30° for pressure amplitude of 100 Pa. This indicates that almost a pure traveling wave builds up in the setup.

Second remark from Figure 2.16 is the decreasing phase difference at higher amplitude for the setup with traveling wave termination. This behavior is in accordance with the result of pressure amplitude sweep for empty setup (Figure 2.14). At higher pressure amplitude, the reflection coefficient increases while the phase difference decreases due to nonlinear effects. The higher pressure amplitude leads to more reflected wave in the setup which contributes to add more standing wave component, hence a lower phase difference and higher reflection coefficient.

In conclusion, the traveling wave termination can generate traveling wave with the jet pump mounted in the setup. Nonlinear behavior at high pressure amplitude was observed in terms of reflection coefficient and phase difference. The traveling wave termination works best at 113 Hz with absorption coefficient of 99.9%.

2.3. Flow visualization

The developed flow visualization test section is described in this chapter. The equipment needed for visualizing the flow such as the smoke wire, the PMMA tube and the high-speed camera is described. The selection of the smoke wire and smoke liquid, as well as the lighting position is presented in this section.

2.3.1. Theory

The flow visualization method used in this thesis is based on the technique of marking flow lines by means of smoke. Smoke visualization is a standard experimental tool for wind tunnel facility and it is suitable to be applied for visualizing gas movement [16]. Merkli and Thomann [17] and Ingard and Labate [18] are some examples that have succeed in applying the smoke visualization method in oscillatory flow. This method will be applied to the experimental setup in order to observe the flow pattern generated by a jet pump in oscillatory flow. The flow pattern could give a better understanding on the behavior of the flow and this information could be useful to interpret the result of pressure measurement later on.

In principle, the smoke is generated and is fed into the gas flow, hence visualizes the pattern of the flow. There are two methods to use the smoke, the first one is by generating smoke to be carried away by the entire flow field and utilizing a light sheet that cuts across the three-dimensional flow. This illumination in the form of a light sheet has become the most common way for illuminating the flow field [16]. The smoke particles reflect the light to be captured by the recording device. The recording device is positioned in a plane parallel to the two-dimensional light sheet. As the light is reflected into the recording device by the smoke particles, a black background should be provided to give a high contrast. This method has been applied in the experimental setup previously and the readers are referred to the work of Lamboo [28] for an orifice in oscillatory flow and van Dixhoorn [9] for a jet pump in oscillatory flow. Some difficulty arises when using this method. Van Dixhoorn [9] concluded that the amount of smoke in the setup highly influences the quality of the images. Therefore, the second method with less amount of smoke is studied.

The second method to mark the flow by means of smoke is by generating smoke in a two-dimensional plane and using backlight illumination for the smoke particles. The smoke sheet is generated by evaporating a smoke fluid that runs along a heating wire. The advantage of this method is that the light source does not need to be regulated for generating a light sheet. In the first method, the light sheet is usually created by a laser beam [16] whereas this method can employ any kind of light source. Moreover, the laser sheet method uses smoke that is injected to the flow and fills the entire PMMA tube in a short amount of time. The quality of the photograph taken under this condition is deemed to be insufficient [9]. The amount of smoke generated from the smoke wire is relatively small compared to the laser sheet method, thus the smoke wire method was chosen.

In order to conduct the flow visualization using the smoke wire technique, the setup needs to be modified to accommodate the wire and the smoke liquid feeding. The different factor that influences the quality of the picture such as the high-speed camera, the smoke wire, the smoke liquid and the lighting position will be investigated in the next sections.

2.3.2. Test section

The smoke wire is mounted vertically inside the PMMA tube within 4 cm spacing to the jet pump sample (Figure 2.17). Two plugs have been made to hold the smoke wire at the upper part and the bottom part of the PMMA tube. These plugs are made of Teflon that can withstand temperature up to 250°C. The upper plug also serves as a liquid reservoir. A needle is connected at the bottom of this plug. This needle is needed because it was observed that without the needle, the liquid flows along the wall of the PMMA tube due to the concave curvature.

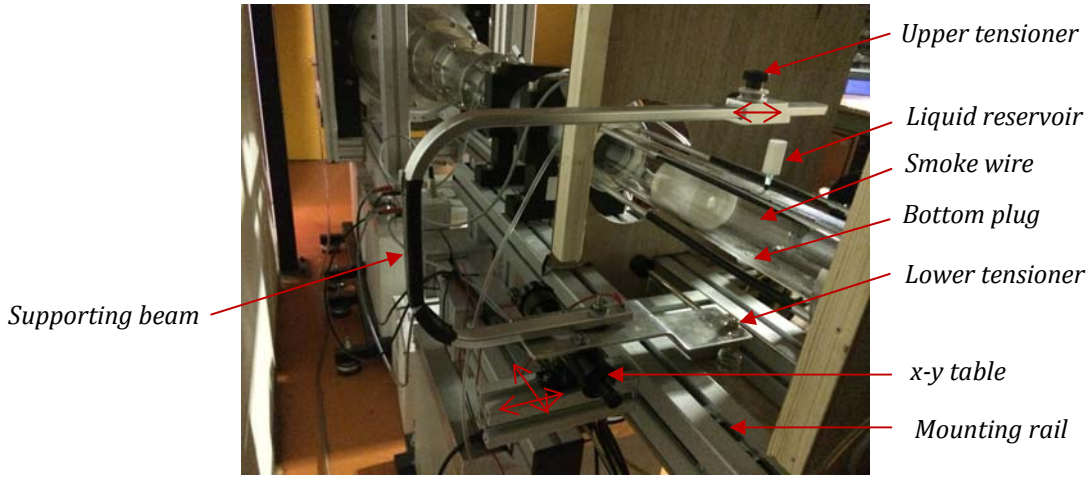

Figure 2.17 Smoke wire test section.

The smoke wire holder consists of an upper tensioner and a lower tensioner that are connected by a supporting beam. The positioning of these tensioners against the PMMA tube can be set using an x-y-table. For an angle adjustment, the upper tensioner can be moved by sliding it along the supporting beam. The two wire holders are connected to the power supply where the power can be regulated to produce the desired wire temperature.

A high-speed camera is mounted across the supporting beam. The high-speed camera is mounted to the mounting rail and can be moved in three axial directions.

2.3.3. Smoke wire

Three different smoke wires have been tested to observe the wire temperature and hence, the evaporation of the smoke liquid. The first wire is made of tin with 1 mm diameter. This wire is more rigid compared to the others, thus it needs a stronger support for the tensioner. Due to its rigidity, it heats up fastly and it can cut the PMMA tube easily compared to other wire. The PMMA tube has a Vicat softening point of 47°C [29]. The Vicat softening point indicates the temperature at which the material can be penetrated to a depth of 1 mm by a flat-ended needle with a cross-section of 1 mm^2 according to Vicat test. It has been observed that at 50°C, the PMMA tube can be penetrated by the tensioned wire. Since this wire conducts high temperature that can soften the PMMA material, it was not chosen for the smoke wire. The second wire that has been tested is made of Tungsten with a diameter of 0.005 mm. This wire is suitable for our application, however it cannot withstand high temperature. Thus, the third wire was tested. It is made of NiCr 8020 with diameter of 0.2 mm. This wire is chosen as the most suitable one because of its flexibility and its ability to withstand large range of temperature.

Another factor to note is the ability of the wire to resist the liquid flow. It is noted from the preliminary experiments that the liquid falls as a droplet from the tip of the needle. These droplets flow along the wire and only a small amount of the droplet is evaporated. Most parts of the droplet are deposited at the bottom of the PMMA tube. This phenomenon happens for all types of smoke wire and smoke liquid, even though the temperature of the wire has been set to maximum. Therefore, it is desired to extend the duration of the droplet on the wire such that larger parts of the droplet will be able to evaporate as it flows along the wire.

To solve this problem, the wire is tied by making equidistant knots of about 1 cm to each other (Figure 2.18). The equidistant knots were observed to give a better result than a straight

wire because the liquid is confined at the knots. This configuration has an advantage of generating a line of smoke at the knots even at high velocity flow (more than 10 m/s). As better results were observed from this configuration, it is used in the scope of this thesis.

Figure 2.18 Smoke wire tied in knots.

2.3.4. Smoke liquid

Different smoke liquids have been examined to obtain the highest contrast. These fluids have the boiling point on the same range, about 100-150°C. A steady flow is applied and the trailing smoke patterns are observed visually. According to the observation, it was decided to use the Safex smoke fluid because it produces the clearest smoke. Moreover, the smoke particles do not patch to the inner wall of the tube, hence no cleaning is needed as would be for other liquids. The summary of the visual observation is presented in Table 2.6.

Table 2.6 Smoke fluid selection table.

Liquid	Boiling point	Viscocity	Results
Paraffine oil	>61°C	1.9 Pa	Very nonviscous. Creates a thin layer of trailing smoke. Problem arises after some time when the smoke particles patch in the inner wall of the tube and create a layer that influences the result of the picture.
Glycerine 80%	101.6°C [19]	6.01 Pa	This liquid has the highest viscosity compared to the others, thus it stays longest in the knotted wire. The smoke particles patch to the inner wall of the tube, hence frequent cleaning is required. This thin layer of smoke particles sticks to the wall better than other liquids, thus it is difficult to clean. Needs the most frequent cleaning.
Glycerine 30%	114.0°C [19]	0.25 mPas	It is expected to have more clear smoke by dilute glycerine in water. However, this does not appear in the observation. Same problem with glycerine 80%.
Eurolite smoke fluid “C”	100°C [20]	N.A.	As viscous as the paraffine oil. Creates a thinner layer of trailing smoke compared to the paraffine oil. It does not require cleaning as often as glycerine.
Safex smoke liquid	100-280°C [21]	N.A	Produces the clearest smoke. It does not require cleaning as often as other liquid. It does not stick to the inner wall.
Faller smoke oil	N.A	N.A	As nonviscous as paraffine oil. Produces same amount of smoke as paraffine oil.

2.3.5. Illumination

The illumination of the smoke particles is achieved by using an LED lamp. Different positions of the lamp have been investigated to obtain the best contrast of the smoke and the black background. The black background is provided using a black cloth. However, there are some problems that need to be addressed to obtain a good quality of the picture. The first one is the glare caused by the circular wall of the tube. This problem is solved by placing the LED lamp at the end of the open (or closed) setup and thus provides illumination from inside the tube. However, for the traveling wave termination, this lighting position cannot be applied and hence the LED lamp should give illumination from outside of the tube. It was noted that by putting the LED lamp parallel to the tube rotational axis, the tube reflection appears in the picture. Therefore, this configuration should be avoided. Putting the lamp beside the camera also leads to a visible tube reflection. Illuminating the tube from the back gives a better result and the lamp should be placed in an angle with respect to the tube axis (Figure 2.20).

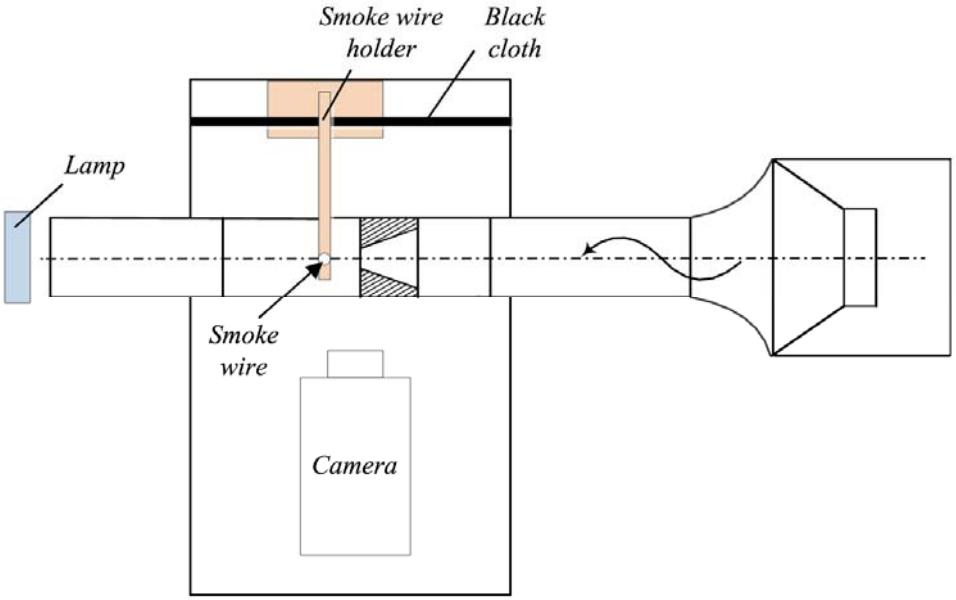

Figure 2.19 Schematic drawing of the lighting position for standing wave setup (upper view, not to scale).

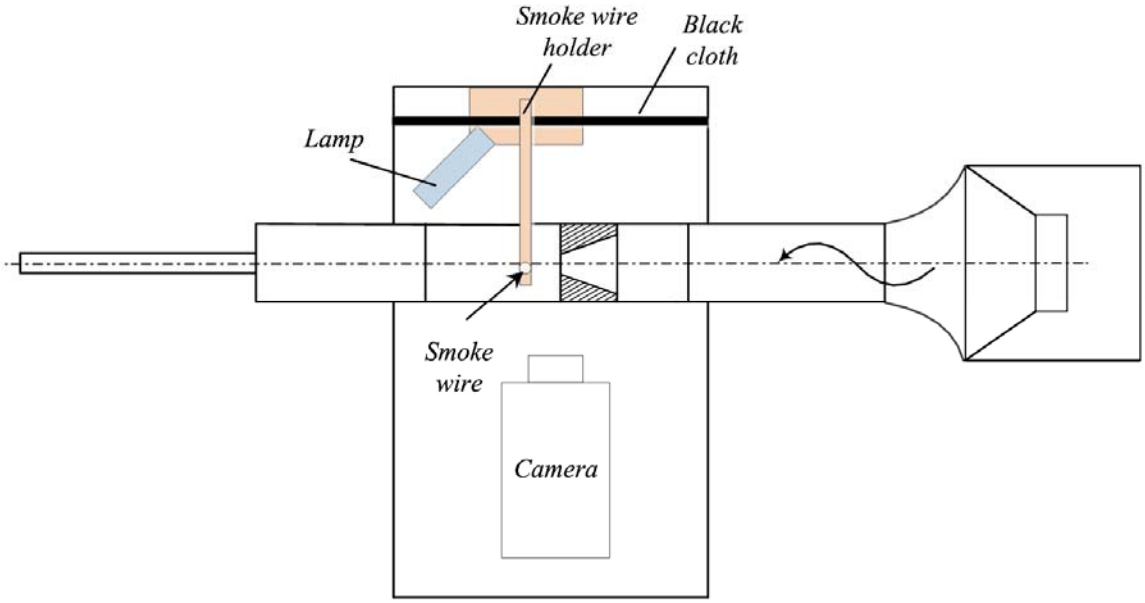

Figure 2.20 Schematic drawing of the lighting position for traveling wave setup (upper view, not to scale).

The second problem is the low contrast between the smoke and the black background. The black cloth can also reflect light and therefore all the light inside the room should be switched off except the LED lamp. The best contrast is achieved in an open and closed end setup because the black cloth is located far away from the LED lamp, consequently only little reflection comes from the background. On the other hand, the setup with traveling wave termination cannot have as black background as the open and closed setup.

The fluid selection also contributes to improve the contrast of the picture, thus the Safex smoke liquid is used for further experiments.

2.3.6. High-speed camera

A high-speed camera is used to capture the movement of the gas inside the setup. A Phantom v7.3 high-speed camera with a Nikkor 40 mm Macro lens at aperture f/3.6 is used for the flow visualization. The high-speed camera is set to capture 1000 frame per second, therefore it captures the mean flow at nine points over a period for 113 Hz. Higher frame rate is possible to use (up to 6500 fps), however it requires more light that cannot be done with conventional lighting.

2.4. Summary

A traveling wave termination has been manufactured for experiments with traveling wave. The traveling wave termination works best at 113 Hz with absorption coefficient of 99.9%. A test section for flow visualization using the smoke wire has also been realized. The selection of the heating wire, the smoke liquid, the lighting position and high-speed camera settings has been done to obtain the best picture quality.

CHAPTER 3

EXPERIMENTS AND RESULTS

Minor loss coefficient for oscillatory flow has been studied over the past decades experimentally and numerically. The experiments of Iguchi [8], Olsen and Swift [36], Petculescu and Wilen [7] are some examples of the study conducted in oscillatory flow. An example of numerical study is the one of Backhaus and Swift [2], in which a relation between the minor loss coefficient for oscillatory flow, velocity amplitude and the time-averaged pressure drop is described. From these previous works, three assumptions are used to determine the minor loss coefficient for oscillatory flow. The assumptions are explained as follows:

1. The Iguchi hypothesis assumes that the value of the minor loss coefficient for an oscillatory flow could be described by a quasi-steady approach [8]. This implies that the total minor loss coefficient for a jet pump in oscillatory flow is the summation of the minor loss coefficient for the forward steady flow and the backward steady flow.

2. The minor loss coefficient for expansion of a steady flow can be calculated using the Borda-Carnot formula (Equation (1.4)) and depends only on the cross-sectional area, while the minor loss coefficient for contraction can be obtained as a constant (see Chapter 1.2). These values have been tabulated for the steady flow case [2,16,23,31].

3. The relation between pressure drop and velocity amplitude in the jet pump is quadratic, while the power dissipation has a cubic relation. These are based on a quasi-steady model that has been developed by Backhaus and Swift [2] and are used to determine the minor loss coefficient for oscillatory flow. This model will be explained later in Chapter 3.2.

The issue addressed in the scope of this thesis is the applicability of these assumptions for jet pumps in oscillatory flow. To investigate this, four jet pump samples were made with varied geometries. Two sets of experiments with the jet pump samples have been performed and the results are presented in this chapter. The first experiment is the pressure and power measurement and the second one is the flow visualization using the smoke wire method. The first experiment was carried out to study the effects of different jet pump geometries to the pressure drop and power dissipation. The flow visualization experiment was conducted to obtain the flow patterns generated by a jet pump in oscillatory flow. The information on the flow patterns can give a better understanding to interpret the results of pressure and power measurement.

Firstly, the four jet pump samples are introduced in Chapter 3.1. The methods to measure the pressure and acoustic power are explained in Chapter 3.2. Finally, Chapter 3.3 delivers the results obtained from the two experiments and the discussion.

The first experiment was performed for all jet pump samples and uses three types of setup termination for each one: the open end, the closed end and the traveling wave termination. Chapter 3.3.1 presents the results from this experiment. The effect of the taper angle, the number of holes and the jet pump termination on the time-averaged pressure drop and acoustic power dissipation are explained. The experimental minor loss coefficients for oscillating flow, forward flow and backward flow are also determined from this experiment.

Based on this experiment, the applicability of the three assumptions is concluded. The discussion on the applicability of the three assumptions is presented in this chapter.

The flow visualization experiment was carried out for one jet pump sample only. This experiment was performed to know whether the smoke wire method is sufficient to capture the flow pattern. If so, this method can be used for future research with other jet pump samples. The obtained flow patterns will also be a reference for flow visualization of other jet pump samples. The flow visualization experiment uses the smoke wire test section described in Chapter 2.3.1.

3.1. Jet pump samples

To conduct the two experiments, four jet pump samples have been designed with varied geometries. In order to design a jet pump, the geometry has to be defined. Figure 3.1 presents the geometry of a jet pump.

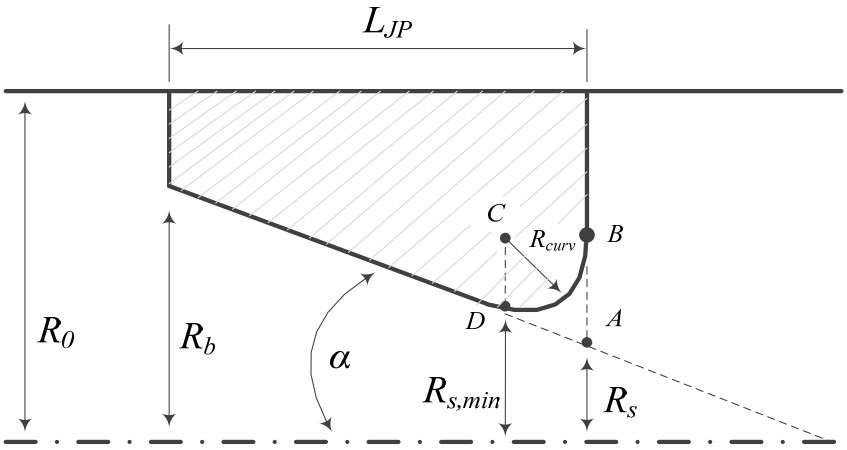

Figure 3.1 Jet pump geometry.

Based on the assumption of minor loss coefficient for a steady flow, the minor loss coefficient depends on the narrowest and widest cross-sectional area of the jet pump opening and the radius of curvature. This narrowest area is defined by the waist radius $R_{s,min}$ while the widest is defined by the radius R_b. The opening near the jet pump waist is rounded with a curvature of R_{curv}. These parameters are kept constant for all jet pump samples while varying the number of holes and the taper angle α. The taper angle and the cross-sectional area determines the length of the jet pump L_{JP}.

Four different jet pump samples are designed with varied parameters of taper angle and number of holes. The design was made based on the geometry of the first jet pump sample used by van Dixhoorn [9]. This geometry was firstly chosen based on the available numerical data of an ongoing numerical study [37]. The widest and narrowest cross-sectional area A_b and $A_{s,min}$ are kept constant for all samples, as well as the radius of curvature R_{curv}. The taper angle and the number of holes are varied because these parameters may influence the minor loss coefficient. The taper angle is designed for 7° and 15° while the jet pump length follows from the specified taper angle and the cross-sectional area. The number of holes is chosen to be one and two holes where the cross-sectional area A_b and $A_{s,min}$ are divided over the number of holes.

The ordered jet pump samples are measured to know the exact diameter in the widest and narrowest cross section, as well as its length. The measurement was done four times with a three-point micrometer. The average values and the designed values are shown in Table 3.1. It should be noted that due to a drawing mistake, one jet pump was manufactured with a shorter length than what is originally designed, hence an 18° taper angle.

Table 3.1 Designed and measured jet pump geometry.

	Jet Pump Geometry		7° 1 hole	7° 2 holes	15° 1 hole	18° 2 holes
Designed	L_{JP}	(mm)	70.11	51.16	35.35	26.67
	D_s	(mm)	12.78	8.658	11.05	6.928
	D_b	(mm)	30.00	21.21	30.00	21.21
	$A_{b,total}$	(mm^2)	706.9	706.9	706.9	706.9
	$D_{s,min}$	(mm)	14.09	9.96	14.09	9.96
	$A_{s,min}$	(mm^2)	155.8	155.8	155.8	155.8
Measured	L_{JP}	(mm)	71.0	51.6	36.1	23.7
	D_b (mm)	Hole 1	30.015	21.235	29.885	21.120
		Hole 2	-	21.279	-	21.125
	$A_{b,total}$	(mm^2)	707.565	709.773	701.449	700.827
	$D_{s,min}$ (mm)	Hole 1	13.978	9.912	12.706	9.629
		Hole 2	-	9.916	-	9.636
	$A_{s,min}$	(mm^2)	153.462	154.378	126.802	145.750
% off	$A_{b,total}$	%	0.10%	0.41%	-0.77%	-0.85%
	$A_{s,min}$	%	-1.52%	-0.94%	-18.63%	-6.47%

The jet pump samples are placed in the experimental setup with a location shown in Figure 3.2 and numerical values given in Table 3.2. The value of x_{JP} differs for each sample due to a hole in the tube wall that is located at $x = 605\ mm$. This hole was used previously to feed smoke into the jet pump for flow visualization using a laser sheet (see [9,28]). The jet pump sample is placed such that it covers this hole. Since the jet pump samples have different lengths, this results in a different positions of x_{JP}. The different jet pump positions do not significantly influence the result due to the small difference, less than 2 cm.

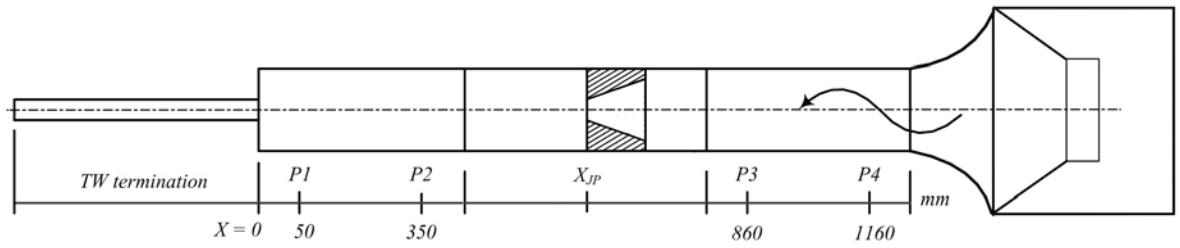

Figure 3.2 Jet pump sample and pressure sensors locations in the experimental setup.

Table 3.2 x_{JP} values for each jet pump sample.

Jet pump sample	x_{JP} (mm)
7° 1 hole	572
7° 2 holes	572
15° 1 hole	582
18° 2 holes	590

3.2. Theory

The jet pump samples are tested in an oscillatory flow to obtain the pressure drop and acoustic power dissipation. In this section, the method to obtain the pressure drop and acoustic power dissipation are explained. From the pressure drop measurement, the total minor loss coefficient of a jet pump in oscillatory flow can be obtained. The power measurement uses the so-called Fusco method [25] and the acoustic power dissipation over the jet pump can be obtained. Then, using additional information from the power measurement, the minor loss coefficient for the forward flow and backward flow can be estimated respectively. The procedures for obtaining these results are described in the following paragraphs.

3.2.1. Pressure drop measurement and total minor loss coefficient calculation

The pressure drop measurement was performed to determine the minor loss coefficient of oscillating flow, the forward flow and the backward flow of each jet pump sample. These coefficients can be determined from the correlation between the time-averaged pressure drop and the velocity amplitude in the jet pump $u_{1,JP}$.

A correlation between the time-averaged pressure drop and the velocity amplitude has been derived by Backhaus and Swift [2] using a quasi-steady model. This model assumes that the flow has no memory of its past [7]. Thus, the oscillatory flow can be described as a steady flow going to the left hand side of the jet pump and a steady flow back to the right hand side of the jet pump (see Chapter 1.2). Equation (3.1) shows this correlation.

$$\Delta p_{JP} = \frac{\rho_m \, u_{1,JP}^2}{8} K_{tot} \tag{3.1}$$

The total minor loss coefficient for oscillatory flow (K_{tot}) is defined as a function of the minor loss coefficient for forward steady flow (K_{out}) and backward steady flow (K_{in}) in the following equation.

$$K_{tot} = K_{out} - K_{in} = \left(K_{exp,s} - K_{cont,s}\right) + \left(\frac{A_{s,min}}{A_b}\right)^2 \left(K_{cont,b} - K_{exp,b}\right) \tag{3.2}$$

From Equation (3.1), the relation between pressure drop and velocity amplitude in the jet pump is quadratic. The pressure drop and velocity amplitude have to be obtained from experiments in order to calculate the total minor loss coefficient. The pressure measurements make use of four pressure sensors mounted in the setup with locations as depicted in Figure 3.2. These pressure sensors measure the time-averaged pressure at each location as well as the

pressure amplitude. The time-averaged pressure data are used for the pressure drop measurement. The time-averaged pressure measurement on the right hand side of the jet pump is measured by sensor P3 whereas the left hand side is measured by sensor P2. Thus, the time-averaged pressure drop across the jet pump can be calculated.

The pressure amplitudes are needed in order to estimate the velocity amplitude in the jet pump waist. This value cannot be directly measured by the data acquisition system. One way to obtain the velocity amplitude at the jet pump waist is by using an acoustic model and to relate it with parameters that are known from the experiment, such as pressure amplitude at sensor P4. An acoustic model of the experimental setup is available from previous research and will be explained in the following paragraphs.

The model was made in COMSOL Multiphysics 4.4 for the experimental setup with three kinds of termination. The jet pump sample is also modeled and is placed with a position according to Table 3.3. Only the single hole jet pumps are modeled; the double hole jet pumps have more complex geometry and it cannot be modeled using an axial symmetry model. It has to be modeled in fully three-dimensional domain, therefore it needs a longer computational time.

The COMSOL model is made on the physics interface. This model is applicable to geometries with small dimensions. The viscous and thermal conduction effects are incorporated in the governing equations. The governing equations are the full linearized Navier-Stokes (momentum), continuity and energy equations. Assuming that all fields and sources to be harmonic, the governing equations are solved in the frequency domain. Solving these equations, the propagation of compressible linear waves in a general viscous and thermally conduction fluid is modeled. The solution consists of the acoustic pressure, the velocity vector and the acoustic temperature variations.

A linear correlation between the velocity amplitude at the jet pump waist and pressure amplitude at sensor P4 is obtained. The results are presented in Table 3.3 for three terminations. These constants can be used to approximate the velocity amplitude at the jet pump waist $u_{1,JP}$ using the measured pressure amplitude at sensor P4.

Table 3.3 Effectiveness constants for determining the velocity amplitude (m/(Pa.s)).

Termination	7°	15°
Closed	0.0308	0.0372
Open	0.0148	0.0141
Traveling wave	0.0262	0.0311

The effectiveness constants are applicable to the case of double hole jet pumps as well and will be explained as follows. The acoustic field inside the setup is generated by the oscillation of the loudspeaker membrane. Since the same acoustic field is generated by the loudspeaker for all jet pump samples, it can be assumed that the volume flow rate is constant. The volume flow rate is related to the velocity flowing through a cross-sectional area. The cross-sectional area at the waist of the jet pump samples is kept constant and the volume flow rate is assumed to be the same. As a consequence, the velocity amplitude is the same for a single hole and double hole jet pump.

The actual minor loss coefficient K_{tot} from the experiment is determined by fitting a quadratic curve to the pressure drop and velocity amplitude measurement according to Equation (3.1). From the curve fitting, the slope of the curve is known and thus K_{tot} can be calculated.

3.2.2. Acoustic power dissipation measurement

The acoustic power dissipation over the jet pump is measured in order to obtain the minor loss coefficient for forward flow and backward flow. The acoustic power dissipation over the jet pump is obtained by measuring the acoustic power at the right hand side (of Figure 3.2) and left hand side section of the jet pump. The power measurement uses the so-called Fusco method [25] for which two pressure sensors are needed to obtain the acoustic power at one section.

The acoustic power is defined as the acoustic energy flowing in the axial direction, time-averaged over an integral number of cycles of the wave [38]. Using this definition, the acoustic power can be formulated as follows:

$$\dot{E} = \frac{\omega}{2\pi}\oint p(t)U(t)dt = \frac{1}{2}\boldsymbol{Re}[p_1\widetilde{U}_1] \tag{3.3}$$

where p is pressure, U is the volume flow rate and $\widetilde{U}$ is the complex conjugate of the volume flow rate. Since the volume flow rate can be defined by the velocity and the cross-sectional area, Equation (3.3) is obtained with θ as a phase difference between p and u.

$$\dot{E} = \frac{1}{2}|p||U|\cos\theta = \frac{1}{2}|p||u|A\cos\theta \tag{3.4}$$

The acoustic power is measured at the right section and at the left section of the jet pump, thus the power dissipation can be obtained. The power measurement is done based on the method described by Fusco [25]. This method uses two pressure sensors to measure the power at each tube section. It measures the pressure gradient over a distance between the two pressure sensors. The average pressure p_{avg} is calculated from the two pressure sensors.

$$p_{avg} = \frac{\widetilde{p_{a,1}} + \widetilde{p_{a,2}}e^{-i\phi}}{2} \tag{3.5}$$

where ϕ is the phase difference between the two pressure sensors. Another parameter is obtained from the two pressure sensors, namely the complex pressure difference.

$$\Delta p_{avg} = \widetilde{p_{a,1}} - \widetilde{p_{a,2}}e^{-i\,\phi} \tag{3.6}$$

The average pressure and average pressure difference are necessary to calculate the acoustic power. The acoustic power can be calculated based on the Newton's Second Law of motion. Consider a gas parcel with mass m inside a cylinder with a cross-sectional area of A. The forces applied to the gas parcel causes it to move with acceleration of a. Thus, the acceleration of the gas parcel can be formulated as in Equation (3.7).

$$\begin{aligned} \Sigma F &= m\,a \\ (p_2 - p_1)A &= ma \\ (p_2 - p_1)A &= \rho\, A\, \Delta x\, a \\ a &= \frac{du}{dt} = \frac{-\Delta p}{\rho \Delta x} \end{aligned} \tag{3.7}$$

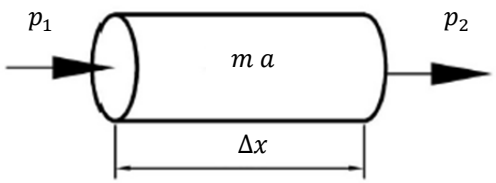

The velocity of the gas parcel can be determined by integration over time:

$$u = \frac{-\Delta p}{i\omega\rho\Delta x} \tag{3.8}$$

Substituting Equation (3.6) to (3.8) and (3.4), the acoustic power can be obtained as follows:

$$\dot{E} = \frac{A}{2\omega\rho\Delta x}\left|p_{a,1}\right|\left|p_{a,2}\right|\sin\phi \tag{3.9}$$

The phase difference θ between p and u can be obtained from Equation (3.10):

$$\theta = \arctan\frac{\widetilde{p_{a,2}}\sin\phi}{\widetilde{p_{a,1}} - \widetilde{p_{a,2}}\cos\phi} \tag{3.10}$$

The aforementioned formula has a limitation on the location of the pressure sensors. The spacing between pressure sensors should be closer than 0.03λ to ensure that the effect of attenuation can be negligible [25]. Fusco proposes another equation valid for any distance Δx for calculating the acoustic power [25]:

$$\dot{E} = \frac{A}{2\rho a\sin\frac{\omega\Delta x}{c_0}}\left(\left|p_{a,1}\right|\left|p_{a,2}\right|\sin\phi\left\{1 - \frac{\delta_\nu}{2r_0}\left[1 - \frac{\gamma-1}{\sqrt{\sigma}} + \left(1 + \frac{\gamma-1}{\sqrt{\sigma}}\right)\frac{\omega\Delta x}{c_0}\cot\frac{\omega\Delta x}{c_0}\right]\right\}\right.$$

$$\left. + \frac{\delta_\nu}{4r_0}\left(\left|p_{a,1}\right|^2 - \left|p_{a,2}\right|^2\right)\left[1 - \frac{\gamma-1}{\sqrt{\sigma}} + \left(1 + \frac{\gamma-1}{\sqrt{\sigma}}\right)\frac{\omega\Delta x}{c_0}\csc\frac{\omega\Delta x}{c_0}\right]\right) \tag{3.11}$$

This equation is most suitable for traveling wave case because the phase difference ϕ between the two adjacent sensors is large enough. Difficulties may arise if this method is used for cases with high standing wave ratio, hence a small $\sin\phi$ value. The accuracy of this method becomes lower [30]. This can be minimized by separating the sensors as far as possible and avoid the placement of both sensors near a pressure node or antinode at the same time. This way, a higher pressure gradient and consequently a higher accuracy can be achieved.

The acoustic power is measured using Equation (3.11) for the right and left hand side sections of the jet pump respectively. Two pressure sensors were used to obtain the acoustic power at each section and the spacing between each pressure sensor is mentioned in Figure 3.2. From the measured acoustic power at each section, the acoustic power dissipation across the jet pump can be calculated.

3.2.3. Estimation of experimental K_{in} and K_{out}

In order to check the validity of the assumption on the minor loss coefficients for steady flow, the total minor loss coefficient for oscillatory flow (K_{tot}) needs to be obtained. The total minor loss coefficient for oscillatory flow (K_{tot}) is obtained from the experimental results on pressure drop measurement. The quasi-steady model of Backhaus and Swift [2] is used to obtain this value.

Since K_{tot} depends on the minor loss coefficient for a forward and a backward flow (K_{out} and K_{in} respectively), these two values are estimated as well. The experimental K_{in} and K_{out} can be obtained by using an equation for the time-averaged power dissipation.

The time-averaged power dissipation can be obtained based on the quasi-steady model of Backhaus and Swift [2]. They have derived an expression to relate the time-averaged power dissipation and the maximum velocity in the jet pump. From their quasi-steady model, the acoustic power dissipation is proportional to $u_{1,JP}^3$, and is expressed in Equation (3.12).

$$\dot{E} = \frac{\rho_m A_s u_{1,JP}^3}{3\pi} K_E \tag{3.12}$$

The other equation that is needed to estimate the experimental K_{in} and K_{out} is the quasi-steady formulation for time-averaged pressure drop across the jet pump as mentioned in Equation (3.1). According to Equation (3.12), K_E can be obtained from the experimental data of power dissipation and the velocity amplitude. The total minor loss coefficient K_{tot} is known from the slope of the curve according to Equation (3.1). Thus, one ends with two equations and two unknown variables as follows:

$$K_E = \left[\left(K_{exp,s} + K_{cont,s}\right) + \left(\frac{A_s}{A_b}\right)^2 \left(K_{cont,b} + K_{exp,b}\right)\right] = K_{out} + K_{in} \tag{3.13}$$

$$K_{tot} = \left[\left(K_{exp,s} - K_{cont,s}\right) + \left(\frac{A_{s,min}}{A_b}\right)^2 \left(K_{cont,b} - K_{exp,b}\right)\right] = K_{out} - K_{in} \tag{3.14}$$

Using Equation (3.13) and (3.14), the experimental K_{in} and K_{out} can be determined.

3.3. Results

In this section, the results from the pressure and power measurement are presented, as well as the flow visualization results. The pressure and power measurement was performed to obtain the minor loss coefficient for oscillatory flow, forward flow and backward flow and consequently, to check the validity of the three assumptions. The discussion about the validity of the three assumptions is presented in Chapter 3.3.1.

Chapter 3.3.2 presents the results of flow visualization on the single hole 7° jet pump. The flow visualization was performed for one jet pump only to determine whether or not the smoke wire method can be used to capture the flow patterns. The obtained flow patterns will also be a reference for flow visualization of other jet pump samples. The information on the flow patterns can give a better understanding to interpret the results of pressure and power measurement. The description of the flow patterns and the calculation of the vortex propagation speed are also explained in this section.

The experimental results shown in Chapter 3.3.1.1 and 3.3.1.2 are presented only for the case with the traveling wave termination. The traveling wave field represents the real environment in a thermoacoustic device such as the thermoacoustic-Stirling heat engine [2]. Therefore, the experiments with the traveling wave termination are the main interest of this thesis. Nevertheless, the experiments with closed and open end were also performed to represent a jet pump in a standing wave thermoacoustic device. The results of experiments with open end and closed end show the same behavior as that of the traveling wave termination and will not be presented here. All experimental results are provided in Appendix B.

3.3.1. Pressure and power measurement

The pressure and power measurement was conducted for all jet pump samples. The effect of the taper angle, the number of holes and the jet pump termination on the time-averaged pressure drop and acoustic power dissipation are explained. The experimental minor loss coefficients for oscillating flow, forward flow and backward flow are determined from this experiment. The discussion on the applicability of the three assumptions is also presented in this chapter.

3.3.1.1. Effect of taper angle

The effect of the taper angle on the pressure drop is presented in Figure 3.3 for the case of a single hole jet pump with quadratic fit for the 7° jet pumps. Figure 3.3 shows the pressure drop as a function of velocity amplitude with vertical error bar for each data point. The vertical error bar is obtained from the measurement over two minutes for one velocity amplitude. Only the results of experiments with the traveling wave termination are shown here. For the results of other terminations, readers are referred to Appendix B. The double hole jet pumps are not shown in this figure because they generate the same trends.

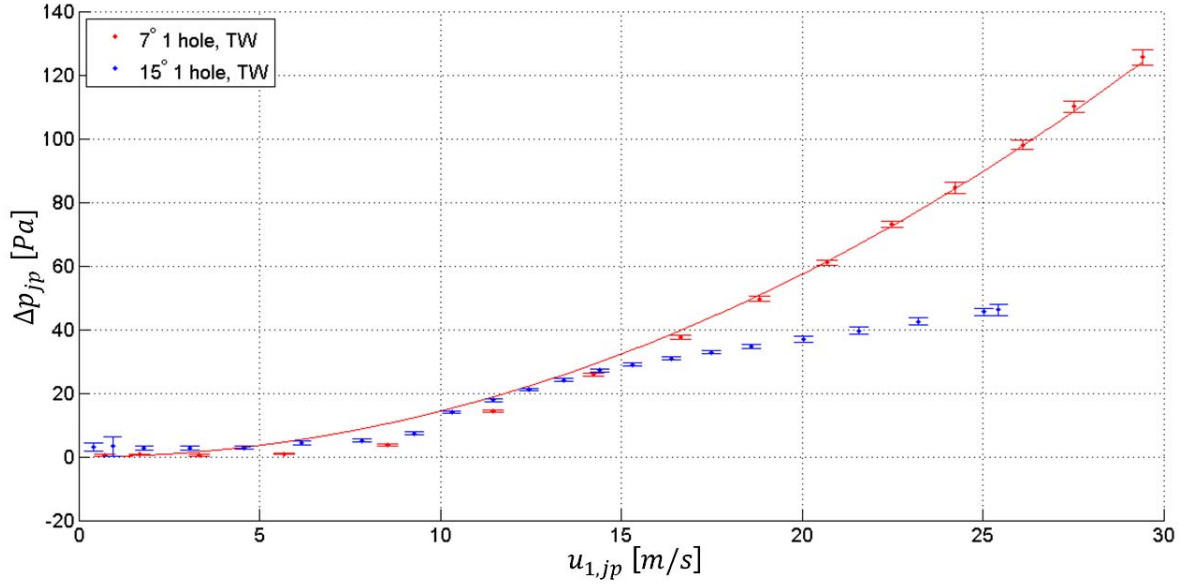

Figure 3.3 Effect of taper angle on pressure drop.

Two samples are compared: the 7° and 15° taper angle for single hole jet pump. From Figure 3.3, it is shown that higher taper angle result in a lower pressure drop. A quadratic curve fitting was done to the results of 7° jet pump according to Backhaus and Swift model (Equation (3.1)). It can be seen that the curve fitting match the results at high pressure amplitude. However, for the 15° jet pump, the experimental result reveals that this sample does not behave quadratically.

The 15° and 18° jet pump result in a nonquadratic curve for both single hole and double hole as depicted in Figure 3.4. Hence, the Backhaus and Swift model on the pressure drop does not hold for the case of high taper angle jet pumps. On the other side, the model of Backhaus and Swift matches perfectly with the experimental results of power dissipation (Figure 3.5). The

higher taper angle leads to higher power dissipation for both single and double hole jet pumps. Thus, the assumption on Backhaus and Swift model for energy dissipation holds for all cases.

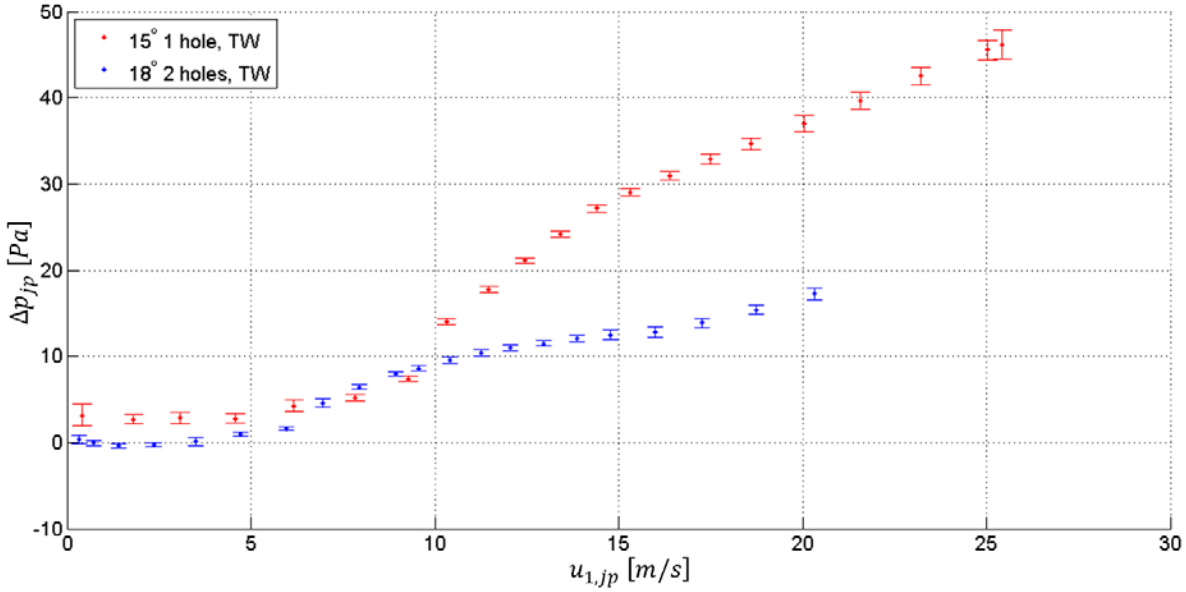

Figure 3.4 Pressure drop curve for 15° and 18° jet pump.

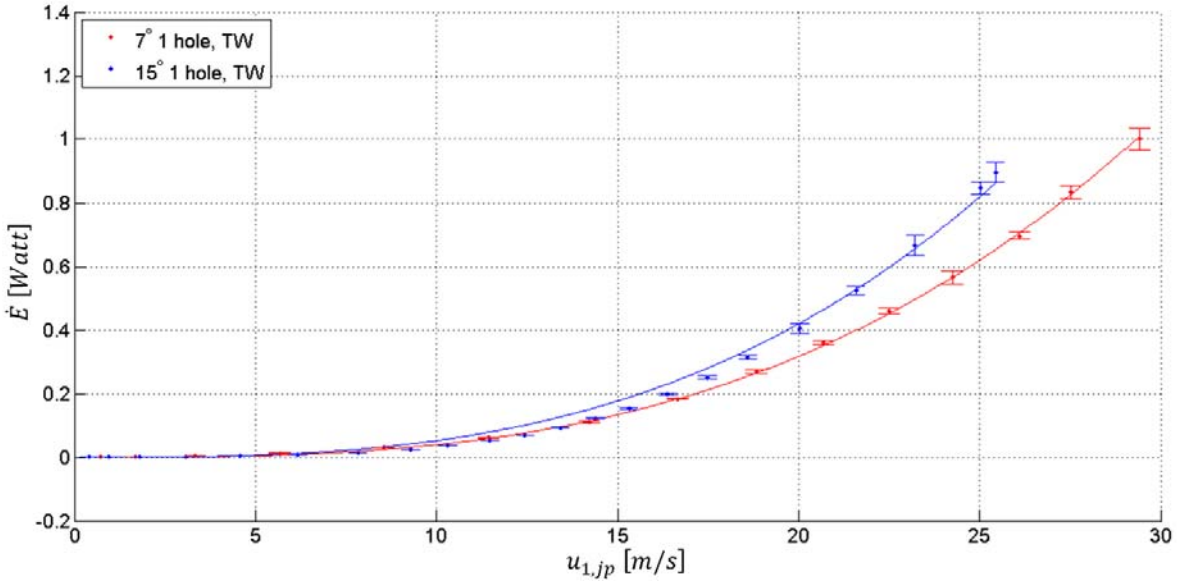

Figure 3.5 Effect of taper angle on power dissipation.

From the quadratic fit of the pressure drop curve, the minor loss coefficient can be determined. The discussion on the estimated minor loss coefficient will be presented later in Chapter 3.3.1.4.

The nonquadratic pressure drop of high taper angle jet pumps is associated to the flow separation. The flow separation is not incorporated in the Backhaus and Swift model and is explained as follows. Consider a pipe with a nontapered surface in a steady flow. Miller [22] has studied the effect of such geometry by using orifice with different thicknesses. The contraction through the orifice opening results in a jetting flow through the opening that is known as the "vena contracta". A region of separated flow is formed between the vena contracta and the wall

of the pipe (see Figure 3.6). The pressure drop and the energy dissipation over the orifice depend on the cross-sectional area of the vena contracta A_c [23]. The area of the vena contracta depends on the curvature of the junction, i.e. the rounded edge gives larger A_c, hence smaller pressure drop.

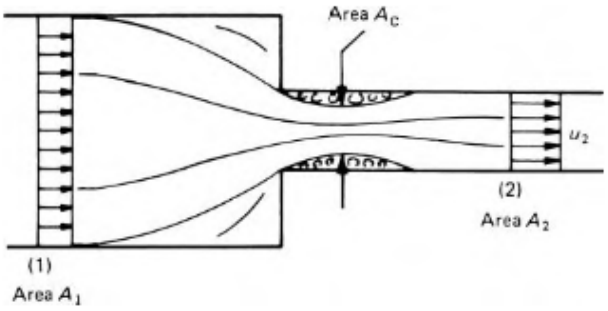

Figure 3.6 Formation of a vena contracta in a contraction [23].

The flow separation can also occur in the case of expansion, such as in a diffuser. Idel'chik [31] has studied the minor loss coefficient for steady flow in a diffuser extensively. A nonuniform velocity distribution is generally formed in the stretch before a sudden expansion. This has a strong effect on the actual pressure losses and considerably increases them above the values calculated from the Borda-Carnot formula [31].

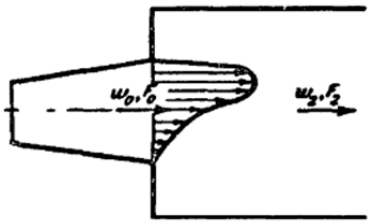

Figure 3.7 Velocity profile in a diffuser [31].

A more severe flow separation can occur in a diffuser with taper angle higher than 10° [31]. As depicted in Figure 3.8, there is a region where the flow turns to reverse direction, thus creating a zone with recirculation. This phenomenon may occur for the 15° and 18° jet pumps.

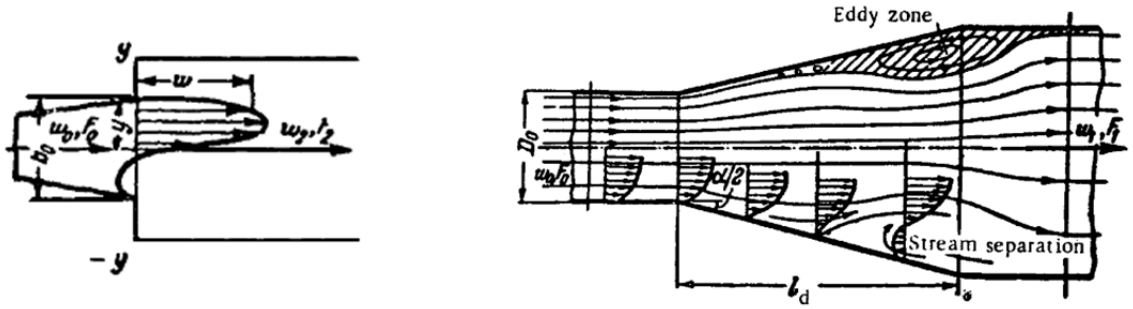

(a) Velocity profile (b) Formation of eddies

Figure 3.8 Expansion in a diffuser with $\alpha > 10°$ [31].

The curves in Figure 3.4 show exactly the flow separation phenomenon for high taper angle jet pump. There is a velocity region where the pressure drop does not give quadratic trend and this region is expected to be the region where the flow is separated. The flow separation yields the formation of the vena contracta that causes pressure drop and energy dissipation [23]. For a steady flow, the highest pressure drop and energy dissipation are obtained from the smallest cross-sectional area of the vena contracta A_c. As shown in the case of steady flow in a diffuser, the high taper angle ($\alpha > 10°$) causes a smaller A_c, thus more severe pressure drop and power dissipation. For the case of oscillatory flow, this phenomenon can be explained by looking at the minor loss coefficients K_{out} and K_{in} from the Backhaus and Swift quasi-steady model. According to Backhaus and Swift model, the pressure drop depends on $(K_{out} - K_{in})$, unlike the power dissipation that depends on $(K_{out} + K_{in})$. It should be noted that for the case of a steady flow, higher taper angle causes higher K_{out} and K_{in}. Hence, for the case of oscillating flow, the subtraction of K_{out} and K_{in} can lead to three possibilities (Figure 3.9).

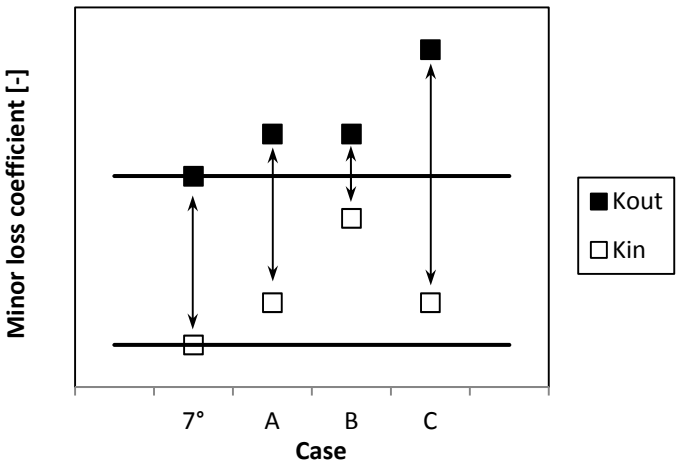

Figure 3.9 Illustration of three possible cases of the 15° and 18° jet pump.

Consider the case of 7° jet pump as a reference. Case A, B and C have higher K_{out} as well as higher K_{in} compared to the case of 7° jet pump. However, Case A results in the same $(K_{out} - K_{in})$ as the 7° case. Case B gives a lower $(K_{out} - K_{in})$, while case D shows higher $(K_{out} - K_{in})$. From the experimental results on pressure drop, it is suggested that case B occurs and the backward flow have a higher effect for the high taper angle jet pumps. To confirm this hypothesis, the values of K_{out} and K_{in} from the experimental results are estimated and will be presented later in Chapter 3.3.1.4.

The hypothesis that Case B occurs during the experiment is reasonable if one takes into account the formation of the vena contracta. Consider the case of a forward flow in Figure 3.10. Due to the contraction on the cross-sectional area of the jet pump, no vena contracta is formed in the jet pump. The contact between the flow and the tapered surface occurs during the half cycle when the gas moves forward. On the other hand, due to the expansion of the cross-sectional area of the jet pump, a vena contracta is formed during the backward flow. At the jet pump waist, the flow encounters abrupt contraction and this leads to higher minor loss coefficient for the backward flow, hence lower total minor loss coefficient for the oscillatory flow.

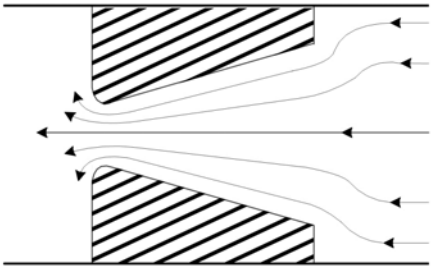

(a) Forward flow: no formation of vena contracta.

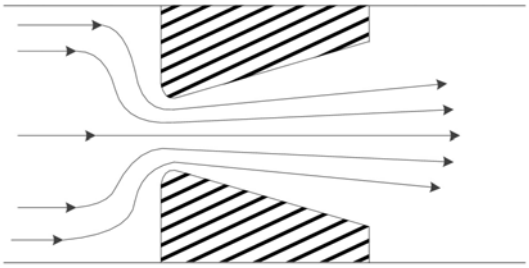

(a) Backward flow: due to the contraction at jet pump waist, vena contracta is formed.

Figure 3.10 Illustration of vena contracta formation in a jet pump.

The energy dissipation behavior can also be explained by looking at Figure 3.9. Case B results in a higher $(K_{out} + K_{in})$ and consequently, higher power dissipation. This is in accordance with the experimental results, i.e. higher taper angle jet pumps result in higher power dissipation.

From the results of pressure drop and power dissipation measurement, it is highly possible that case B occurs. The minor loss coefficient for backward flow is higher than what is predicted by the assumption on steady flow minor loss coefficient. This hypothesis will be confirmed later by estimating the value of K_{out} and K_{in} from the experiment. The calculation of the experimental K_{out} and K_{in} and the discussion will be presented in Chapter 3.3.1.4.

3.3.1.2. Effect of number of holes

According to the assumption on the minor loss coefficient for steady flow, the minor loss coefficient for expansion only depends on the widest and narrowest cross-sectional area of the jet pump, while the minor loss coefficient for contraction depends on the edge of the jet pump hole, i.e. sharp or rounded edge. Based on this assumption, the single hole and double hole jet pump should have the same pressure drop. However, the experimental results show discrepancy between the two jet pump samples. Figure 3.11 and Figure 3.12 present the effect of the number of holes. Both the pressure drop and power dissipation increases with increasing number of holes. These results suggest that the assumption on minor loss coefficient for steady flow cannot be used for oscillatory flow.

The assumption on minor loss coefficient for steady flow can be calculated using the Borda-Carnot formula for expansion. For the contraction, the values are tabulated based on the ratio of rounded radius and the hole diameter. Hence, it is desired to know whether Borda-

Carnot formula, the tabulated values, or both that are not applicable to the case of oscillatory flow.

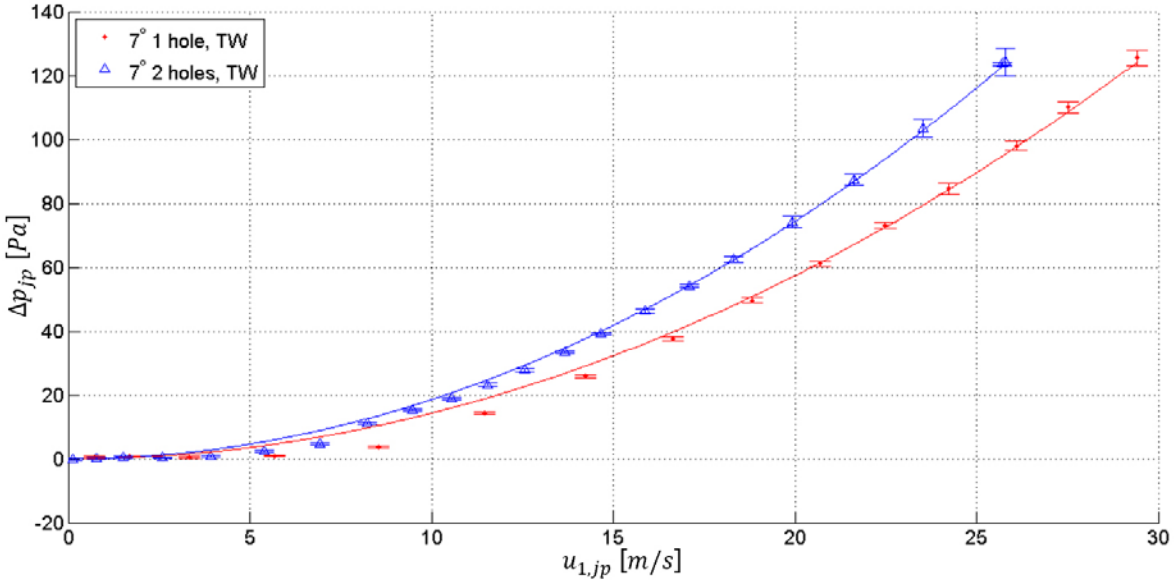

Figure 3.11 Effect of number of holes on pressure drop.
The double hole 7° jet pump gives a higher pressure drop. The curve fit based on Equation (3.1) matches the experimental data at high pressure amplitude.

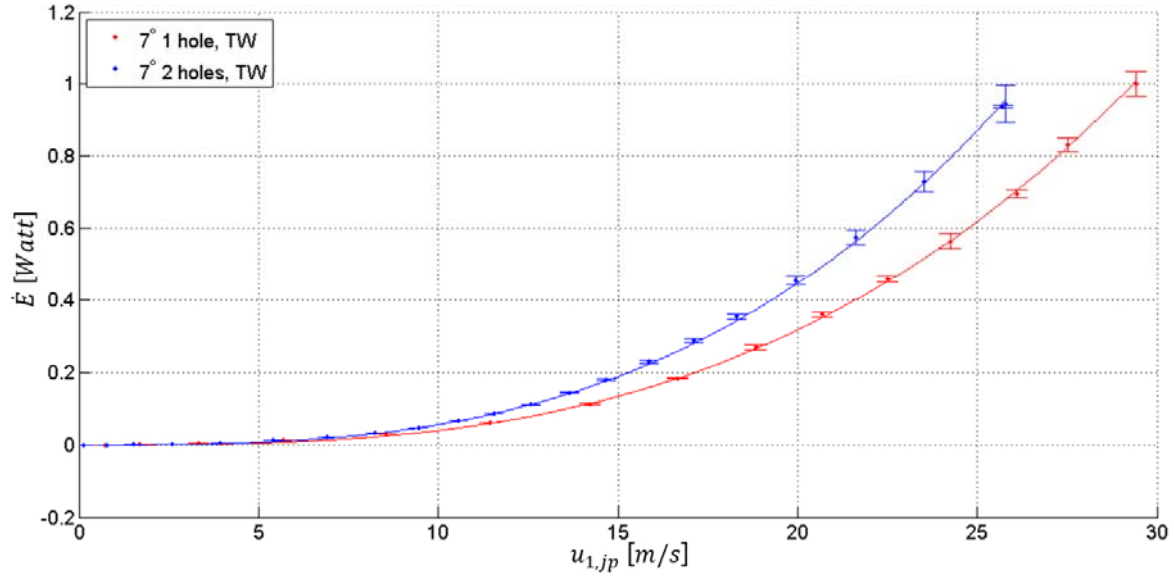

Figure 3.12 Effect of number of holes on power dissipation.
The double hole 7° jet pump gives a higher pressure drop. The curve fit based on Equation (3.12) matches the experimental data.

Three cases are evaluated: (a) the minor loss coefficient for expansion from the Borda-Carnot formula is not applicable to the oscillatory flow, (b) the minor loss coefficient for contraction from literature is not applicable to the oscillatory flow, and (c) both minor loss coefficient for contraction and expansion cannot be used for oscillatory flow. Two parameters could affect these cases, namely the inner wall and the ratio of the rounded radius and the hole

diameter. The inner wall could affect case (a), while the ratio of the rounded radius and the hole diameter could give effect to case (b).

Consider the first case. It follows from the Borda-Carnot formula that the inner wall surface area of the jet pump is not considered and therefore the pressure drop is independent to the inner wall. According to the discrepancy of the experimental results, this might not be the case. Therefore, the inner wall surface area is calculated based on the measured jet pump geometry.

The inner surface area of a jet pump is defined as the area of the tapered surface and the curved surface that connects the taper and $R_{s,min}$. The derivation of the formula for calculating the inner surface area is given in Appendix C. From the measured dimension, the inner surface area of each jet pump sample is compared to the theoretical value from the designed geometry. Table 3.4 gives the calculated inner wall surface area for the jet pump samples and the designed value.

Table 3.4 Comparison of actual and designed inner wall surface area.

Jet pump sample	**MEASURED** Cone surface area [mm2]	Curvature surface area [mm2]	Total inner surface area [mm2]	**DESIGNED** Total inner surface area [mm2]	**DEVIATION [%]**
7° 1 hole	3548	1.8	3548	3506	+1.2%
7° 2 holes	3646	10.2	3646	3611	+1.0%
15° 1 hole	1491	3.4	1491	1460	+2.1%
18° 2 holes	1413	7.1	1414	1572	-10.1%

The 18° jet pump gives the largest deviation due to the length of the jet pump which is 11.1% shorter than what is designed. From Table 3.4, the highest measured inner wall surface area is achieved for the double hole 7° jet pump, then the single hole 7° jet pump, 15° and 18° jet pump consecutively. This order is in accordance with the measured pressure drop (see Appendix B for comparison of all samples). Thus, the contour of the inner wall affects the pressure drop of a jet pump in an oscillatory flow. This has two implications: either (a) the Borda-Carnot formula cannot be applied directly to the case of oscillating flow, or (b) the Iguchi hypothesis does not hold anymore. From this experiment, it is evident that the Borda-Carnot formula does not hold for oscillating flow. One way to check this hypothesis is by performing the pressure drop measurement in a steady flow for all jet pump samples, thus eliminates or rather supports the Iguchi hypothesis.

Consider case (b). The value of $K_{cont,s}$ is dependent on a limit where for $R_{curv}/(2\,R_{s,min}) \geq 0.15$, this value is minimal, typically 0.04 [2]. In contrast, the value of $K_{cont,s}$ for a sharp edge is typically 0.5 [2]. It should be noted that this ratio limit applies for the $K_{cont,s}$ value, particularly in the case of a backward flow. In our case, the single hole and double hole jet pumps have different $R_{s,min}$ for each hole, hence different ratio. The value of $R_{curv}/(2\,R_{s,min})$ for single hole and double hole 7° jet pump are 0.4 and 0.5, subsequently. As explained in the previous section, the more rounded edge results in a larger cross-sectional area of the vena contracta, hence a lower pressure drop. Therefore, theoretically, the double hole jet pump should have a lower minor loss coefficient for the backward flow (K_{in}) and consequently, higher total minor loss coefficient for oscillatory flow K_{tot} if one assumes that the minor loss coefficient for forward flow K_{out} is kept constant. This argument is in accordance with the pressure drop results, i.e. the double hole jet pump has more rounded edge, thus higher pressure drop.

Regardless of the analysis of case (a) and (b), it is evident that the assumption on minor loss coefficient for steady flow cannot be applied to this experiment.

The higher power dissipation for the double hole jet pump is investigated. Energy dissipation could be caused by turbulence effects [32]. Therefore, the critical Reynolds number of the flow is calculated, and consequently, the velocity amplitude at which the flow starts to become turbulent is determined. The transition between laminar and turbulent in oscillating flow depends on the dimensionless frequency [39]. The dimensionless frequency is defined in Equation (3.15).

$$\omega' = R^2 \frac{\omega}{\nu} \tag{3.15}$$

where ν is kinematic viscosity and R is the tube radius, in this case $R_{s,min}$. In our case where $\omega' > 7$, the critical Reynolds number is:

$$Re_{os,c} = 882\sqrt{\omega'} \tag{3.16}$$

The Reynolds number of an oscillating flow can be calculated in the same way with steady flow, thus it depends on the velocity amplitude. The velocity amplitude at which the transition between laminar and turbulent flow occur is found to be higher than 45 m/s for all jet pump samples. Since all experiments are conducted at velocity amplitude lower than 40 m/s, the flow is laminar. However, the laminar flow can still conduct higher energy dissipation due to the effect of the coupling of two jet streams.

The coupling of two parallel jet streams in a steady airflow has been studied by Nasr and Lai [32]. They show that a recirculating zone exists in between the two jets and the velocity profile is presented in Figure 3.13.

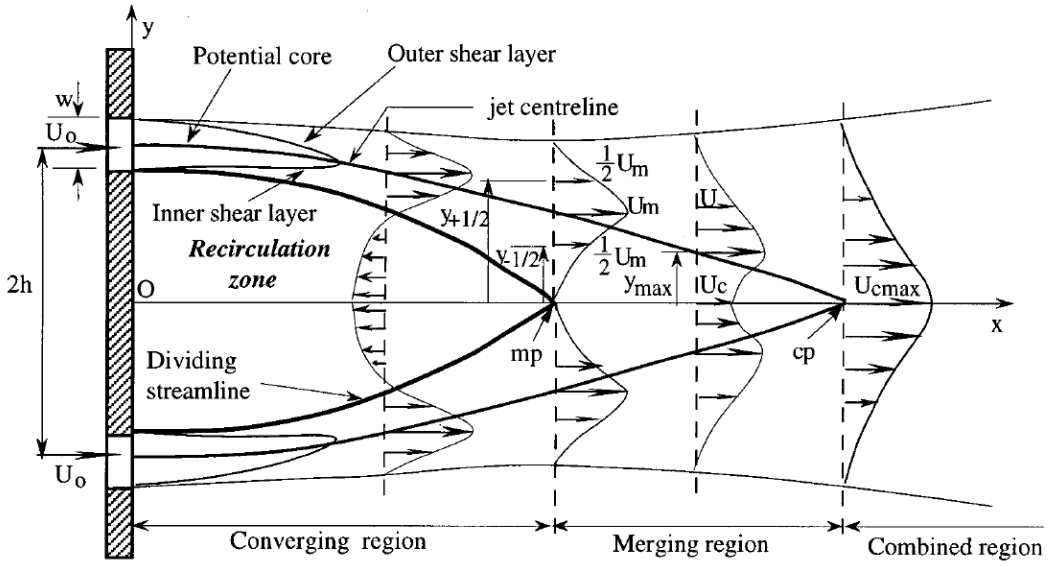

Figure 3.13 Schematic diagram of two parallel jet streams [32].

Three regions are distinguished in Figure 3.13. The converging region is located nearest to the nozzle plate. In this region, the individual jets curve towards each other due to the lower pressure close to the nozzle plate. At some distance, the two jets merge and the starting point of the merging region is indicated by the merging point *mp*. At this point, the velocity on the x axis

is zero. The two jets continue to merge in this region until they are combined as a single jet flow. The starting point of the combined region is indicated by the combined point *cp* where the velocity on the *x* axis reaches its maximum value.

The recirculation zone could lead to higher energy dissipation due to the turbulence activities [32]. Nasr and Lai compare the effect of two parallel jets and single jets. It was found that the turbulence activities in the recirculation zone and the interaction of recirculating flow with the inner shear layer are significantly stronger for the two parallel jets than for the single jet. This may lead to complex flow structures as suggested by Huang and Tsai [33]. In their experiments of visualization of a swirling double concentric jet flow, the flow field in the recirculating zone is characterized by complex flow structures such as dual rings, vortex breakdown, and vortex shedding [33]. Thus, it is necessary to perform the flow visualization for the double hole jet pumps to know whether complex flow patterns are formed and whether this case causes higher energy dissipation. However, this case is not covered in this thesis and is left for future research.

In conclusion, the assumption on minor loss coefficient for steady flow cannot be applied for an oscillatory flow. This hypothesis will be confirmed later by calculating the experimental minor loss coefficient (Chapter 3.3.1.4). However, this analysis is only valid if Iguchi hypothesis holds. This argument remains as a hypothesis since the steady flow measurement was not performed in this thesis. Thus, it is necessary to perform the steady flow measurement to clarify the assumptions that are used for this experiment.

The experimental results on the effect of taper angle and number of holes leads to a hypothesis that the taper angle effects are more dominant than the effects of number of holes. This behavior is clearly observed when the acoustic power dissipation is plotted against the pressure drop (Figure 3.14).

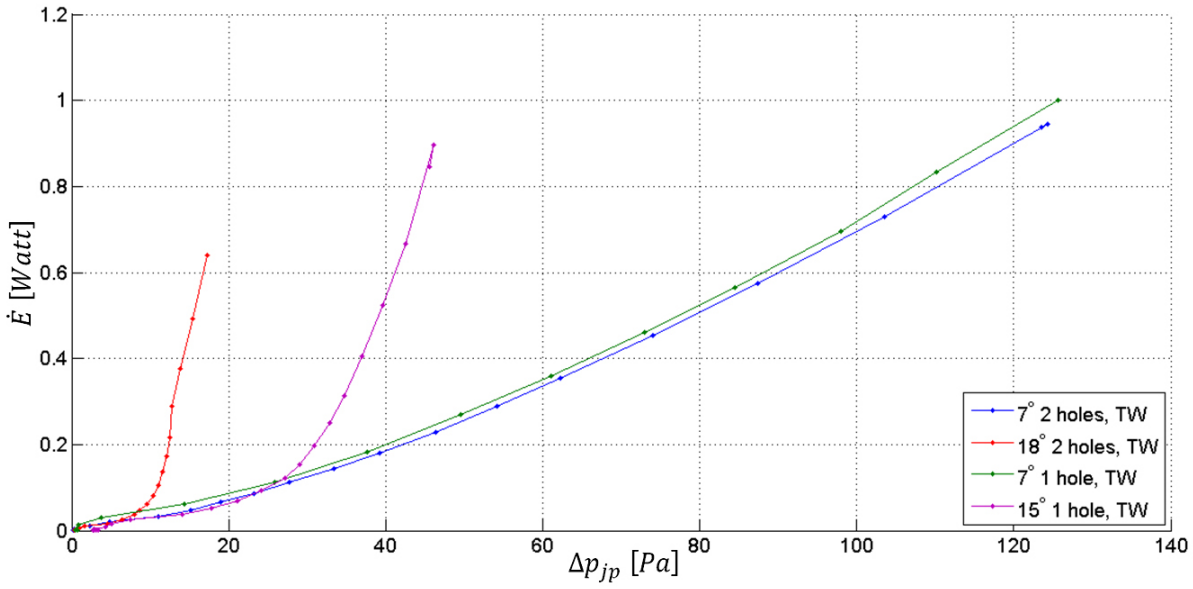

Figure 3.14 Power dissipation plotted against pressure drop.

Figure 3.14 shows that there is a similar trend for the 15° and 18° jet pump, while both the single hole and double hole 7° jet pumps have the same behavior. The double hole 18° jet pump behaves more similarly to the single hole 15° jet pump, indicating that the effect taper angle is more dominant than the effect of the number of holes.

3.3.1.3. Effect of wave phasing

The effect of wave phasing can be seen by performing the experiment using three different terminations. The traveling wave termination creates a traveling wave field inside the setup, thus the phase difference between the pressure and velocity is close to zero. Both open end and closed end creates a standing wave in the main tube, in which the phase difference between the pressure and velocity is close to 90°. The difference between open end and closed end lies on the reflection coefficient: 1 for an ideal setup with closed end and -1 for an open end. The negative sign is due to the 180° phase shift between the forward and backward traveling wave.

Figure 3.15 and Figure 3.16 depict the effect of wave phasing in term of pressure drop for the double hole 7° jet pump and 18° jet pump respectively. For other jet pump samples, readers are referred to Appendix B. The results show that different terminations do not give significant effect as the experimental results overlay each other. The only difference lies on the open setup of the 18° jet pump experiment that shows a higher pressure drop.

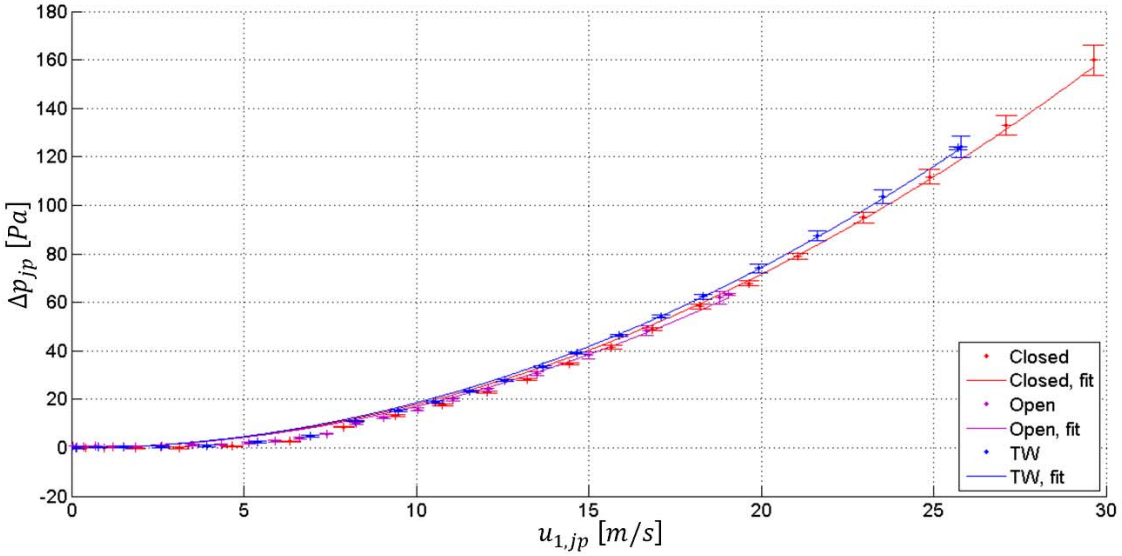

Figure 3.15 Effect of wave phasing on pressure drop for low taper angle jet pump.

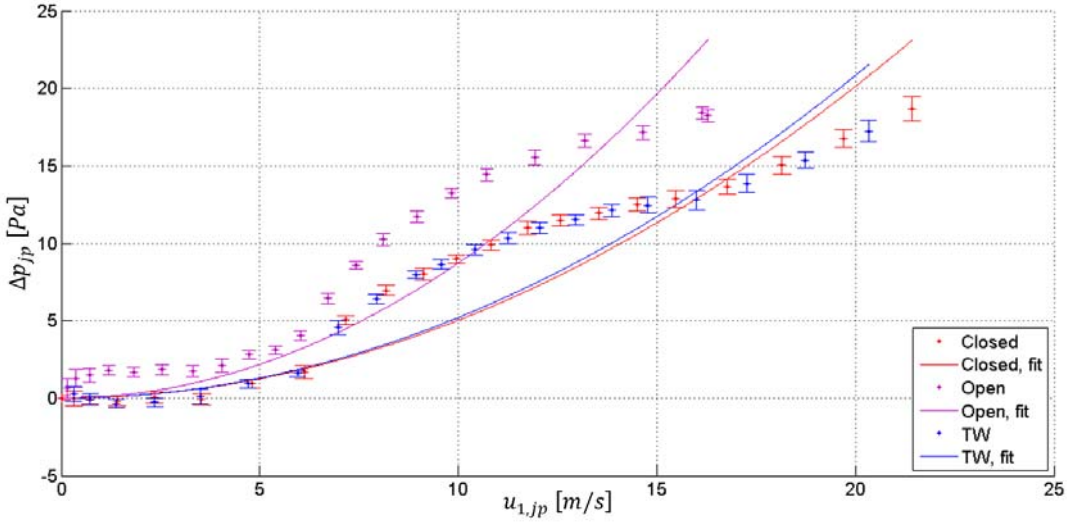

Figure 3.16 Effect of wave phasing on pressure drop for high taper angle jet pump.

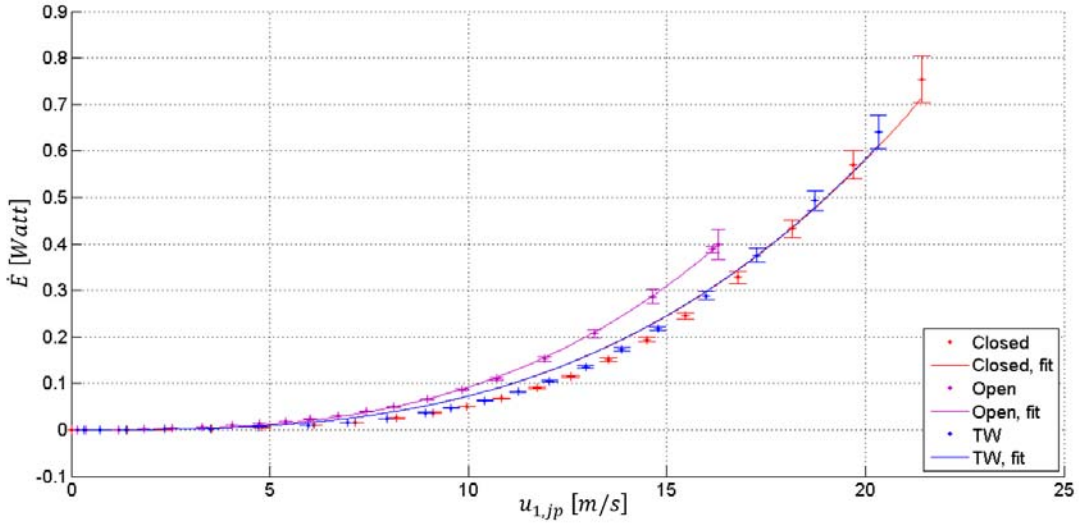

Figure 3.17 Effect of wave phasing on power dissipation for the 18° jet pump.

In terms of acoustic power dissipation, the results of the closed setup and the setup with traveling wave termination do not differ significantly. The open end gives higher value for all samples. The discrepancy between the results of open setup and other terminations could be caused by the effectiveness constant. The effectiveness constant could have incorrect scaling as indicated by the velocity amplitude shift in Figure 3.16 and Figure 3.17. The result of the 18° jet pump in as open setup has the same magnitude as the other two cases but with velocity amplitude shifted.

3.3.1.4. Estimation of experimental minor loss coefficients

The estimation of minor loss coefficients for the oscillatory flow, the forward flow and the backward flow was done to check the applicability of the minor loss coefficient for steady flow for oscillatory flow. In Chapter 3.3.1.1, it is suggested that the minor loss coefficient for backward steady flow gives higher deviation than the forward steady flow compared to the experimental result (Case B). In order to check this hypothesis, the values of the experimental minor loss coefficients are determined.

From the pressure drop and power dissipation measurement, two parameters can be calculated, namely the minor loss coefficient for the forward flow K_{out} (to the left hand side of Figure 3.2) and backward flow K_{in} (flow to the right). The subtraction of these two parameters define the total minor loss coefficient K_{tot}. Firstly, the total minor loss coefficient is obtained from the quadratic fit in Figure 3.3 but for all setup terminations. The results are compared to the theoretical value and are presented in Figure 3.18. The theoretical value is obtained using the Borda-Carnot formula for calculating K_{exp} from the measured jet pump dimension. The minor loss coefficients for contraction K_{cont} are taken from Reference [2].

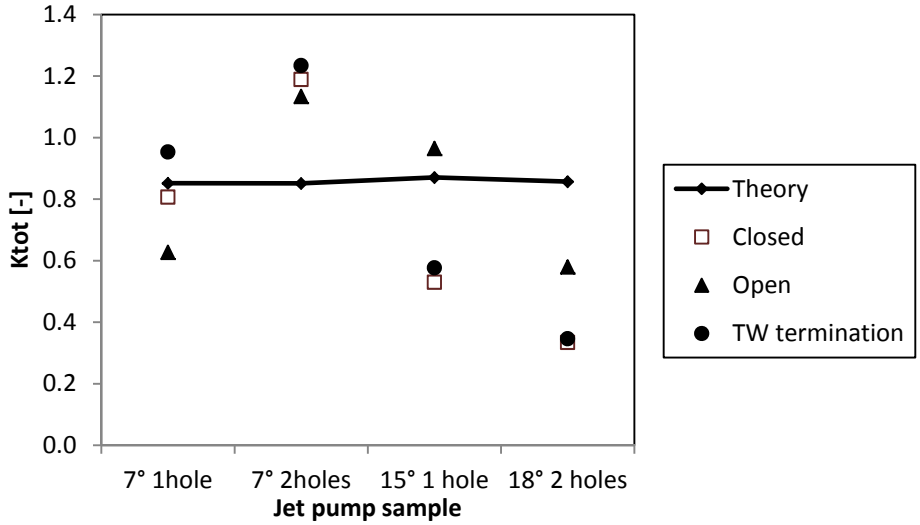

Figure 3.18 Total minor loss coefficient of the jet pump samples.
Note that the total minor loss coefficients obtained for high taper angle jet pumps do not represent the real values due to the poor curve fitting.

It should be noted that the Backhaus and Swift model for the pressure drop (Equation (3.1)) does not hold anymore for high taper angle jet pumps at low pressure amplitude (less than 25 m/s). The experimental K_{tot} that is obtained from the curve fitting based on this model can be misleading because the behavior of these jet pumps at high velocity amplitude is not known due to the limit of the loudspeaker. Nevertheless, the values of K_{tot} are in the same order of magnitude with the theoretical value. These values can be used to predict the total minor loss coefficient of the high taper angle jet pumps if experiments at higher velocity amplitude are to be performed. According to the curve fitting for the pressure drop, if one assumes a quadratic behavior continues at higher velocity amplitude, then the magnitude of the total minor loss coefficient for these samples will be lower than the ones shown in Figure 3.18.

There is a possibility that the Bakchaus and Swift model still holds and that the total minor loss coefficient varies as a function of velocity amplitude. According to Figure 3.16, there are three regions which lead to different K_{tot}, i.e. the region from 0 to 6 m/s, 6 to 15 m/s, and higher than 15 m/s. From Figure 3.16, it can be seen that the experimental data show a tendency to form a quadratic trend at high velocity amplitude. However, due to the limitation of the loudspeaker, this argument cannot be investigated at the moment and is left for future work.

It can be seen from Figure 3.18 that the theoretical value of K_{tot} deviate between -40% to 45% compared to the experimental values. These deviations will be investigated further by looking at the experimental K_{in} and K_{out} to know which component gives more contribution to the deviation of K_{tot}. Using a cubic fit to the power dissipation curve and the known experimental K_{tot} from the pressure drop measurement, the following results are obtained.

The minor loss coefficients obtained from the Borda-Carnot equation and the minor loss coefficient for contraction from Reference [2] are compared to the experimental values. The theoretical minor loss coefficients are calculated from the dimension of the measured jet pump samples. All experimental results are higher than the theoretical values. The values for experiments using traveling wave termination are also higher than the values for experiments using the closed end, except for the 18° jet pump. Since all theoretical values deviates from the experimental values, it is desired to know which component of K_{tot} gives larger contribution to the deviation.

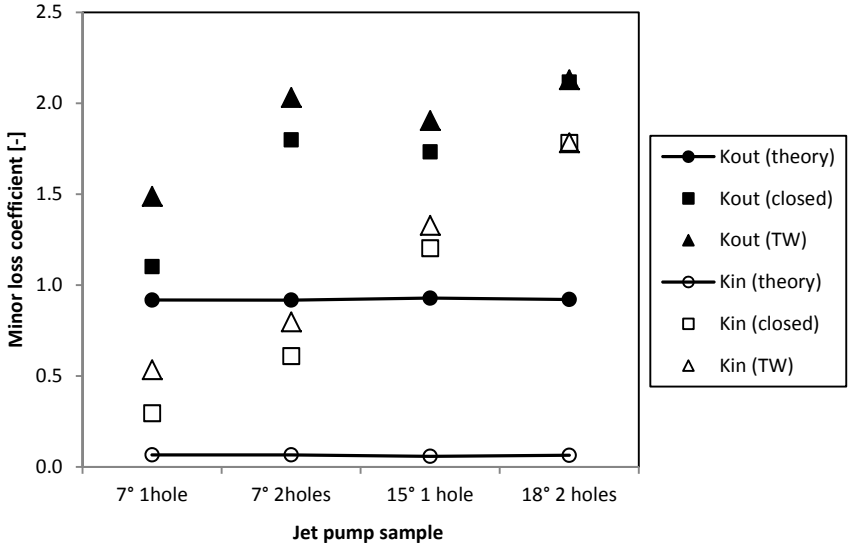

Figure 3.19 Experimental K_{out} and K_{in} of jet pump samples.

It can be seen from Figure 3.19 that the theoretical values of K_{out} deviate from 0.2 to 2.2 times the experimental value. On the other hand, the theoretical values of K_{in} give a significant deviation up to 20 times the experimental value. Moreover, the theoretical value of K_{in} is 10 times lower than the theoretical value of K_{out}. This does not result from the experimental values and the order of magnitude of K_{in} is the same as K_{out}. The order of magnitude of K_{in} and K_{out} are in a good agreement with the experiments of Petculescu and Wilen [7]. His experiments in both steady flow and oscillatory flow using a single hole 7° jet pump with $R_{curv}/(2\ R_{s,min}) = 0.3$ result in a value of $K_{out} = 1.05$ and $K_{in} = 0.55$. He also reveals that higher taper angle jet pump results in a higher minor loss coefficients, as well as higher deviation of K_{in} to the theoretical value.

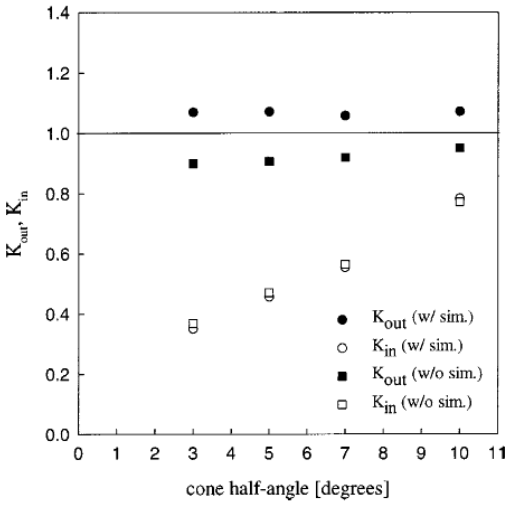

(a) Minor loss coefficients as a function of taper angle. Values from numerical simulation are marked with circle; experimental values are marked with square.

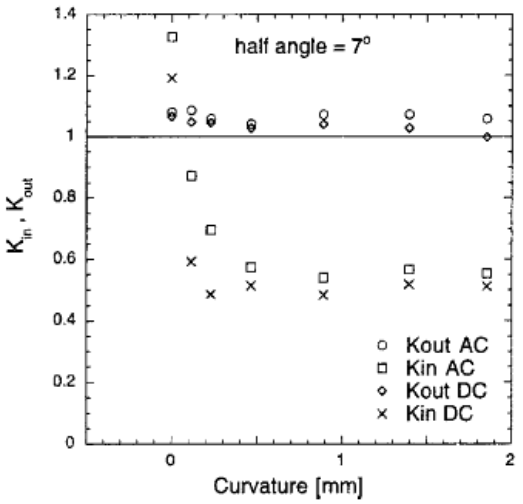

(b) Minor loss coefficients for 7° jet pump with varied R_{curv}. Curvature of 0.45 mm results in $R_{curv}/(2\ R_{s,min}) = 0.3$.

Figure 3.20 Experimental results of Petculescu and Wilen [7].

The hypothesis that the minor loss coefficient for steady flow cannot be applied to the oscillatory flow remains true if the Iguchi hypothesis holds. However, it is unlikely that the

Iguchi hypothesis does not hold because it has been confirmed by Petculescu and Wilen [7] from their steady flow measurements. Nevertheless, to confirm the hypothesis that the minor loss coefficient for steady flow cannot be applied to the oscillatory flow, a steady flow measurement needs to be performed and this work is left for future research.

In conclusion, the backward flow (to the right hand side of the jet pump) highly influences the total minor loss coefficient for oscillatory flow. The experimental results confirm that the Borda-Carnot equation for K_{exp} and the values of K_{cont} that are taken from literature cannot be applied for oscillatory flow. The quasi-steady model of Backhaus and Swift [2] holds for the case of 7° jet pumps. For high taper angle jet pumps, this model does not hold for velocity amplitude lower than 25 m/s.

3.3.2. Flow visualization

The flow visualization was conducted to get a better understanding on the flow pattern which could explain the results of the pressure drop and power dissipation measurement. In the scope of this thesis, the flow visualization experiment was performed to know whether the smoke wire method is sufficient to capture the flow pattern. If so, this method can be used for future research with other jet pump samples. The obtained flow patterns will also be a reference for flow visualization of other jet pump samples.

The jet pump sample used in this experiment is the single hole 7° jet pump only. The experiment to obtain the flow patterns was performed at fixed frequency and velocity amplitude. The gas oscillation and two flow patterns are visible during this experiment and the flow patterns are described in Chapter 1.1.1. Another flow pattern was observed in the form of vortex ring propagating away from the jet pump hole. The experiment to capture the vortex ring propagation was done at four frequencies: 28, 56, 80 and 169 Hz to know the effect of different frequencies to the vortex propagation speed. The propagation speed is then calculated and is presented in Chapter 3.3.2.2.

3.3.2.1. Description of flow patterns

The flow patterns originated by a jet pump in oscillatory flow could give useful information to interpret the results of pressure and power measurement. The information on the flow patterns of the single hole 7° jet pump in oscillatory flow could also be a reference for future flow visualization experiments with other jet pump samples. For example, future research could apply the flow visualization to the multiple hole jet pumps. In that case, the flow patterns of the single hole jet pump can be a reference.

In this section, the gas movement due to oscillatory flow is described. The gas movement can be observed clearly near the smoke wire. Using a frame rate of 1000 fps, the high speed camera is able to capture the flow every 0.001 s. This time scale is ten times lower than the wave period of 113 Hz, thus it is possible to see the gas parcel displacement of one wave period within ten images. Figure 3.21 depicts this phenomenon that happens around the smoke wire. During the first half of the cycle, the smoke shifts to the left and is indicated by the trails of white smoke on the left side of the smoke wire. During the next half cycle, the smoke shifts back to the right. This movement can be observed within 9 frames. This duration is in accordance with the period of one cycle for 113 Hz (0.0088 s), therefore the smoke movement can be associated to the movement of the gas parcel due to the acoustic field.

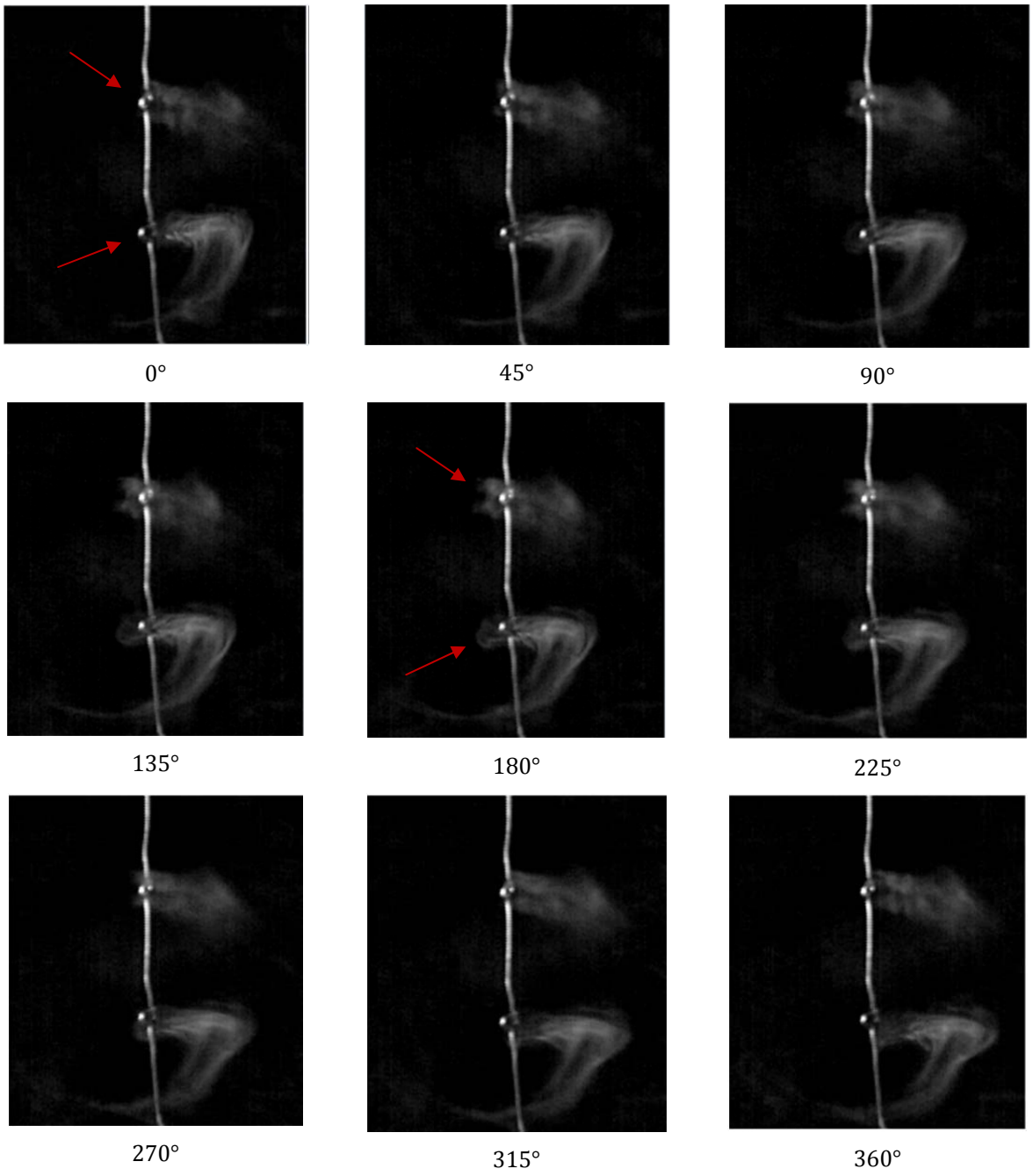

Figure 3.21 Gas oscillation.
Obtained for the single hole 7° jet pump at 113 Hz and velocity amplitude of 10.5 m/s using setup with closed termination.

Another mean flow is observed at velocity amplitude of 10.5 m/s (Figure 3.22). The jet pump sample is located at the right hand side of the picture. It can be seen that the smoke line moves while rotates with respect to the jet pump axis and propagates into the jet pump. It is observed that this smoke trail is formed at the outer surface of the jet pump hole, hence visualizing the outer flow. After 0.181 s, this outer flow is sucked into the jet pump as indicated by the strong line of smoke close to the hole at the right hand side of the last picture.

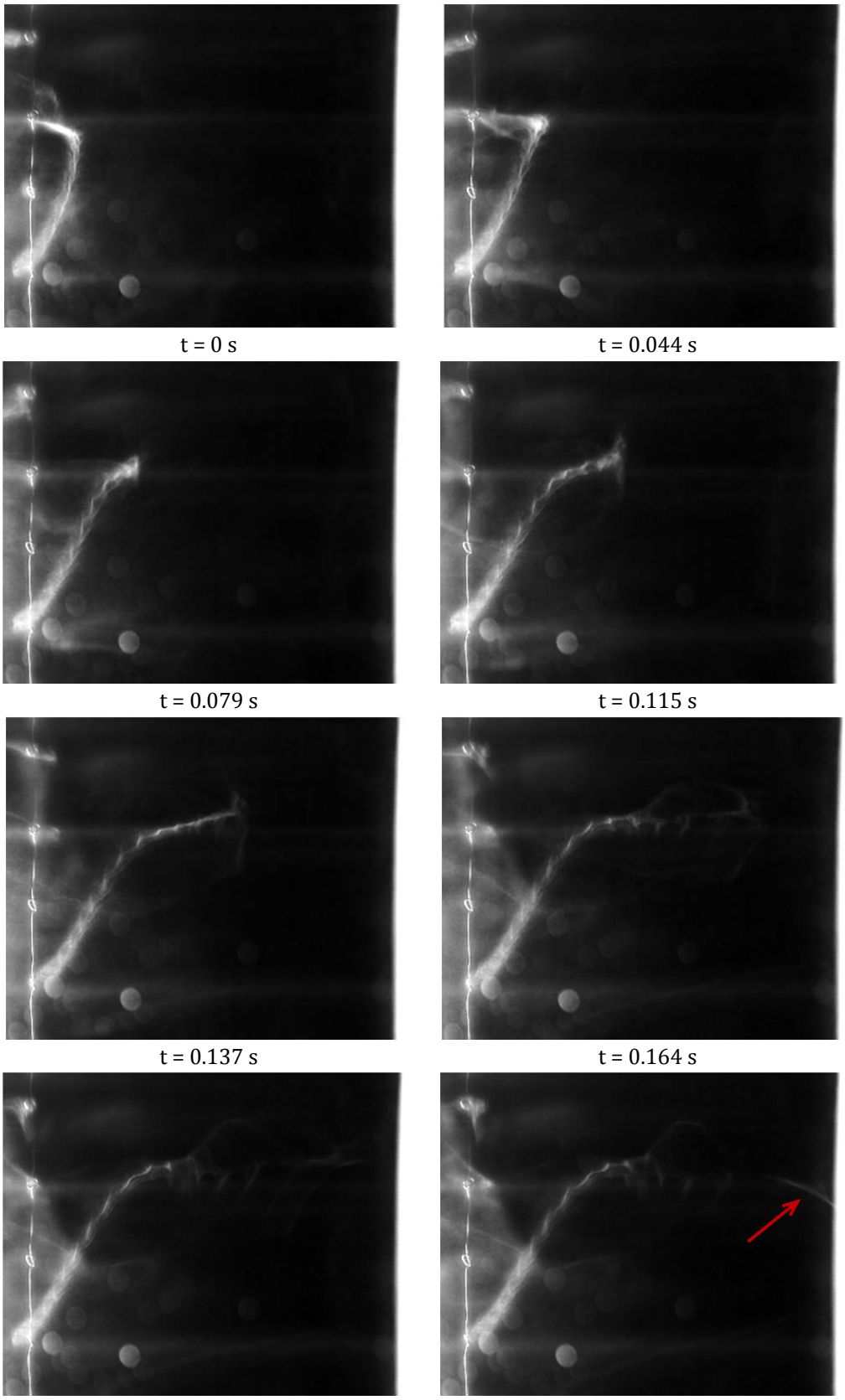

Figure 3.22 Trail of smoke sucked into the jet pump.
Obtained for the single hole 7° jet pump at 113 Hz and velocity amplitude of 10.5 m/s using setup with traveling wave termination.

An outburst flow is visible at low velocity amplitude of about 1.5 m/s. The length of the jet flow is about 3 cm from the jet pump opening. This flow was observed 345 s after the first image was taken. The phase angle of the pressure is 348°. However, this kind of outburst flow is not visible at higher velocity amplitude. This may be causes by the high velocity of the outburst flow so that the smoke particles are dispersed rapidly.

Figure 3.23 Outburst flow.
Obtained for the single hole 7° jet pump at 113 Hz and velocity amplitude of 1.5 m/s using setup with traveling wave termination.

Two flow patterns and the gas oscillation are visible during the flow visualization experiment. The utilization of the high speed camera also gives contribution to capture the gas oscillation and more detailed evolution of the flow pattern over a short period of time. In conclusion, the smoke wire method can be used for further research to obtain the flow pattern generated by a jet pump in oscillatory flow.

3.3.2.2. Vortex detection and propagation speed calculation

The flow visualization was performed at 28, 56, 80 and 169 Hz with fixed velocity amplitude of 13, 13.5, 17 and 16 m/s respectively. From this experiment, a vortex ring propagates away from the jet pump is visible. The propagation of the vortex ring is visible if the captured frames are shown in sequence as a video recording such that the successive movement of the vortex ring can be distinguished. If one looks into one captured frame only, the vortex ring is indistinguishable from the surrounding. The vortex ring is visible in the recording as a black line moving away from the jet pump hole only when there is a large amount of smoke in the test section. Due to the position of the smoke wire at the downstream of the jet pump, the vortex ring cannot be captured as a ring of smoke propagating away from the jet pump opening.

In order to get a picture of a ring of smoke propagates away from the jet pump, it was tried to insert the smoke at the right hand side of the jet pump. A smoke generator that has been used for previous flow visualization experiment of van Dixhoorn [9] and Lamboo [28] is utilized. However, this method is unsuccessful. There is a possibility that the smoke particle is too heavy to be carried out by the vortex, or the propagation and the rotation speed is so fast that the smoke particle cannot last long enough in the vortex ring.

It was observed that the vortex ring rotates with respect to the torus axis. The direction of the rotation of the vortex ring can be observed when it passes the smoke wire. The newly produced smoke is dispersed to the left hand side of the picture as the vortex ring touches it. Figure 3.24 gives the schematic drawing of the rotational direction of the vortex ring.

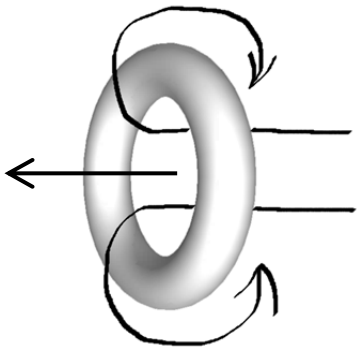

The rotational direction of the vortex ring. The jet pump is placed at the right hand side of the image and the vortex ring propagates away from the jet pump.

Figure 3.24 Schematic of vortex ring propagation and rotational direction.

The formation of a vortex ring is caused by the forward propagating wave that forces the gas inside the jet pump to rotate while traveling forward along the jet pump length. When the next half of the cycle occurs, the vast majority of the gas parcel is sucked into the jet pump. A part of the gas parcel that has passed the jet pump opening is thrown into the bigger space of the PMMA tube, while the rest is sucked into the jet pump. The gas parcel that is released to the PMMA tube then travels away from the jet pump opening.

The generation of the vortex ring is caused by the acoustic field. It was confirmed that the vortex ring is generated near the jet pump hole every ten pictures. Since the time step between two captured frame is 0.001 s, the duration between the formation of two consecutive vortices is approximately the wave period of 113 Hz (0.0088 s).

The velocity of the vortex propagation is determined to compare with the gas velocity at the center of the jet pump hole. It is expected that the vortex propagation velocity (or celerity) has a different value than the gas parcel velocity [34]. Figure 3.25 shows an example of the vortex detection process. From the recordings, the images are processed and the edge detection is applied. The image processing is useful to give a better visualization of the vortex movement and to determine the vortex propagation speed for the future work.

The vortex edge is marked with green line and its centroid location is shown by the yellow line. The vortex ring appears in darker color, thus it can be distinguished from the surroundings using a color threshold. The selection of the vortex is done based on the black colored area and its location in the frame. Minimum and maximum thresholds for area are set such that the black area with unreasonably high or low value will not be considered as a vortex. The location of the vortex is also considered, i.e. the black area roughly in the middle of the frame will be considered as a vortex while other black area that appears near the edge of the frame will be marked with magenta line. Other black areas that satisfy the color threshold but do not comply the area threshold will be marked with red line, e.g. the third picture of Figure 3.25. The original pictures of the sequence shown in Figure 3.25 are presented in Appendix D.

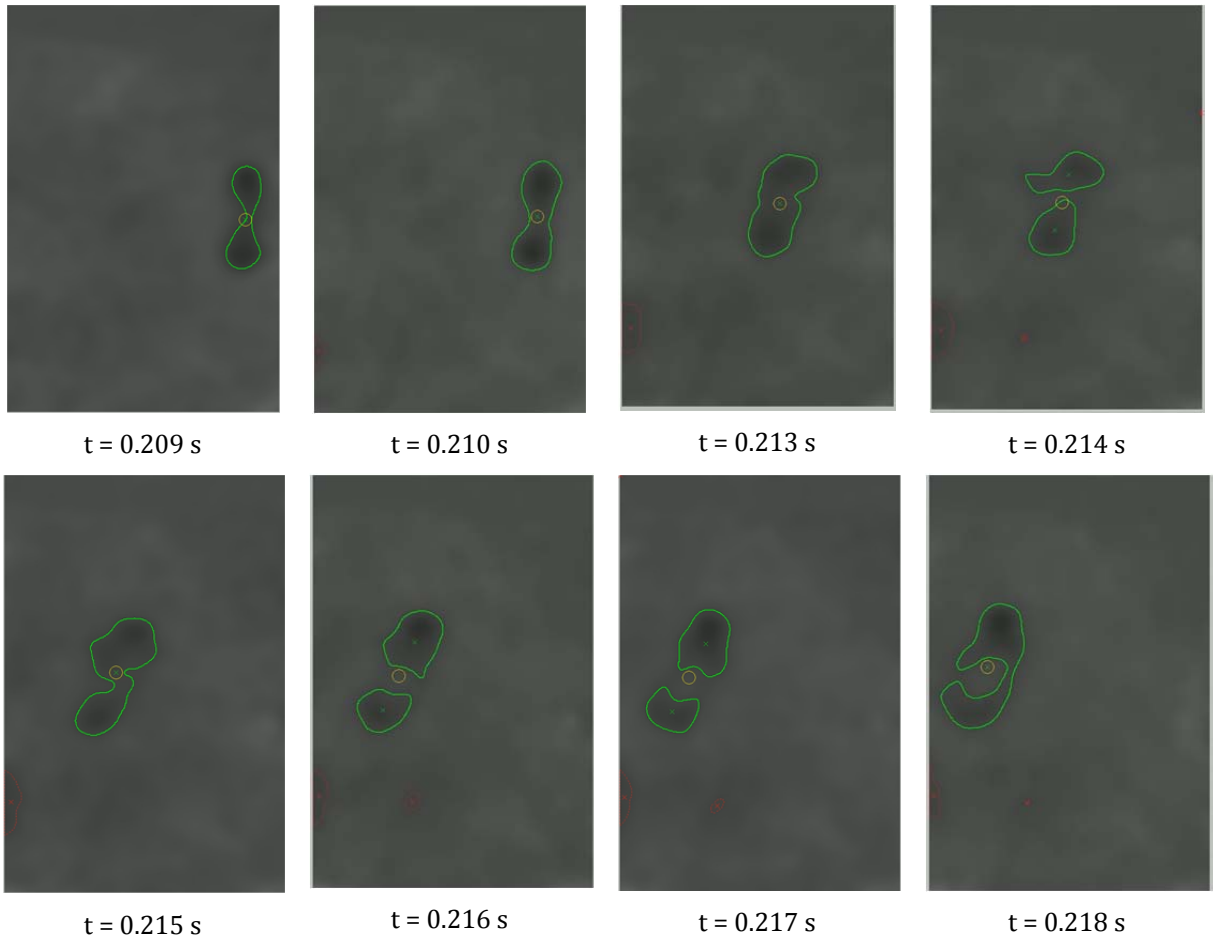

Figure 3.25 Vortex edge detection.
Obtained for the single hole 7° jet pump at 80 Hz and velocity amplitude of 10.5 m/s.

The vortex propagation speed is determined by manually measuring the distance traveled by the vortex over a certain time. The pictures used for this measurement is the original picture without any image processing. The vortex propagation speed is expressed in Equation (3.17).

$$u_v = x_v \frac{fps}{n} \tag{3.17}$$

where fps is the frame rate and x_v is the distance traveled by the propagating vortex, which is measured manually. n is the number of frame taken to see the propagating distance x_v. From the recordings of the high speed camera, twenty vortex rings per frequency are measured manually and its propagation speed is calculated. The average value of the twenty measurements is depicted in Figure 3.26 with the standard deviation of the twenty measurements presented by a vertical error bar. Experiment 1, 2, 3 and 4 refers to the experiment at 28, 56, 80 and 169 Hz. The error bars show that the standard deviation reaches 30%. Therefore, it is suggested not to use the manual measurement for further experiments.

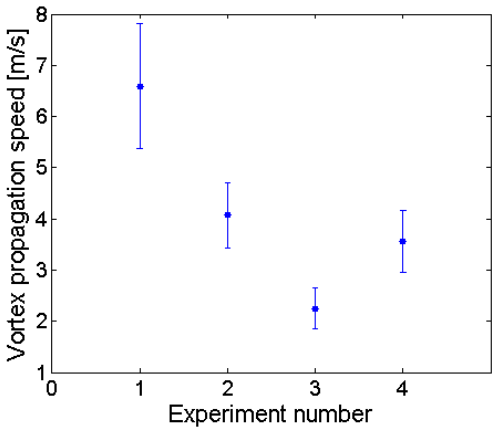

Figure 3.26 Vortex propagation speed as a function of frequency.

The vortex propagation speed is calculated to know whether or not it has the same value as the gas parcel velocity. The gas parcel velocity is measured from the gas displacement at the center line of the jet pump. However, this measurement could not be performed because the smoke at this location is immediately dispersed by the propagating vortex. The vortex ring highly influences the movement of the smoke so that the gas oscillation cannot be seen during the period between the formation of two subsequent vortices. One way to obtain the gas parcel velocity is by performing the flow visualization inside the jet pump, thus visualizing the gas displacement at the jet pump waist. To achieve this, the manufacturing of a jet pump sample with transparent material should be considered. Nevertheless, the results of the vortex propagation speed could be useful as a reference for future research.

The experimental results of flow visualization show that the smoke wire method cannot mark the vortex ring propagation, probably because the smoke particle is too heavy to be carried away by the propagating vortex. Other smoke fluid with lighter particles could solve this problem. Nevertheless, the flow visualization using the smoke wire method needs additional image processing and vortex tracking to obtain the vortex propagation speed. Otherwise, other method of flow visualization should be considered.

In conclusion, the flow visualization using a smoke wire can mark the flow patterns generated by jet pump is oscillatory flow. The flow patterns obtained for the single hole 7° jet pump can be a good reference for future work with other jet pump samples, for example experiments with the double hole jet pump to check the recirculation zone or with the high taper angle jet pump to observe the vena contracta formation. The image processing to detect the vortex propagation has been applied successfully. If this method is to be applied for further research, the image processing can be used to obtain the vortex propagation speed without performing any manual measurement of the vortex displacement.

3.4. Summary

From the pressure and power measurement, several parameters can be obtained, such as time-averaged pressure drop, acoustic power dissipation, total minor loss coefficient, minor loss coefficient for the forward flow and backward flow. The effect of taper angle, number of holes and wave phasing are determined. The experimental results of the high taper angle jet pumps confront the quasi-steady model of Bakchaus and Swift [2], hence the assumption on Backhaus

and Swift model does not hold for high taper angle jet pump. The second assumption on the theoretical value of minor loss coefficient for expansion and contraction also fails, suggesting that the formula and typical values for steady flow cannot be used for oscillatory flow.

The smoke wire method was performed to visualize the flow near the exit region of the jet pump. From this experiment, the gas parcel oscillation can be observed. A mean flow that is sucked into the jet pump is also visible as well as an outburst flow at low velocity amplitude. The propagation of a vortex ring can be seen and the vortex propagation speed is calculated for four experiments at different frequencies. An edge detection method has been implemented and the vortex ring can be detected using this method.

CHAPTER 4

CONCLUSION AND RECOMMENDATION

In this chapter, the research questions mentioned in Chapter 1 will be answered. The modification of the standing wave experimental setup into a traveling wave setup has been done successfully. A series of experiments have been performed using both the standing wave and traveling wave setup to investigate the effects of different jet pump geometries. The flow visualization experiment was also performed and the flow patterns generated by a jet pump in an oscillatory flow can be visualized. The conclusion and recommendations will be presented in the following sections.

4.1. Conclusion

The design and manufacture of the traveling wave termination, the smoke wire test section, and the realization of four jet pump samples have been done. In order to perform experiments in a traveling wave, a one-dimensional model to design a traveling wave termination has been realized and validated. Using this model, a traveling wave termination is designed and manufactured. This termination works best at 113 Hz with absorption coefficient of 99.9%. A nonlinear behavior was observed during the experiment using empty setup with the traveling wave termination: the absorption coefficient decreases nonlinearly with increasing pressure amplitude. This result also gives information for determining the operational range of the traveling wave setup. The test section for flow visualization has also been realized. This test section acts as a mounting for the jet pump sample as well as the mounting for the smoke wire. The selection of the smoke wire, the smoke liquid, the lighting position and high-speed camera settings has been done to obtain the best picture quality. Finally, four jet pump samples have been designed with various geometries. These jet pump samples have been tested together with the traveling wave termination to make sure that a traveling wave exists in the setup. The result of this experiment is then compared to that of the closed setup. In conclusion, the traveling wave termination can generates traveling wave with the jet pump mounted in the setup.

The experiment consists of two kinds: pressure measurement and flow visualization. The pressure measurement was carried out for all jet pump samples, each with three different terminations. From this experiment, it was found that the taper angle and the number of holes influences the pressure drop and power dissipation. The experimental minor loss coefficients for oscillating flow, forward flow and backward flow are also obtained. From this experiment, it is concluded that the model of Backhaus and Swift for calculating the pressure drop does not hold for high taper angle jet pump. Other assumption on the theoretical value of minor loss coefficient for expansion and contraction of a steady flow also fails, suggesting that the formula and typical values for steady flow cannot be used for oscillatory flow.

The experimental minor loss coefficient for oscillatory flow, forward flow and backward flow confirm that the formula and typical values of minor loss coefficient for steady flow are not applicable to oscillatory flow. The experimental values are compared to the theoretical values taken from the Borda-Carnot formula and the typical contraction coefficient from Reference [2]. The theoretical value of K_{tot} deviates in the range of -40% to 45% compared to the

experimental values, while the theoretical K_{out} deviates from 0.2 to 2.2 times the experimental value and the theoretical K_{in} give a significant deviation up to 20 times lower. The experimental results are in the same order of magnitude with the experiments of Petculescu and Wilen [7], thus supporting the hypothesis that the minor loss coefficient for steady flow cannot be applied to the oscillatory flow.

However, the abovementioned argument remains as a hypothesis because no measurement in a steady flow was performed to confirm the Iguchi hypothesis. Therefore, it is necessary to perform the steady flow measurement and obtain the value of K_{in} and K_{out} from this experiment. The steady flow measurement was not carried out in this thesis and is left for future research.

From the flow visualization experiment using a smoke wire, the gas oscillation can be observed, as well as the mean flow. The high speed camera is able to capture different flow patterns that occur between 1 millisecond intervals. The obtained flow pattern could be a useful reference for future flow visualization experiments with other jet pump samples. Two flow patterns are visible: one at the outer boundary of the jet pump where the smoke is sucked into the jet pump while also rotating with respect to the jet pump center line, and the outburst flow at low pressure amplitude. However, the smoke wire method cannot mark the vortex ring propagation sufficiently so that an additional image processing is needed.

The vortex propagation speed is determined for each frequency by manually measuring the vortex displacement from the original images. The information on the vortex propagation speed is useful for further research with other jet pump samples. The image processing has been applied and the edge detection is able to visualize the propagation of the vortex. This image processing could be used in the future to calculate the vortex propagation speed so that no manual measurement is needed.

Finally, it can be concluded that the modification of the standing wave experimental setup into a traveling wave setup has been done. The pressure drop and power dissipation measurements have been carried out and the effects of taper angle, number of hole, and wave phasing are determined. The minor loss coefficients for oscillatory flow, forward flow and backward flow have been determined from the experimental data to check the applicability of the three assumptions. The flow visualization can capture several flow patterns for the 7° jet pump. Nevertheless, further research and improvement are needed to confirm the results obtained in the scope of this thesis.

4.2. Recommendation

Further research and improvements are needed in order to confirm the hypothesis proposed in this thesis. In order to check the validity of the Iguchi hypothesis, it is necessary to perform pressure and power measurement in a steady flow. Moreover, the minor loss coefficients for the forward and backward flow should be determined from this experiment to confirm the experimental values of K_{in} and K_{out} obtained in this thesis.

The pressure drop measurement for high taper angle jet pump at higher velocity amplitude also needs to be carried out to confirm the validity of the Backhaus and Swift model at high velocity amplitude. Due to the limitation of the loudspeaker, this experiment cannot be performed at the moment.

From the pressure measurement, the velocity amplitude can be determined. The determination of the velocity amplitude is approximated using a numerical simulation because it cannot be directly measured from the experiment. One way to solve this problem is by using the smoke wire as a hot wire anemometer. By measuring the temperature change or electric current change over the wire, the velocity at the jet pump waist can be estimated. A more accurate method is by visualizing the flow inside the jet pump sample. Thus, a transparent jet pump sample is needed so that the gas displacement inside the jet pump can be determined. Subsequently, the velocity inside the jet pump can be determined as well.

The flow visualization test section is sufficient to be used at the moment. However, there are some issues that need to be resolved. First, the jet pump sample is inserted through one end of the PMMA tube. This method can be applied for the currently used jet pump samples, however difficulties will arise if the jet pump sample has a very compact shape. Moreover, by inserting the jet pump sample from one end and push it halfway through the tube, there is a chance that the tube wall will be scratched. Therefore, a new design to mount the jet pump sample as well as the smoke wire should be considered for future research. The new test section could consist of three parts: two PMMA tubes that clamp another PMMA tube which serves as a mounting for the jet pump and the smoke wire. Furthermore, this design allows the user to easily clean the PMMA tube from the smoke particles that are patched to the tube wall.

Second improvement of the current smoke wire test section can be done by making a smoke liquid injection system. At the moment, the smoke liquid injection depends solely on the gravitational force, therefore its flow rate cannot be controlled. A pressurized liquid injection system will be favorable to control the liquid flow rate. A suction system at the bottom of the smoke wire is also needed to dispose the excess smoke liquid that is pooled at the bottom of the tube.

Other problem of the current flow visualization test section is the unwanted reflection from the PMMA tube and the aluminum bars that supports the PMMA tube. The aluminum bars have been covered with a black duct tape, however there are still some reflections coming from the duct tape. One way to solve this is by painting the aluminum bars with black coating that does not reflect light. The backside of the PMMA tube can also be painted black to give enough contrast rather than using a black cloth as a background. Other solution is by using a light sheet which has enough light intensity to be used with the high speed camera to minimize the reflection from other directions.

The current flow visualization method is unable to capture the propagation of the vortex ring, probably due to the heavy smoke particles. Other smoke liquid should be studied and tested whether it can be carried away with the vortex ring. However, other flow visualization method is also favorable. Smith and Swift [35] have succeeded in applying a Schlieren technique to visualize a synthetic jet (or a jet flow in oscillatory flow). This method works based on the density change of the fluid, i.e. the change of density results in a different refractive index which cause light to refract within the fluid [16]. The change of the direction of the light result in a more shadowed area compared to the one of the unchanged density. Hence, this shadowed area can be visualized.

BIBLIOGRAPHY

[1] in 't Panhuis, P.H.M.W. (2009). *Mathematical aspects of thermoacoustics* (Doctoral dissertation). Technische Universiteit Eindhoven, The Netherlands.

[2] Backhaus, S., & Swift, G.W. (2000). A thermoacoustic-Stirling heat engine: Detailed study. *Journal of Acoustical Society of America,* **107,** 3148-3166.

[3] Aben, P.C.H. (2010). *High-amplitude thermoacoustic flow interacting with solid boundaries* (Doctoral dissertation). Technische Universiteit Eindhoven, The Netherlands.

[4] TAP-SBIR09313. Retrieved 13 November 2013 from http://www.aster-thermoacoustics.com/

[5] Pennsylvania State University. (2010). Retrieved 13 November 2013 from http://www.acs.psu.edu/thermoacoustics/

[6] Boluriaan, S., & Morris, P.J. (2003). Acoustic streaming: from Rayleigh to today. *International Journal of Aeroacoustics,* **2**(3-4), 255-292.

[7] Petculescu and Wilen, A., & Wilen, L.A. (2003). Oscillatory flow in jet pumps: Nonlinear effects and minor losses. *The Journal of the Acoustical Society of America,* **113**(3), 1282-1292.

[8] Iguchi, M., Ohmi, M., & Maegawa, M. (1982). Analysis of free-oscillating flow in a U-shaped tube. *Bulletin of the JSME,* **25**(207), 1398-1405.

[9] van Dixhoorn, F. (2014). *Visualization and pressure measurements of the oscillatory flow in a jet pump* (Bachelor thesis). University of Twente, Enschede, The Netherlands.

[10] van der Gun, D. (2013). *Design and realization of an experimental thermoacoustic setup* (Master thesis). University of Twente, The Netherlands.

[11] van der Eerden, F.J.M. (2000) *Noise reduction with coupled prismatic tubes* (Doctoral dissertation). University of Twente, The Netherlands.

[12] Tijdeman, H. (1975). On the propagation of sound waves in cylindrical tubes. *Journal of Sound and Vibration,* **39**(1), 1-33.

[13] National Aerospace Laboratory NLR, NLR-TR F.238. (1965). *Theoretical and experimental results for the dynamic response of pressure measuring systems.* Amsterdam: Bergh, H. and Tijdeman, H.

[14] Levine, H., & Schwinger, J. (1948). On the radiation of sound from an unflanged circular pipe. *Physical Review,* **73**(4), 383-406.

[15] Bies, D.A., & Hansen, C.H. (1996). *Engineering Noise Control: theory and practice.* London: E&FN SPON.

[16] Tropea, C., Yarin, A.L., & Foss, J.F. (2007). *Springer Handbook of Experimental Fluid Mechanics*. Berlin, Heidelberd: Springer Berlin Heidelberg.

[17] Merkli, P., & Thomann, H. (1975). Transition to turbulence in oscillating pipe flow. *Journal of Fluid Mechanics,* **68**(3), 567-575.

[18] Ingård, U., & Labate, S. (1950). Acoustic circulation effects and the nonlinear impedance of orifices. *The Journal of the Acoustical Society of America,* **22**(2), 211-212.

[19] Glycerine Producers' Association. (1963). *Physical Properties of Glyceringe and its Solutions*. New York: American Cleaning Institute.

[20] Eurolite smoke fluid data sheet. Retrieved 18 August 2014 from http://prosklep.pl/download/00055627.pdf

[21] Safex smoke fluid data sheet. Retrieved 18 August 2014 from https://www.google.nl/url?sa=t&rct=j&q=&esrc=s&source=web&cd=2&cad=rja&uact=8&ved=0CCsQFjAB&url=http%3A%2F%2Fbric.postech.ac.kr%2Fmyboard%2Fview.php%3FBoard%3Dnew_protech%26filename%3DFCCS_Safex_Safety_Documents.pdf%26id%3D1042%26fidx%3D2&ei=IDnxU_KDCMeW0QWgzoDgDQ&usg=AFQjCNF9QnhYgKf-NvdA_AyV3nTbg7ZX5g&sig2=cAaqyb4QHYZUSCBvfWbw_g&bvm=bv.73231344,d.d2k

[22] Miller., D.S. (1990). *Internal flow systems* (2nd ed.). Cranfield: BHR Group Ltd.

[23] Massey, B., & Ward-Smith, J. (Ed.). (2006). *Mechanics of Fluids* (8th ed.). New York: Taylor & Francis e-Library.

[24] Blackstock, D.T. (2000). *Fundamentals of physical acoustics.* New York: John Wiley & Sons Inc.

[25] Fusco, A.M., Ward, W.C., Swift, G.W. (1992). Two-sensor power measurements in lossy ducts. *The Journal of the Acoustical Society of America,* **91**(4), 2229-2235.

[26] Gatti, P.L. & Ferrari, V. (2003). *Applied Structural and Mechanical Vibrations: Theory, Methods and Measuring Instrumentation*. London: Taylor & Francis e-Library.

[27] Gaitan, F.D. & Atchley, A.A. (1993). Finite amplitude standing waves in harmonic and anharmonic tubes. *Journal of Acoustical Society of America*, **93**(5), 2489-2495

[28] Lamboo, S. (2013). *Setup design for flow visualization of oscillating flow* (Bachelor thesis). University of Twente, The Netherlands.

[29] Technical University of Gabrovo. Polymethyl methacrylate (PMMA). Retrieved 18 August 2014 from webhotel2.tut.fi/projects/caeds/tekstit/plastics/**plastics_PMMA.pdf.**

[30] Ruziewicz, A. (2014). *Acoustic power measurements* (Internship report). University of Twente, The Netherlands.

[31] Idel'chik, I.E. (1966). *Handbook of Hydraulic Resistance: Coefficients of Local Resistance and of Friction.* Jerussalem: U.S. Department of Commerce.

[32] Nasr and Lai. 1997. Comparison of flow characteristics in the near field of two parallel plane jets and an offset plane jet. *Physics of Fluids*, **9**(10), 2919 – 2931.

[33] Huang, R.F. & and Tsai, F.C. (2001). Flow field characteristics of swirling double concentric jets. *Experimental Thermal and Fluid Science,* **25,** 151-161.

[34] Smith, B.L. & Glezer, A. (1998). Formation and evolution of synthetic jets. *Physics of Fluids,* **10**(9), 2281-2297.

[35] Smith, B.L. & Swift, G.W. (2001). Synthetic jets at large Reynolds number and comparison to continous jets. *American Institute of Aeronautics and Astronautics*.

[36] Olsen and Swift

[37] Oosterhuis, J.P., Bühler, S., Douglas, W., van der Meer, T.H. (2014). Computational fluid dynamics analysis of the oscillatory flow in a jet pump: the influence of taper angle. *9th PAMIR International Conference.*

[38] Swift, G.W. (2002). *Thermoacoustic: A unifying perspective for some engines and refrigerators.* Acoustical Society of America.

[39] Ohmi, M. & Iguchi, M. (1982). Critical Reynolds number in an oscillating pipe flow. *Bulletin of the JSME*, **25**(200), 165-172.

APPENDIX A

TRAVELING WAVE TERMINATION MODEL

Modeling and Validation

In this section, the parameters that were used in the model and the result obtained by van der Eerden [11] will be presented and compared. Figure 0.1 shows the configuration of two tubes in series and the boundary conditions used by van der Eerden [11].

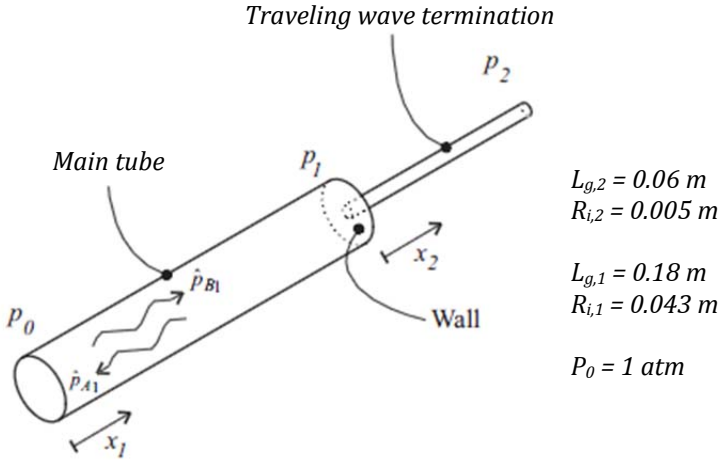

Figure 0.1 A traveling wave termination connected to the main tube in series [11].

Standard air conditions were used and the values are listed in Table 0.1.

Table 0.1 Standard air conditions.

Parameter	Unit	Value
Specific heat, *Cp*	J/kgC	1006
Mean density, $\boldsymbol{\rho_0}$	kg/m^3	1.22
Dynamic viscosity, $\boldsymbol{\mu}$	Ns/m^2	1.82e-05
Speed of sound, $\boldsymbol{c_0}$	m/s	343.3
Square root of Prandtl number, $\boldsymbol{\sigma}$	-	0.845
Ratio of specific heat, $\boldsymbol{\gamma}$	-	1.4

Note that the length L in Figure 0.1 refers to the geometrical length. Another term that is used in the model is the effective length. The effective length is equal to the geometrical length increased by an end correction and will be explained later. It was obtained by van der Eerden[11] that for such configuration, 100% absorption can be achieved for frequency 1337 Hz. Figure 0.2 shows the absorption coefficient as a function of frequency and the acoustic variables in both tubes.

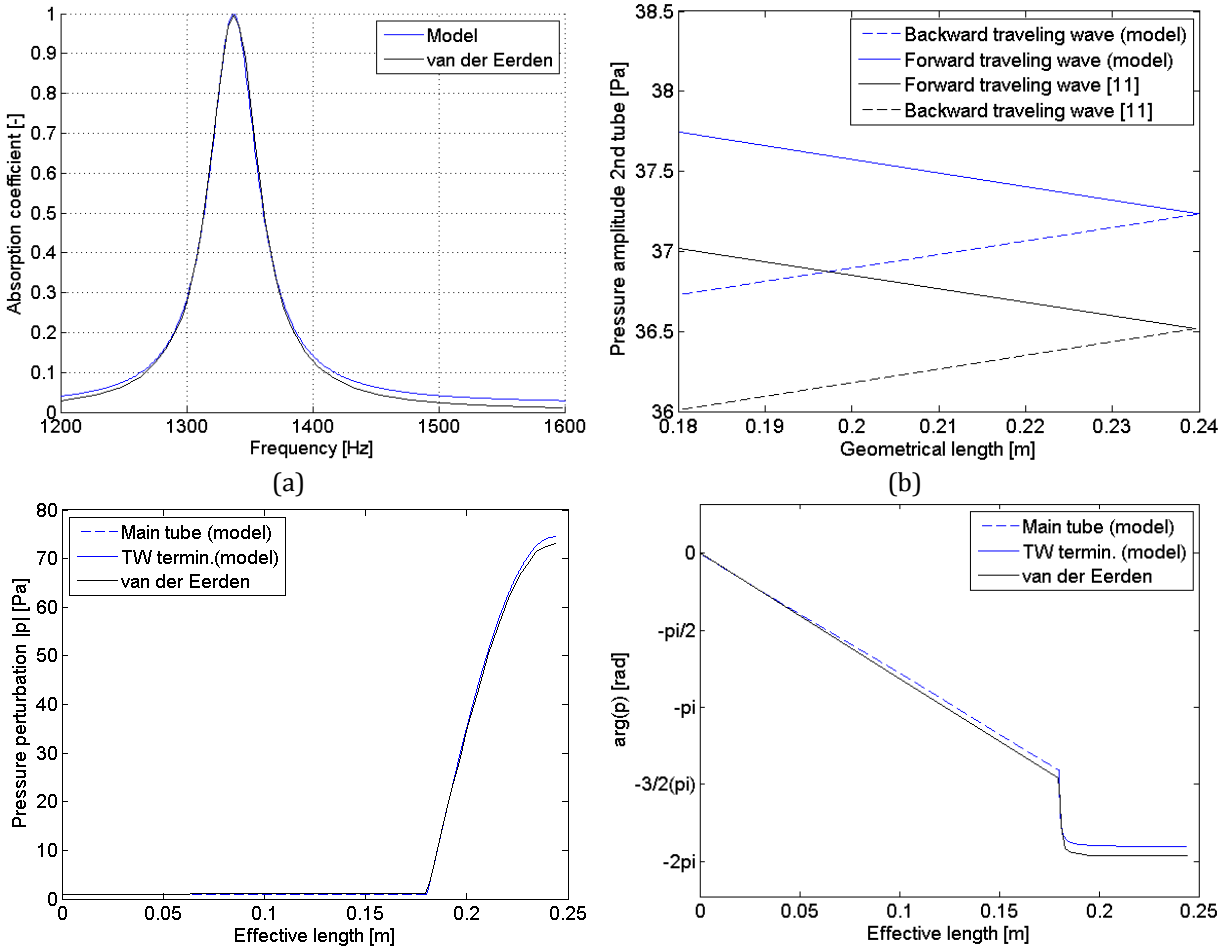

Figure 0.2 Comparison of model implementation and van der Eerden's result [11]:
(a) sound absorption coefficient as a function of frequency, (b) amplitude of the forward and backward propagating wave in the traveling wave termination, (c) pressure perturbation magnitude and (d) phase at 1337 Hz. Taken for $L_1 = 0.18\ m$ and $L_2 = 0.0636\ \ m$.

The model implementation shows a good agreement with the reference. Figure 0.2(a) indicates a maximum absorption when the frequency reaches 1337 Hz. At this frequency, it can be seen from Figure 0.2(b) that the forward and backward propagating waves behave similarly. The negative linear gradient shows that there is decay on pressure amplitude of the forward wave, followed by the same decay for the reflective wave. The same gradient of the incident and reflection wave indicates a constant attenuation inside the traveling wave termination as an effect of the wave propagation constant Γ.

Figure 0.2 (c) is also in accordance with Figure 0.2(d), which shows a traveling wave inside the main tube, marked by the constant pressure and the constant phase change. While inside the traveling wave termination, it is shown that there is relatively large pressure amplitude and a constant phase. These behaviors signify that there is a standing wave pattern inside the traveling wave termination.

Although the graphs in Figure 0.2 show the same shape with van der Eerden's result, there is a significant difference in the magnitude shown in Figure 0.2(b). The value in Figure 0.2(b) shifts about 0.7 Pa higher. The cause of this difference is not known yet since Figure 0.2(a), (c) and 3.3(d) gives exactly the same value with the reference. One possible reason is that the length

used to obtain Figure 0.2(b) is the effective length where the end correction is applied for both the main tube and the traveling wave termination.

The effective length is a corrected length that considers the inlet effect. This effect has been studied extensively by Levine and Schwinger [14], and is also mentioned by van der Eerden [11] for the geometrical length of a tube. The effective length is the geometrical length L_g increased by a small increment d. According to Rayleigh (1945,[11]), the increment d_1 for a single tube opening to an infinite baffle is:

$$d_1 = \frac{8R}{3\pi} \tag{2.44}$$

The end correction d for a single tube centrally located in a tube of circular cross-section with radius R_2 is formulated by Bies [15] as:

$$d_2 = \frac{8R_2}{3\pi}\left(1 - \frac{1.25R_2}{R_1}\right), with\ \left(\frac{R_2}{R_1} < 0.6\right) \tag{2.45}$$

The inlet effects takes place at the junction where the two tubes are connected, hence it affects the flow at the entrance of the traveling wave termination. Considering this phenomenon, it was decided to apply the end correction to the traveling wave termination only. The length of the main tube is kept uncorrected (equals to its geometrical length) due to the fact that the entrance of the main tube is connected to the cone and the loudspeaker, hence the inlet effect is neglected. This formula is proven to be correct for obtaining Figure 0.2(a), (c) and (d).

To investigate the discrepancy of magnitude in Figure 0.2(b), the end correction was applied to both tubes. Equation (2.44) was applied to the main tube, whilst the traveling wave termination uses Equation (2.45). Thus, Figure 0.3 was obtained. The pressure amplitude at the inlet of the traveling wave termination is in the same order as van der Eerden's result. The magnitude difference is only about 0.01 Pa and is constant for certain geometrical length. The difference is small, therefore it is concluded that the model can be used to design the traveling wave termination.

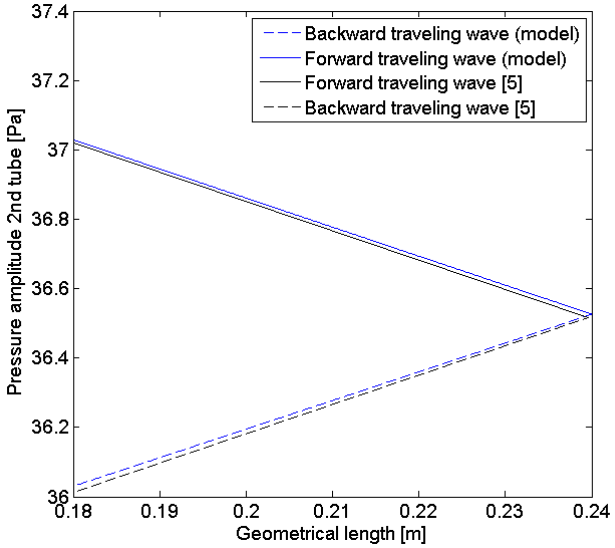

Figure 0.3 Pressure amplitude at the traveling wave termination.
The end correction is applied at both tubes ($\boldsymbol{L_1 = 0.2165\ m}$ and $\boldsymbol{L_2 = 0.0636\ m}$).

From Figure 0.2 and Figure 0.3, it can be concluded the end correction influences the acoustic field inside the setup. The difference of applying the end correction at both tubes can be seen in Figure 0.2(b) and Figure 0.3. Since the acoustic field inside the setup is influenced by the end correction, it is desired to know whether it can influence the working frequency as well. Thus, the following test was performed.

The model was run to obtain the working frequency for three different scenarios: (1) uncorrected length, (2) end correction applied at the traveling wave termination, and (3) end correction applied at the traveling wave termination and the main tube. The results are depicted in Figure 0.4. It can be seen that using the uncorrected length results in a higher working frequency than the corrected length. The end correction of the main tube does not give significant effect on the working frequency compared to the end correction of the traveling wave termination, as these two graphs overlay each other. This result is in accordance with the one obtained by van der Eerden [11]. Thus, it can be concluded that the end correction applied for both tubes does not give significant influence on the working frequency, but it influences the pressure amplitude at the traveling wave termination, as shown by Figure 0.2(b) and Figure 0.3.

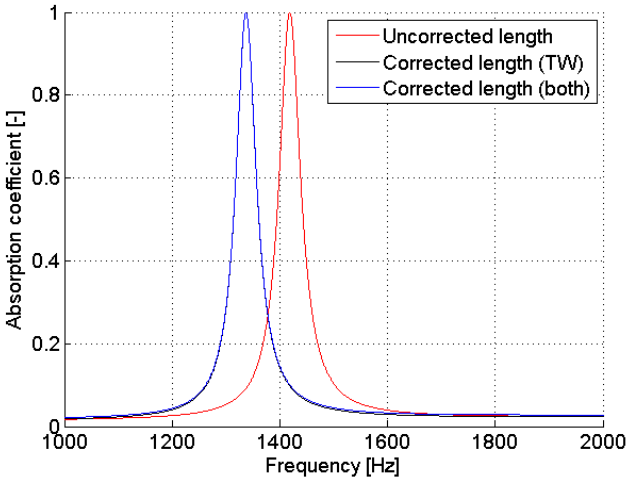

Figure 0.4 Influence of end correction.

Using the geometrical length $L_{g,1}$ and the effective length $L_{e,2}$ as an input for the model, the outcomes in Section 2.2.3 and 2.2.4 are obtained.

The traveling wave termination model

In this section, the relation between the tube radius, length, absorption coefficient and frequency will be explained. In order to know the effect of these parameters, the model was run by keeping the tube radius constant and varying the length of the tube. Afterwards, the tube radius is changed and the same procedure is repeated. For each length of the tube, a maximum absorption coefficient and its respective working frequency are obtained. Then, the model was run again for a different length and the next maximum point is obtained. The maximum points are plotted in Figure 0.5 for each tube radius.

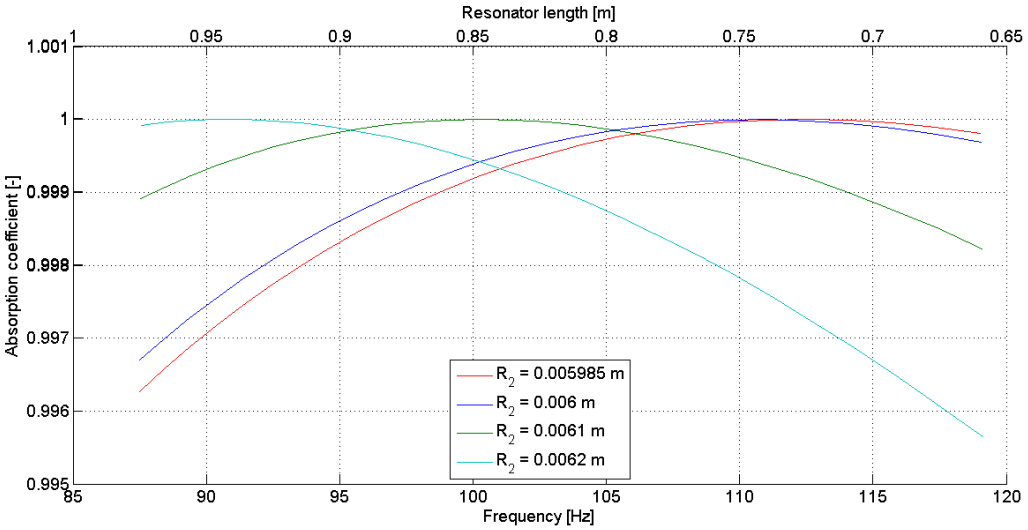

Figure 0.5 Relation between tube radius, length, absorption coefficient and working frequency.

Figure 0.5shows that in order to obtain the working frequency at 100 Hz (maxima point at 100 Hz), it is favorable to have a tube radius larger than 6 mm. For working frequency of 100 Hz, a tube inner diameter of 6,1 mm should be used. However, the ordered tube arrived with inner diameter of 5.985 mm. According to Figure 0.5, this tube is suitable for a working frequency of 113 Hz. Nevertheless, this tube can also be used for 100 Hz with absorption coefficient of 99.9% if one uses a length of 85 cm. Since there is a limitation on the length of the tube, the 113 Hz was chosen for resonator length of 0.737 m.

Experiment with foams

To improve the absorption coefficient at 113 Hz, two kinds of porous material are attached to the junction of the traveling wave termination. This was done based on the presumption that higher reflection coefficient than the model might result because the flow is not purely a one-dimensional flow. Therefore, it is desired to have a flow only in one direction to see whether this behavior keeps appearing. This reason is motivated by the fact that the resonator model is a one-dimensional model. The velocity in radial direction is assumed to be zero, therefore this model predicts only one-dimensional flow. Hence, the porous materials are expected to act as a flow straightener and the experimental results are expected to match better with the model.

The porous materials are attached to the junction of the main tube and the traveling wave termination, where it covers the entire surface of the end wall of the main tube and the entrance hole to the traveling wave termination. The frequency sweep is performed at 100 Pa and 600 Pa. The comparison of the experimental results is presented in Figure 0.6.

Consider Figure 0.6(c). The effect of adding a porous material is clearly shown in the steepness of the curve compared to the experiment without the porous material. The foam sample and the glass wool sample show curve with less steep gradient and less wide peak. The reflection coefficient at 113 Hz is also higher for both cases. It can be seen that the foam sample leads to steeper gradient and less wide peak than the glass wool sample.

(a) Foam sample

(b) Glass wool sample

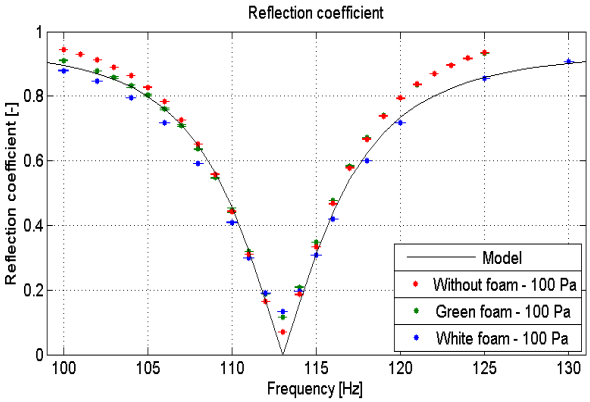

(c) Frequency sweep at 100 Pa

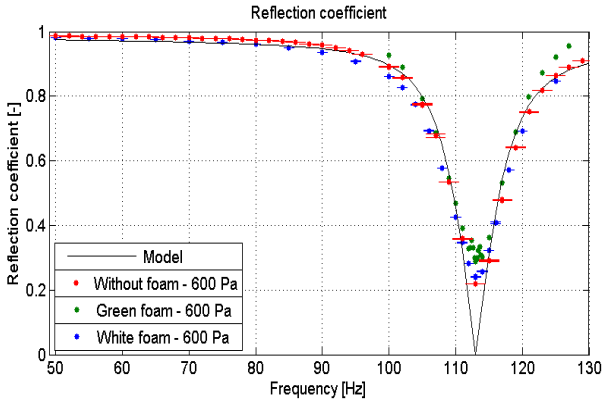

(d) Frequency sweep at 600 Pa

Figure 0.6 The comparison of foam effect at 100 Pa and 600 Pa.

It was expected that the porous materials should give results that match better with the model, however this does not happen. As can be seen around 113 Hz, both samples result in a higher reflection coefficient compared to the experiments without porous material. This might be caused by the location where the samples are attached, which covers the entire surface of the end wall of the main tube. Due to the random structure of the sample matrix, the end wall of the main tube generates an absorbed backward travelling wave (Figure 0.7). The phase of the absorbed backward traveling wave cannot be predicted because of the sample structure, hence it is possible that this backward wave is not in accordance with the initial design. On the other hand, the end wall of the traveling wave termination still has a reflecting surface that produces the same reflection wave. Thus, the two reflection waves from both traveling wave termination and the main tube will not be able to cancel each other as good as the case when the porous material is not used.

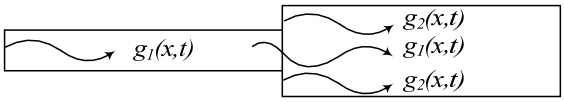

(a) Without porous material

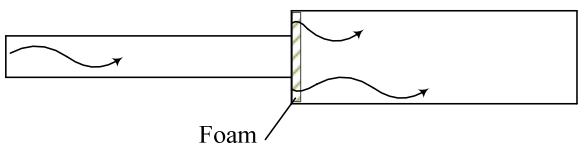

(b) With porous material

Figure 0.7 Schematic of the backward traveling wave.
(b) The case of porous material covers the end wall: the end wall reflection wave has a random phase, consequently it cannot cancel the reflection from the traveling wave termination.

From this set of experiment, it can be concluded that the porous material does not improve the performance of the traveling wave termination. This means that either the foam does not act as a flow straightener, or it acts as a flow straightener but there is other parameter that affects the performance of the traveling wave termination. One way to check whether the porous material can act as a flow straightener is by attaching the foam only at the hole to the entrance of the traveling wave termination, and see whether the result match better with the model.

Other possible reason is that a nonlinear effect takes place. The nonlinear effects occur at high amplitude so that the linear theory cannot hold anymore [3]. Since the model that has been developed is a linear model and it neglects the higher order terms, this effect is not incorporated in the model. One example of the neglected term in the model is the higher harmonics. This phenomenon was observed by Gaitan and Atchley [27]. The generation of higher harmonics can cause nonlinear waveforms and its effect is highest near the resonance [1]. Higher harmonics can also interact together to form shock waves. Their measurement indicates that 20% of the acoustic power is dissipated due to the higher harmonics. Other nonlinear effect can exist in the form of flow disruption. A turbulence flow can arise due to abrupt changes in the cross-section of the channel, which leads to flow separation and vortex shedding [1]. Thus, it is concluded that the discrepancy of the experimental result and the model is probably caused by higher harmonics and turbulence at the junction of the traveling wave termination.

APPENDIX B

EXPERIMENTAL RESULTS

OF PRESSURE AND POWER MEASUREMENT

Comparison of pressure drop and power dissipation for all jet pump samples in a traveling wave.

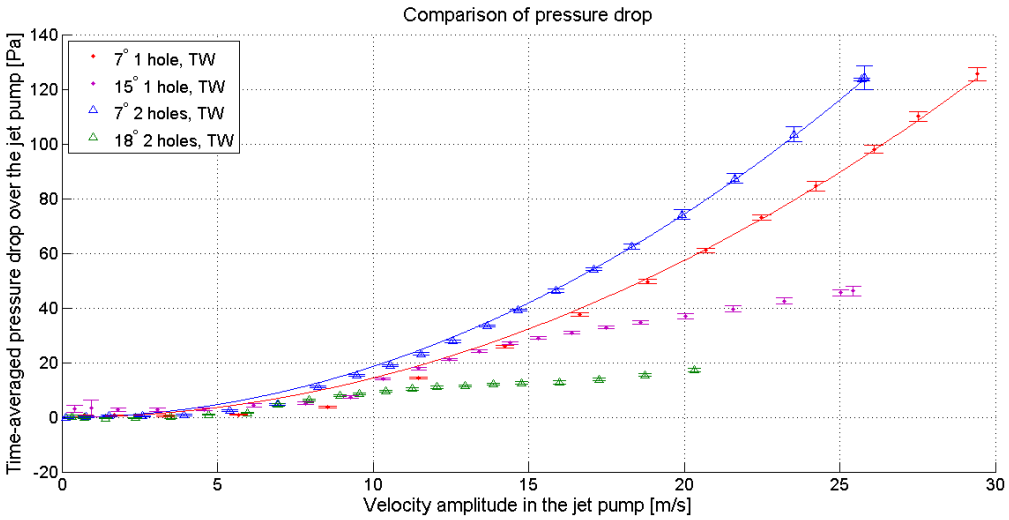

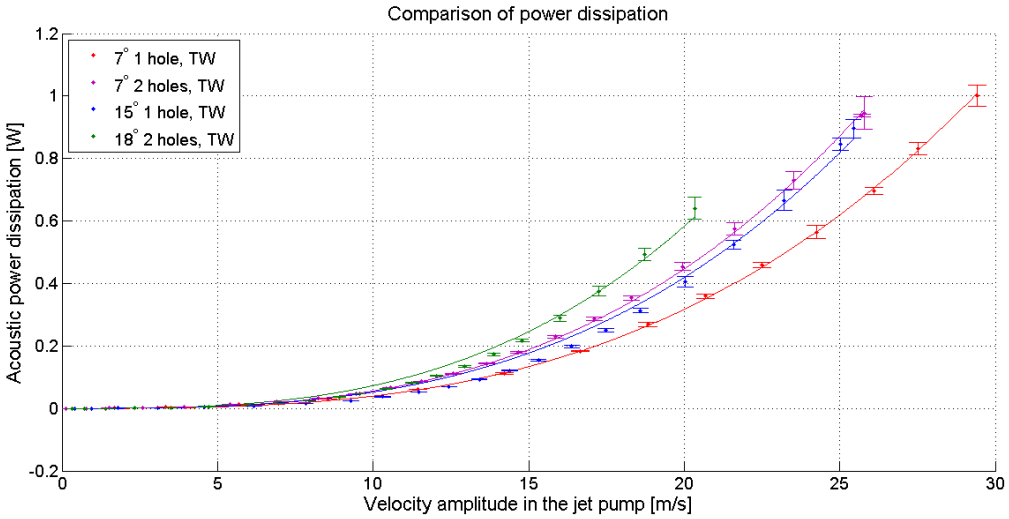

PRESSURE DROP

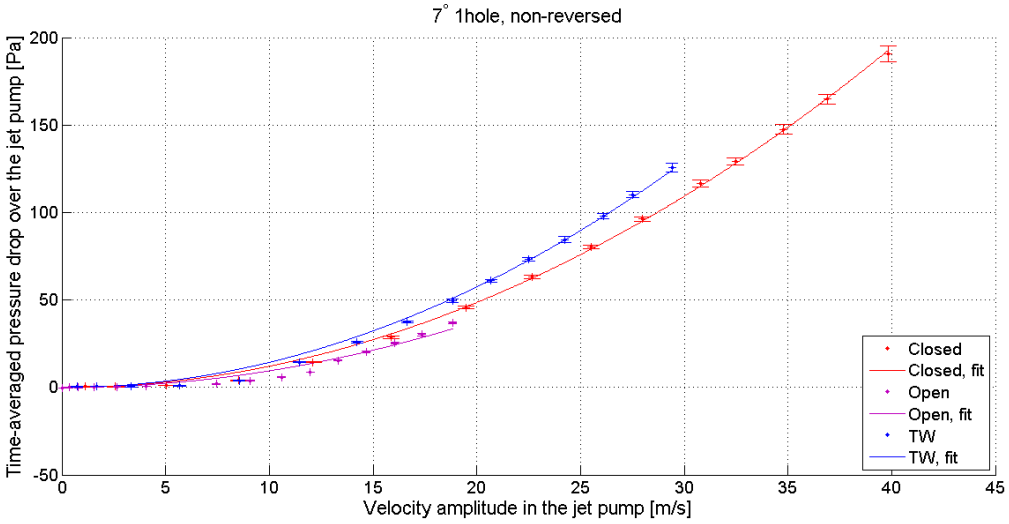

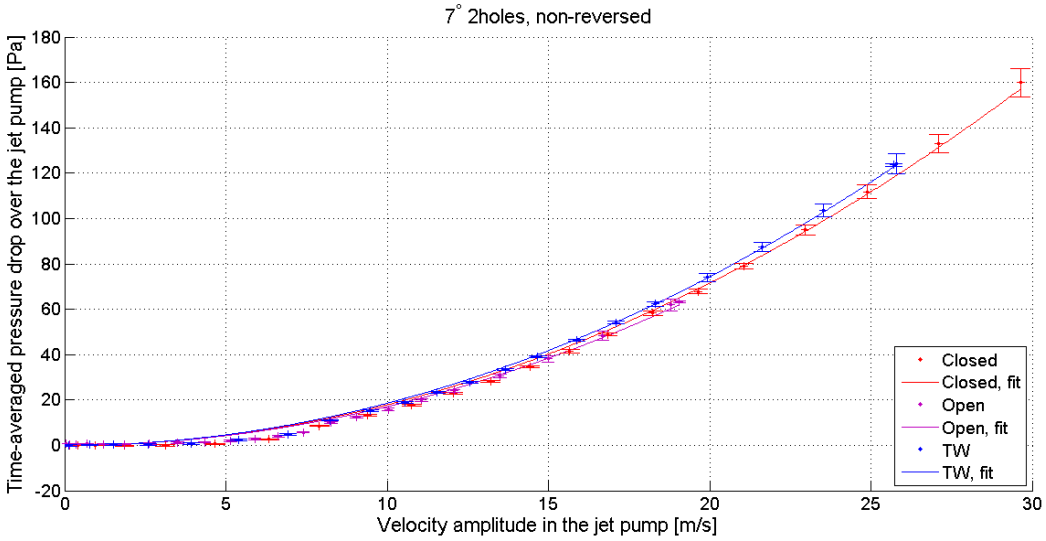

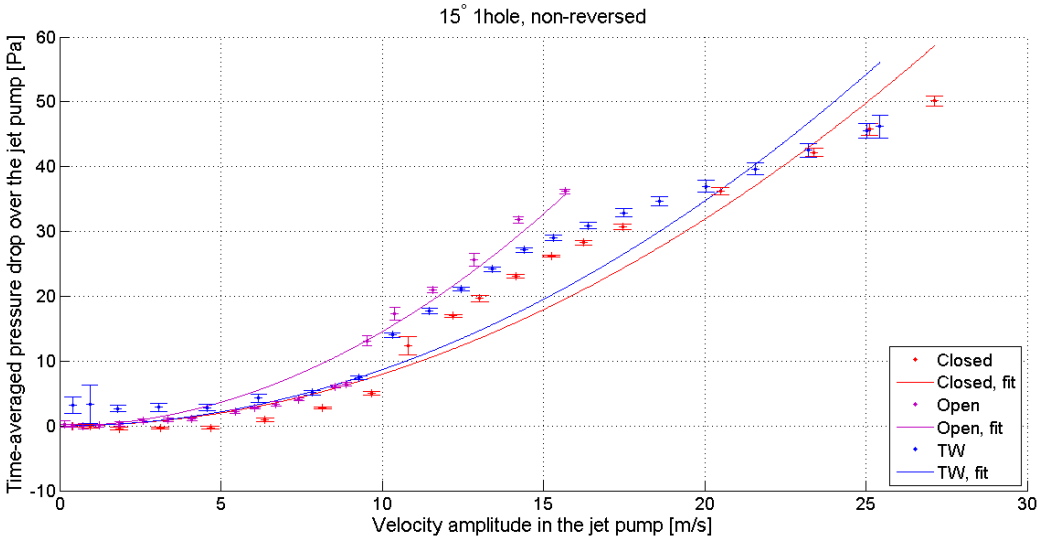

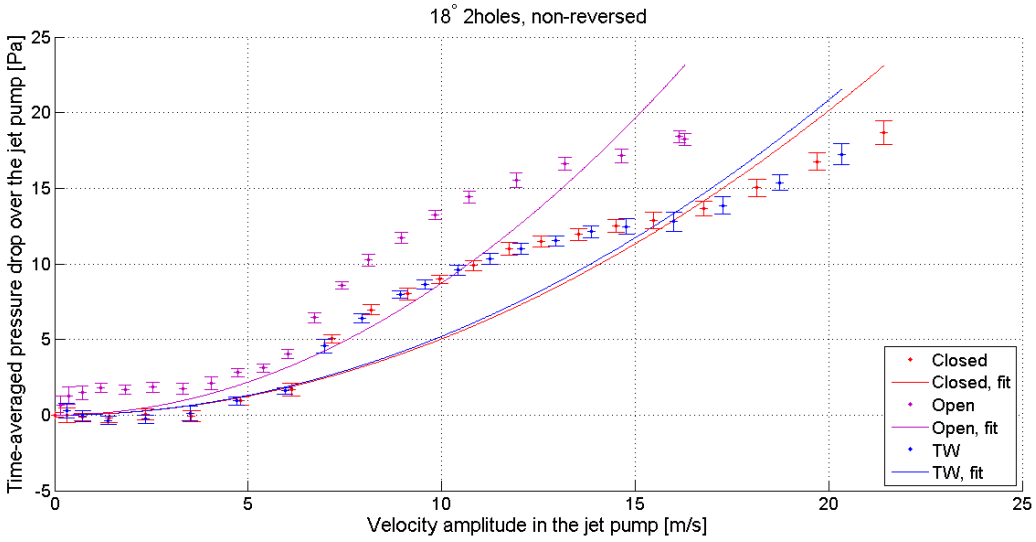
18° 2holes, non-reversed
Time-averaged pressure drop over the jet pump [Pa]
Velocity amplitude in the jet pump [m/s]
Closed
Closed, fit
Open
Open, fit
TW
TW, fit

POWER

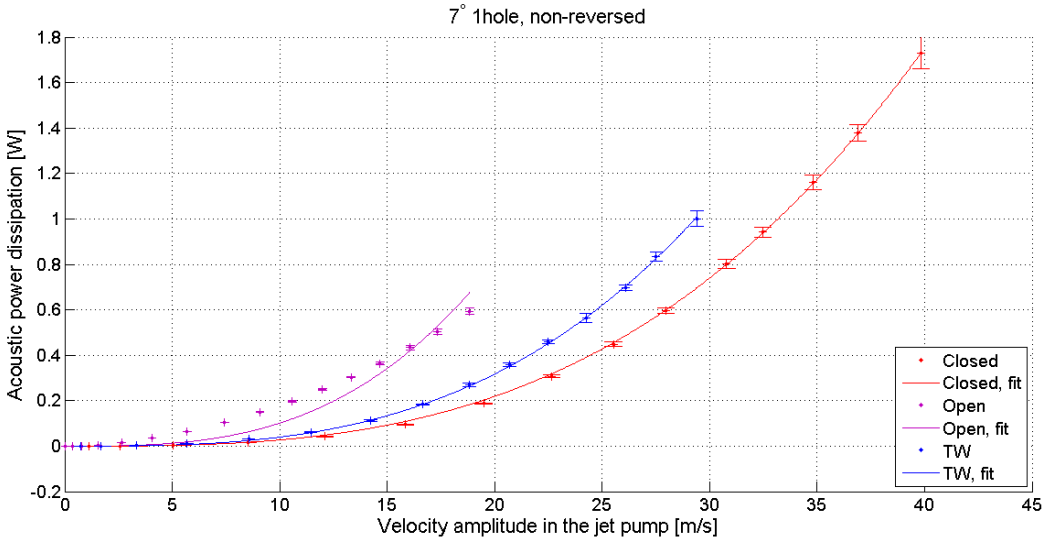
7° 1hole, non-reversed
Acoustic power dissipation [W]
Velocity amplitude in the jet pump [m/s]
Closed
Closed, fit
Open
Open, fit
TW
TW, fit

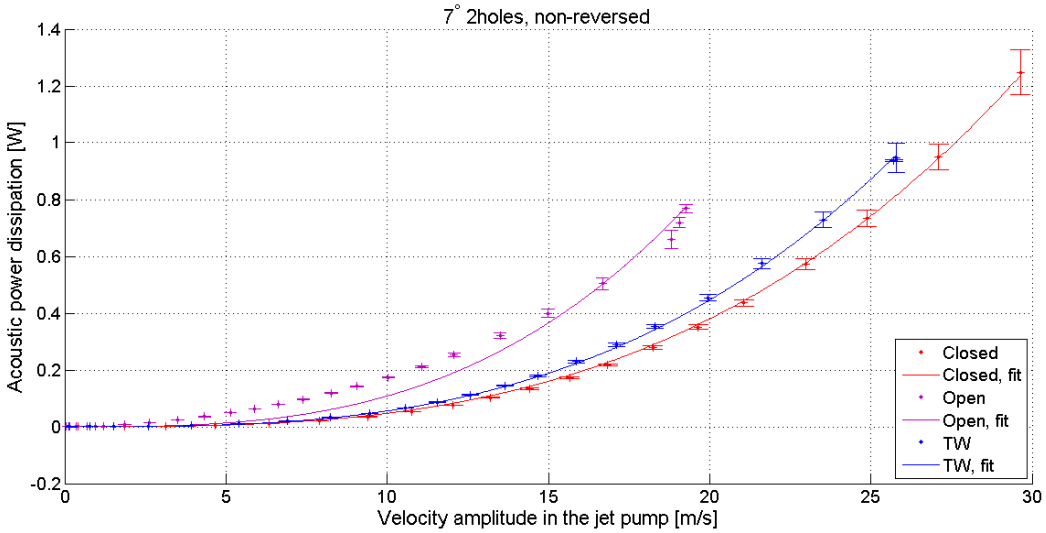
7° 2holes, non-reversed
Acoustic power dissipation [W]
Velocity amplitude in the jet pump [m/s]
Closed
Closed, fit
Open
Open, fit
TW
TW, fit

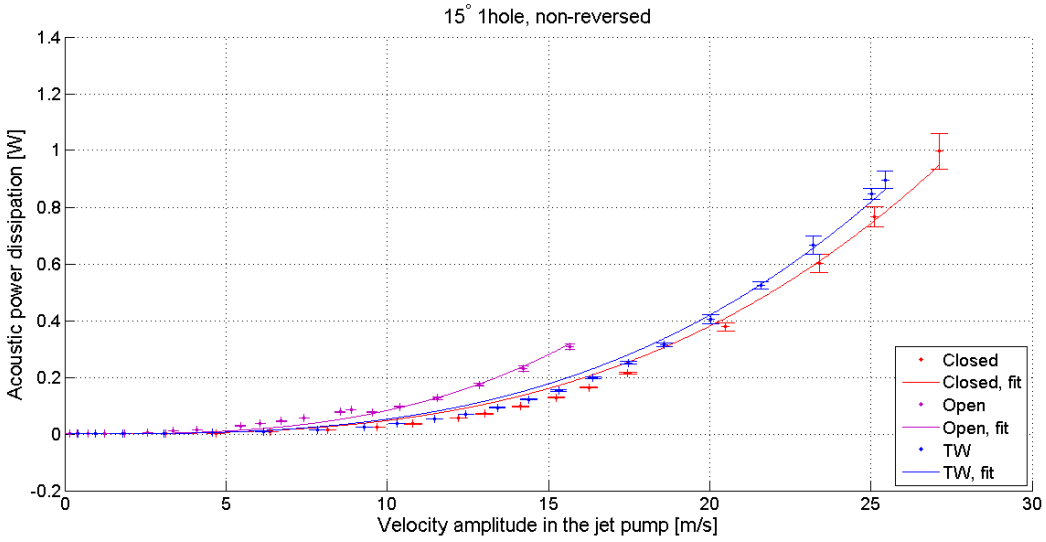

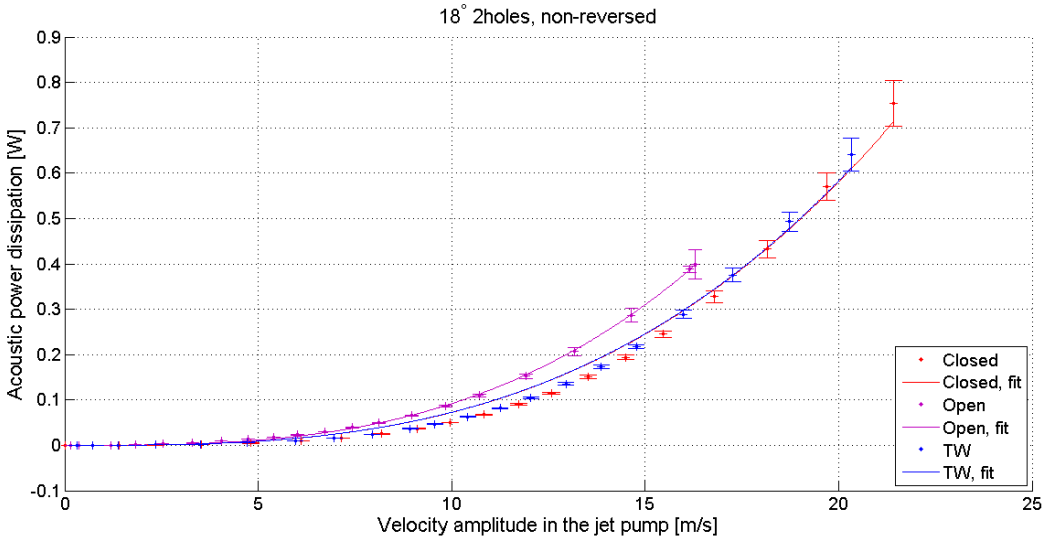

COP

A parameter is introduced to describe the efficiency of a jet pump. Here the term "coefficient of performance (COP)" is used. The COP is defined as the ratio of power dissipation over pressure drop. It indicates the amount of power that is dissipated for a certain pressure drop. The lower the value of this ratio will be favorable.

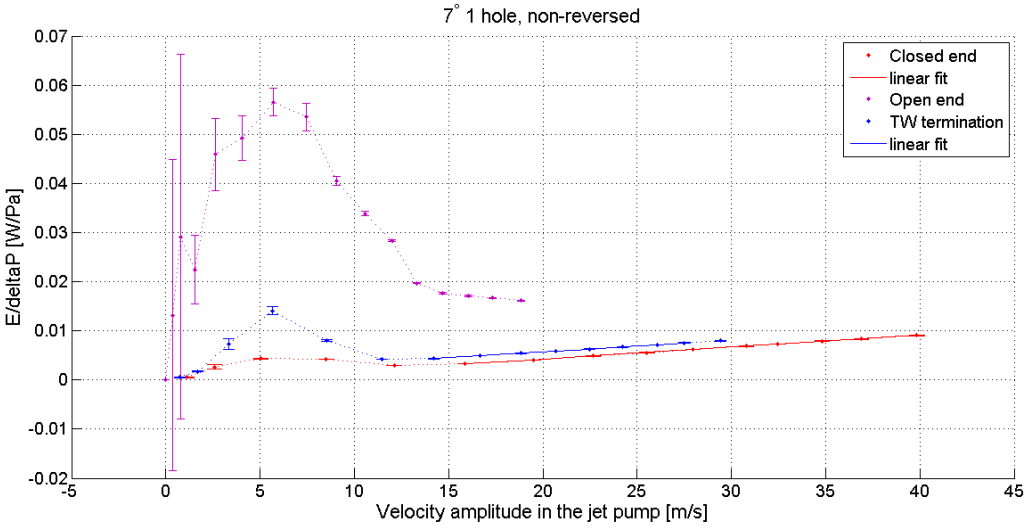

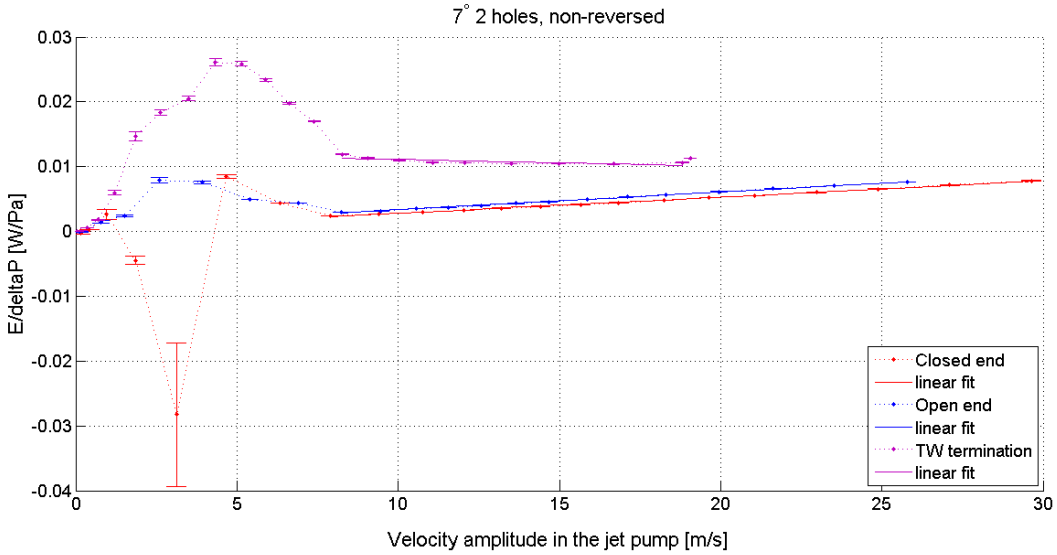
7° 2 holes, non-reversed
E/deltaP [W/Pa]
Velocity amplitude in the jet pump [m/s]
Closed end
linear fit
Open end
linear fit
TW termination
linear fit

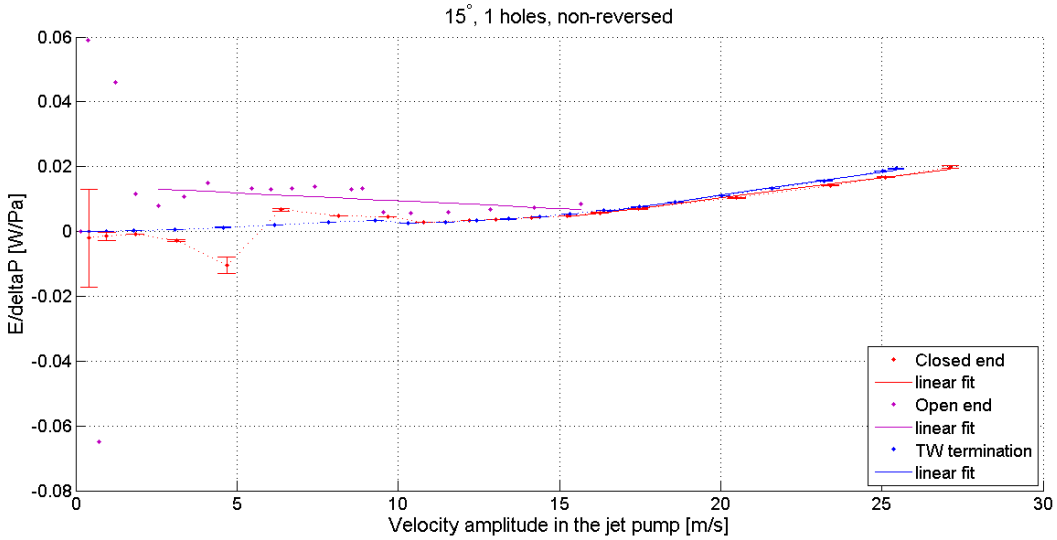
15°, 1 holes, non-reversed
E/deltaP [W/Pa]
Velocity amplitude in the jet pump [m/s]
Closed end
linear fit
Open end
linear fit
TW termination
linear fit

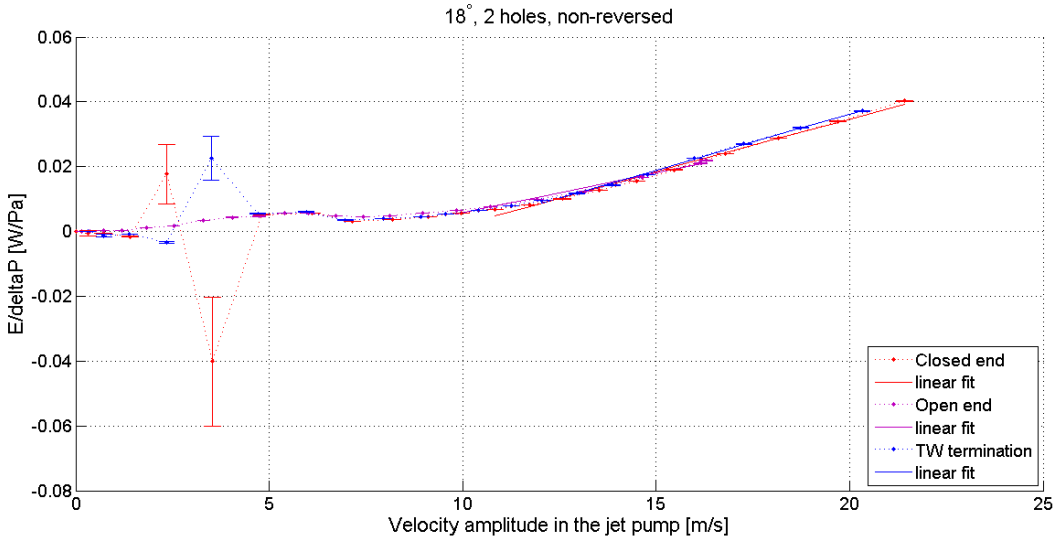
18°, 2 holes, non-reversed
E/deltaP [W/Pa]
Velocity amplitude in the jet pump [m/s]
Closed end
linear fit
Open end
linear fit
TW termination
linear fit

REVERSED JET PUMP

PRESSURE DROP

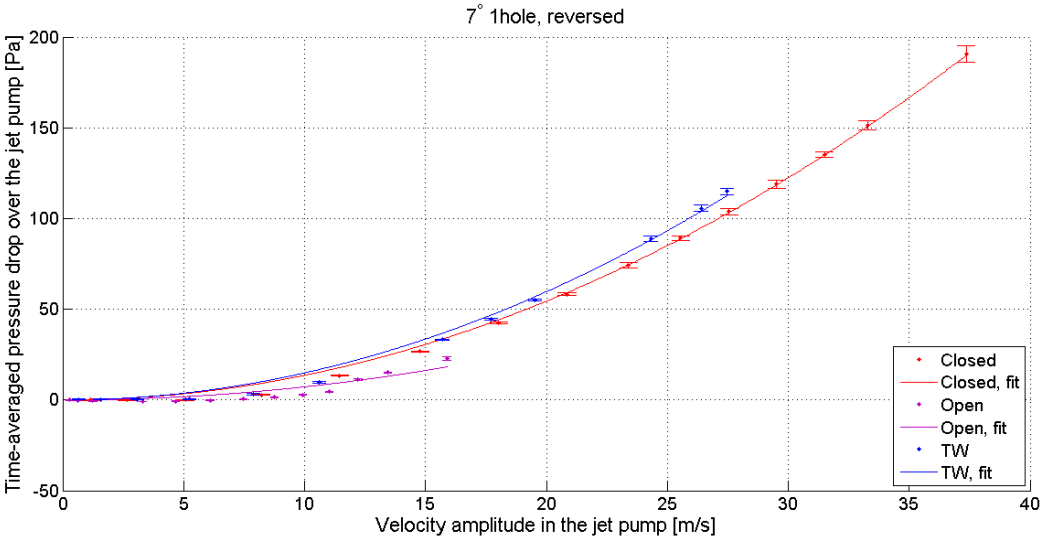

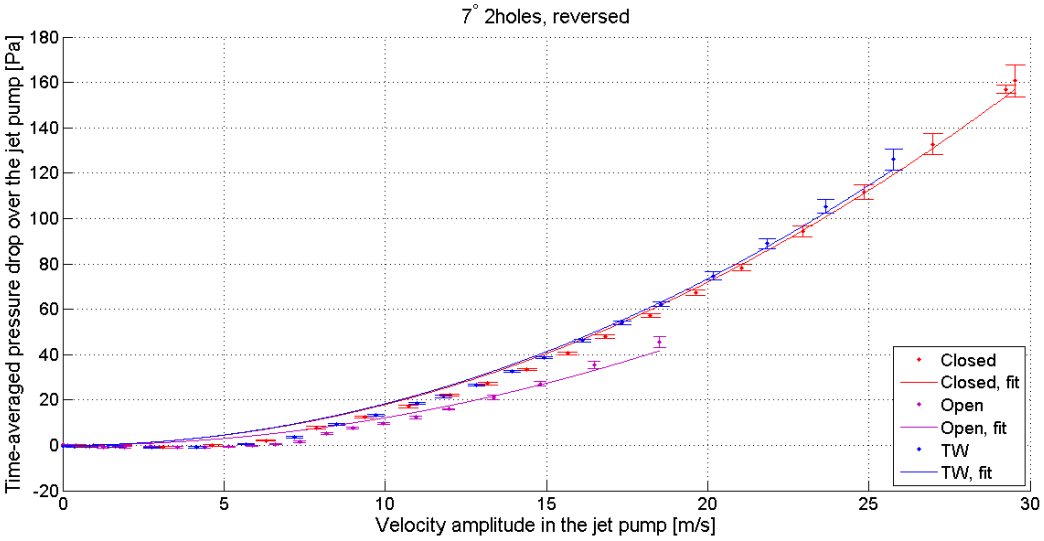

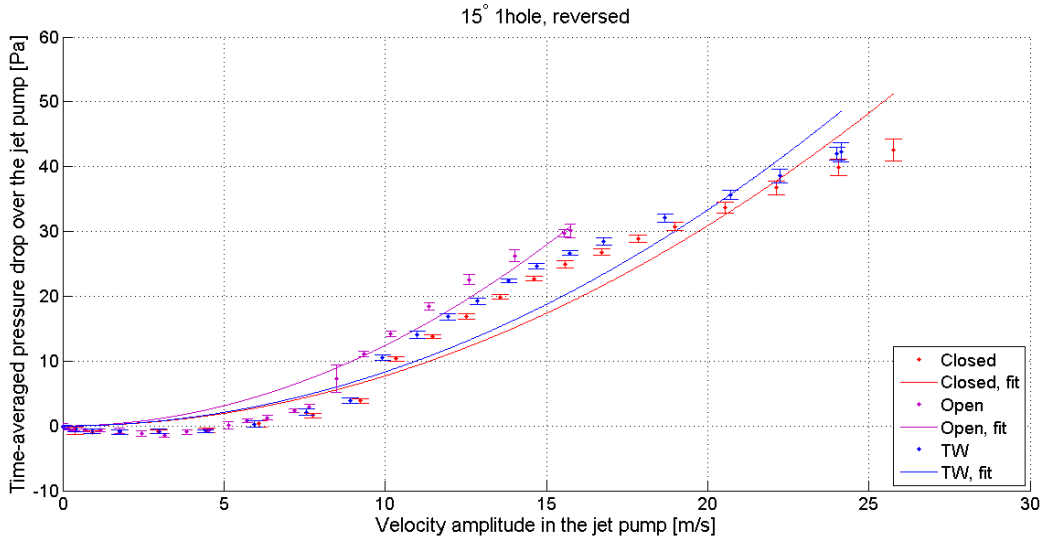

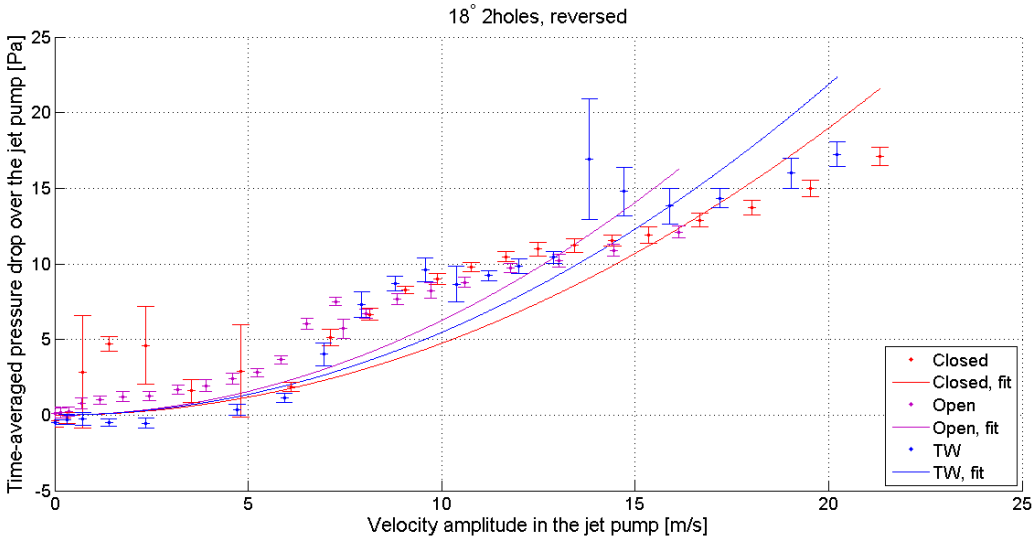
18° 2holes, reversed
Time-averaged pressure drop over the jet pump [Pa]
Velocity amplitude in the jet pump [m/s]
Closed
Closed, fit
Open
Open, fit
TW
TW, fit

POWER

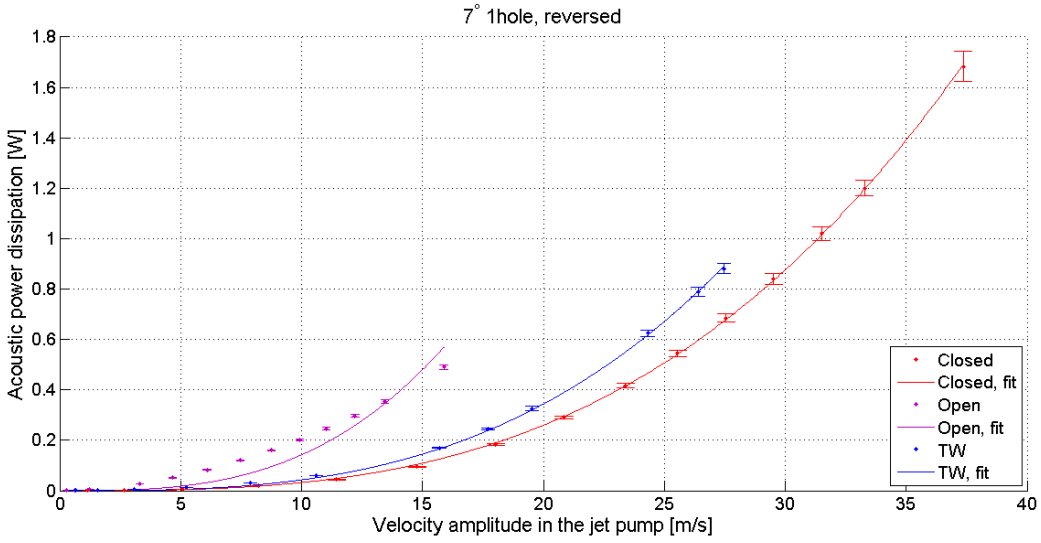
7° 1hole, reversed
Acoustic power dissipation [W]
Velocity amplitude in the jet pump [m/s]
Closed
Closed, fit
Open
Open, fit
TW
TW, fit

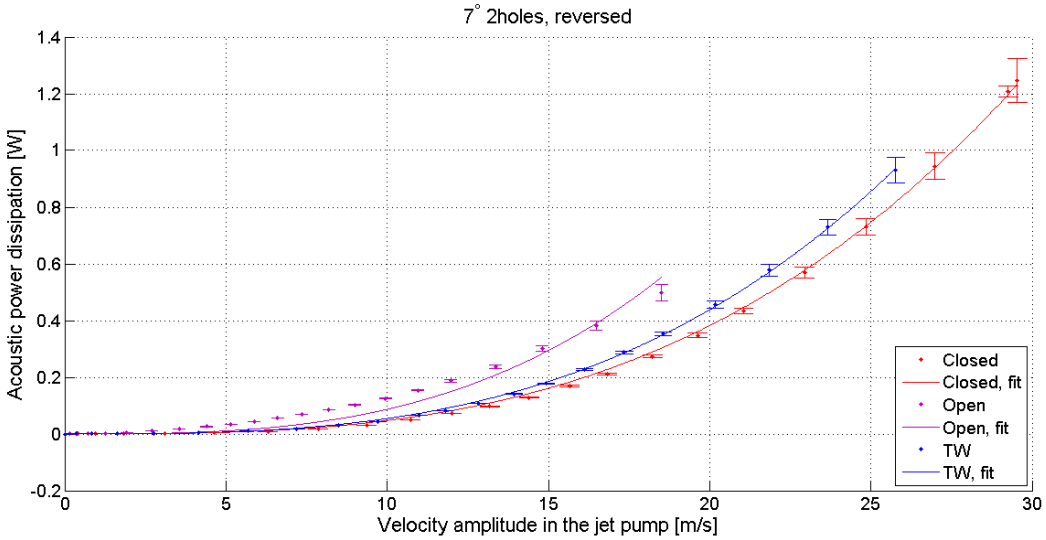
7° 2holes, reversed
Acoustic power dissipation [W]
Velocity amplitude in the jet pump [m/s]
Closed
Closed, fit
Open
Open, fit
TW
TW, fit

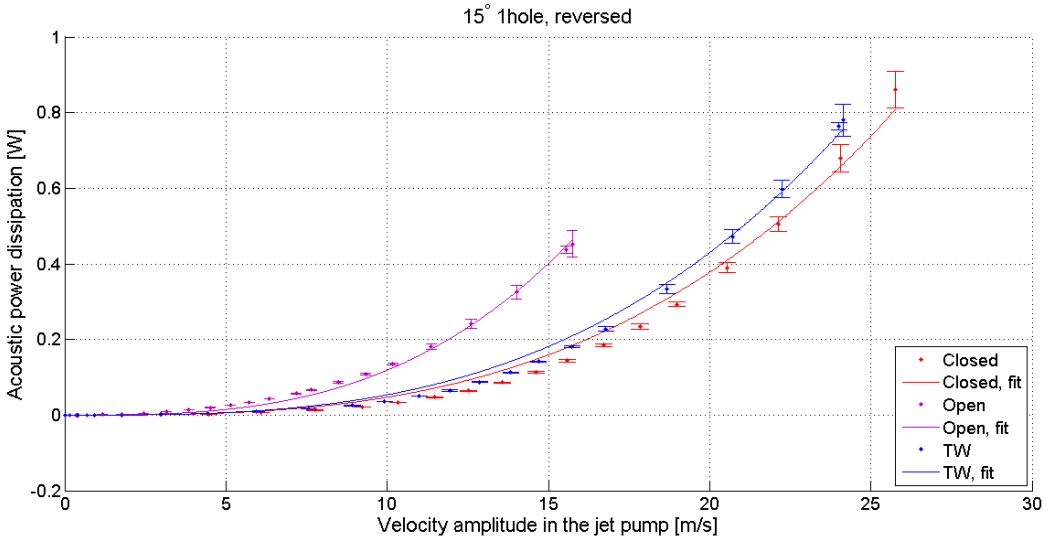
15° 1hole, reversed
Acoustic power dissipation [W]
Velocity amplitude in the jet pump [m/s]
Closed
Closed, fit
Open
Open, fit
TW
TW, fit

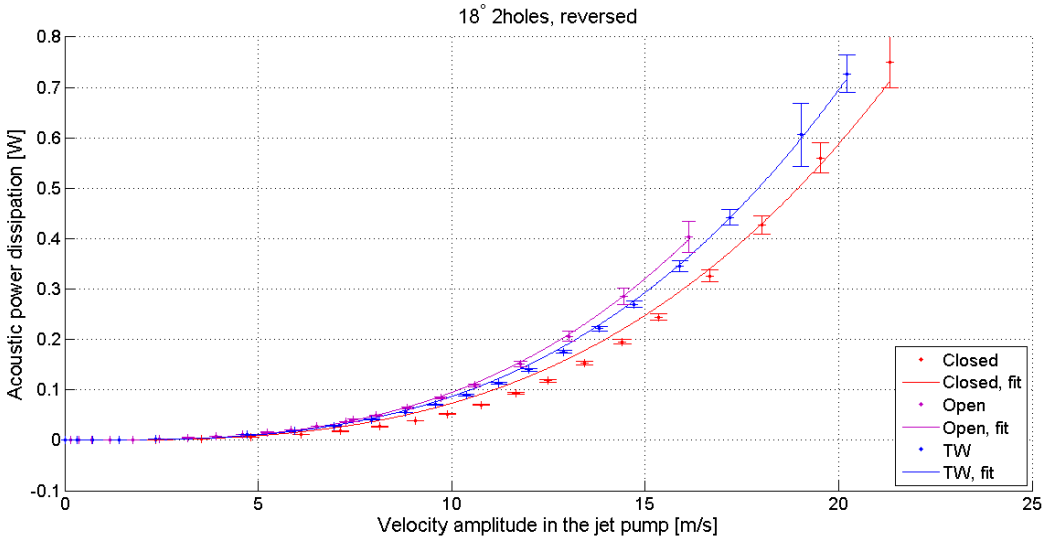
18° 2holes, reversed
Acoustic power dissipation [W]
Velocity amplitude in the jet pump [m/s]
Closed
Closed, fit
Open
Open, fit
TW
TW, fit

COP

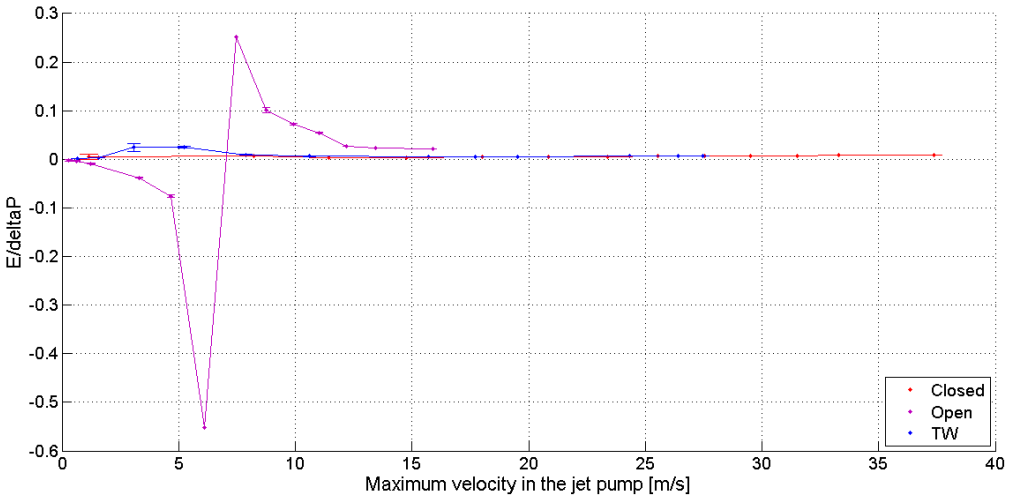
E/deltaP
Maximum velocity in the jet pump [m/s]
Closed
Open
TW

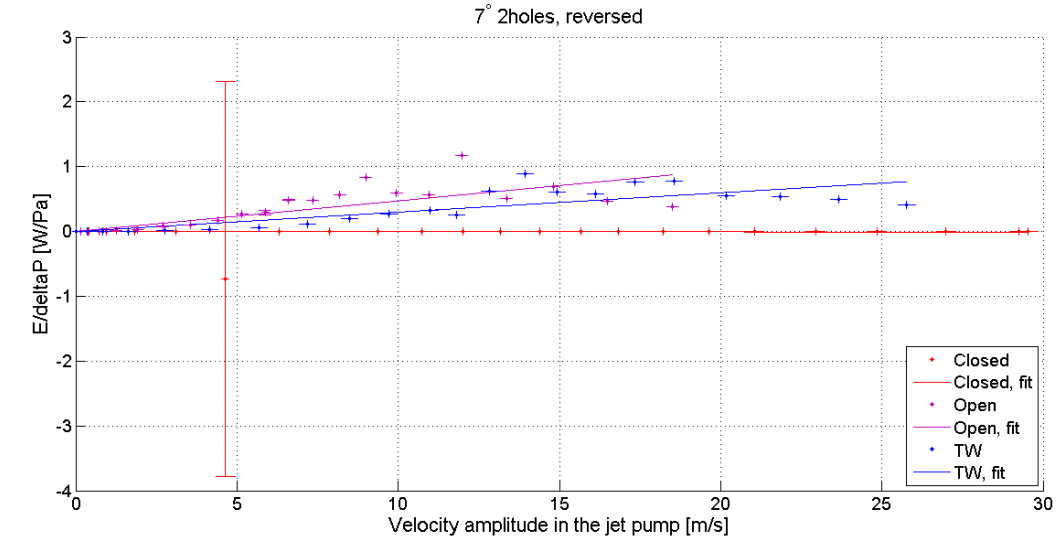
7° 2holes, reversed
E/deltaP [W/Pa]
Velocity amplitude in the jet pump [m/s]
Closed
Closed, fit
Open
Open, fit
TW
TW, fit

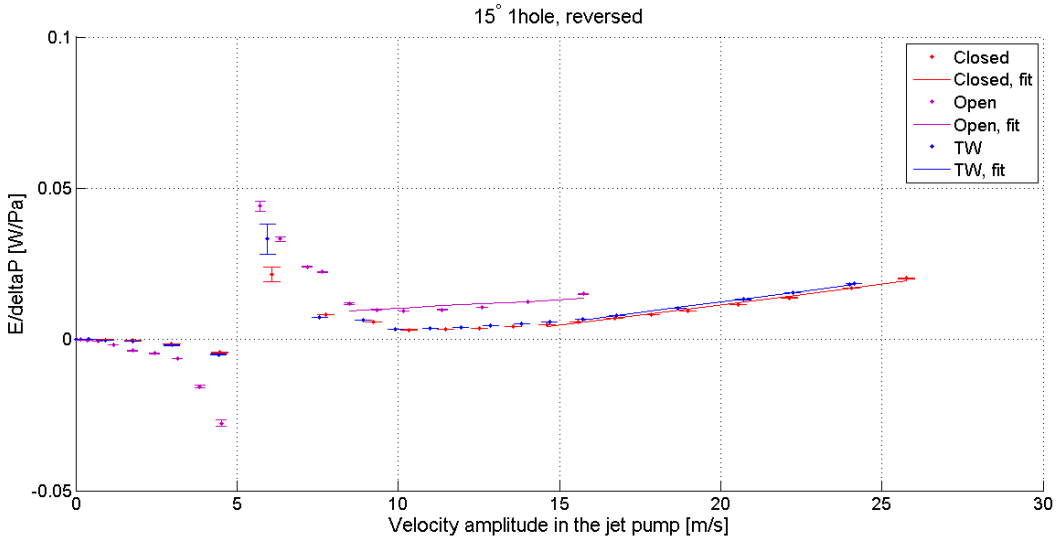
15° 1hole, reversed
E/deltaP [W/Pa]
Velocity amplitude in the jet pump [m/s]
Closed
Closed, fit
Open
Open, fit
TW
TW, fit

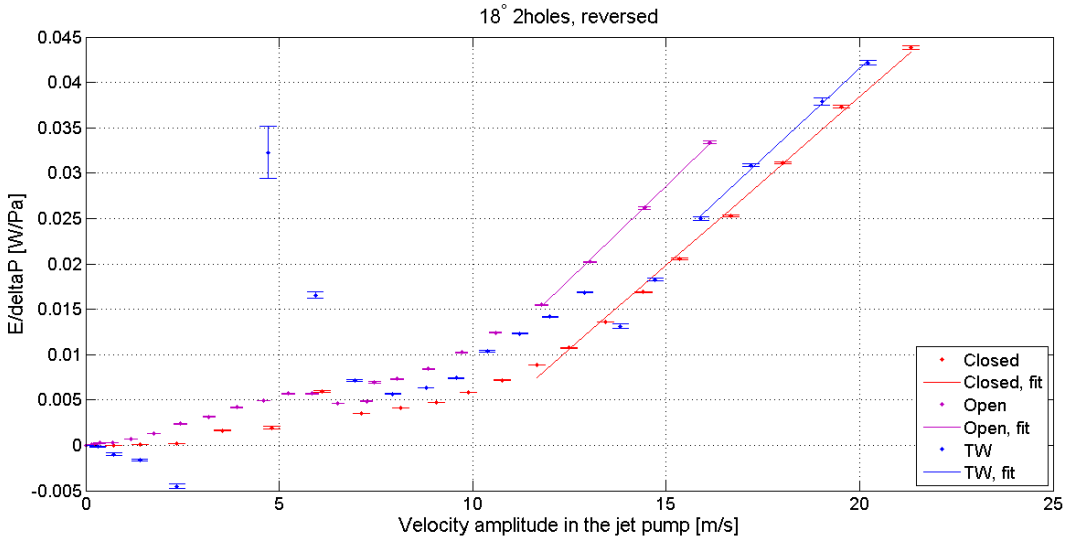
18° 2holes, reversed
E/deltaP [W/Pa]
Velocity amplitude in the jet pump [m/s]
Closed
Closed, fit
Open
Open, fit
TW
TW, fit

APPENDIX C

CALCULATION OF INNER WALL SURFACE AREA

The calculation of the inner wall surface area was performed for all jet pump samples. The dimensions are known from measurement and are listed in Table 3.1. The inner wall surface area is defined as the area of the tapered surface and the curved surface that connects the taper and $R_{s,min}$. Since the radius of curvature R_{curv} cannot be measured, it was assumed to be 5 mm and that the curvature forms an exact circle. The area that contributes to the calculation of the inner wall surface area is depicted in Figure 0.1 with red line.

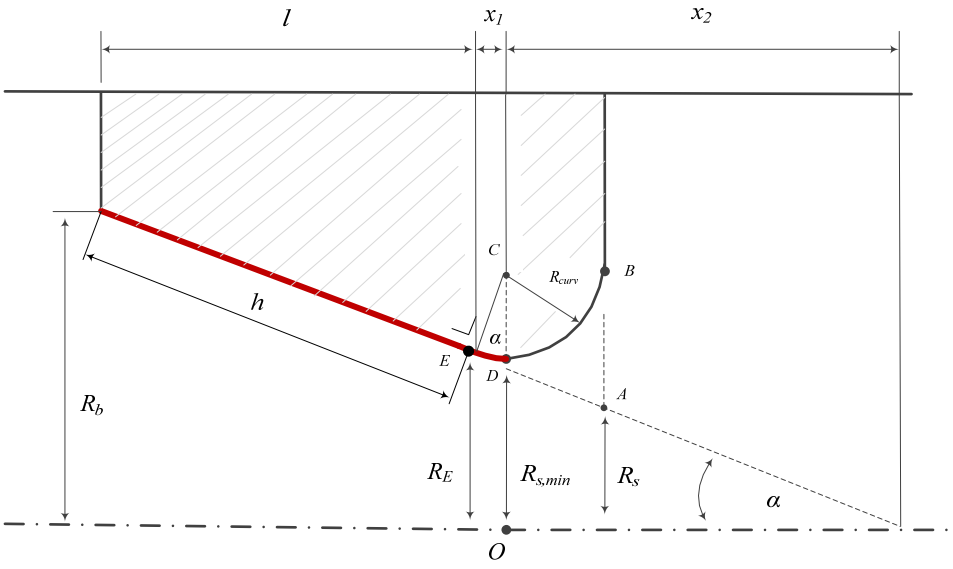

Figure 0.1 Inner wall surface area

The tapered surface area A_h is defined in the following equation.

$$A_h = \pi R_b(l + x_1 + x_2) - \pi R_E(x_1 + x_2) \tag{B.1}$$

Substituting l, R_E, x_1 and x_2 with Equation (B.2), A_h can be written as a function of $R_{s,min}$, R_{curv} and L_{JP}.

$$l = L_{JP} - R_{curv} - x_1$$

$$x_1 = R_{curv} \sin\alpha \tag{B.2}$$

$$x_2 = \frac{R_{s,min}}{\tan\alpha}$$

$$R_E = R_{s,min} + R_{curv} \sin\alpha \tan\alpha$$

The curved surface area A_c can be calculated based on the parametric formulation for a circle equation with its center is located in (h,k) in Cartesian coordinate and a radius R_{curv}. This parametric equation can be expressed by Equation (B.3).

$$x = h + R_{curv} \sin \alpha \tag{B.3}$$

$$y = k + R_{curv} \cos \alpha$$

Assuming the origin (0,0) is located in point O (see Figure 0.1), Equation (B.3) can be expressed as follows:

$$\begin{aligned} x &= R_{curv} \sin \alpha \\ y &= R_{curv} + R_{s,min} + R_{curv} \cos \alpha \end{aligned} \tag{B.4}$$

The curvature in Figure 0.1 is symmetric to the x axis. The surface area of the curvature if it is rotated with respect to the x axis is formulated in Equation (B.5).

$$S = \int 2\pi y \, ds \tag{B.5}$$

With ds is defined in the following equation.

$$ds = \sqrt{\left(\frac{dx}{d\alpha}\right)^2 + \left(\frac{dy}{d\alpha}\right)^2} \, dt \tag{B.6}$$

Deriving Equation (B.4) with respect to α, the following equation is obtained.

$$ds = R_{curv} \, d\alpha \tag{B.7}$$

Therefore, Equation (B.5) can be written as follows:

$$S = \int_0^7 2\pi R_{curv} \left(R_{curv} + R_{s,min} + R_{curv} \cos \alpha\right) d\alpha \tag{B.8}$$

Solving Equation (B.8), the curved surface area A_c is obtained.

APPENDIX D

SEQUENCE OF IMAGES

FROM FLOW VISUALIZATION

Vortex ring propagation

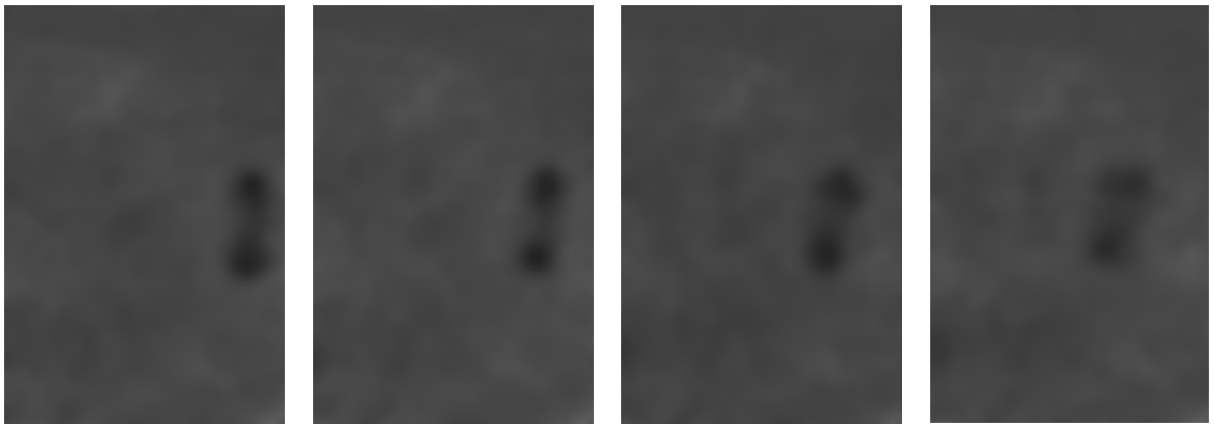

t = 0.209 s | t = 0.210 s | t = 0.211 s | t = 0.212 s

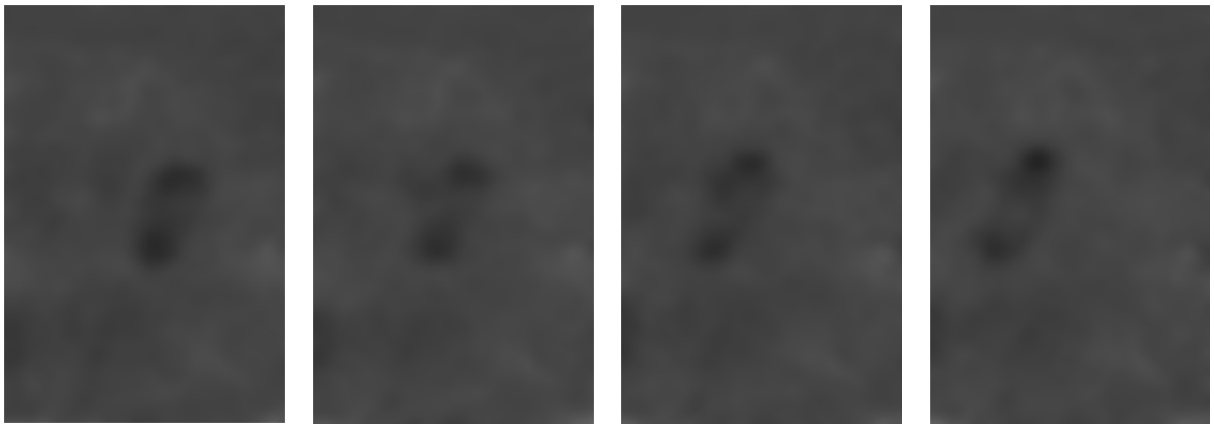

t = 0.213 s | t = 0.214 s | t = 0.215 s | t = 0.216 s

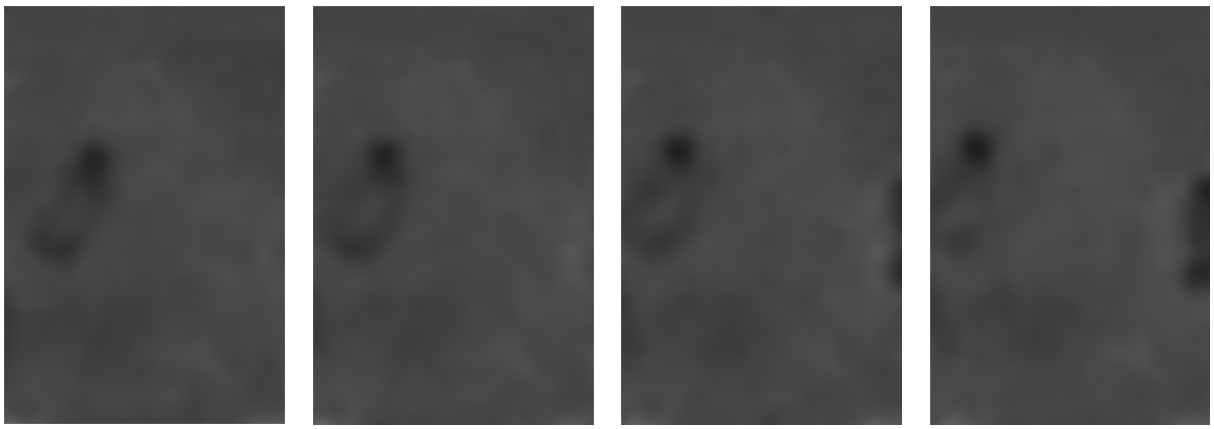

t = 0.217 s | t = 0.218 s | t = 0.219 s | t = 0.220 s